Strojniški vestnik
Journal of Mechanical Engineering

Since 1955

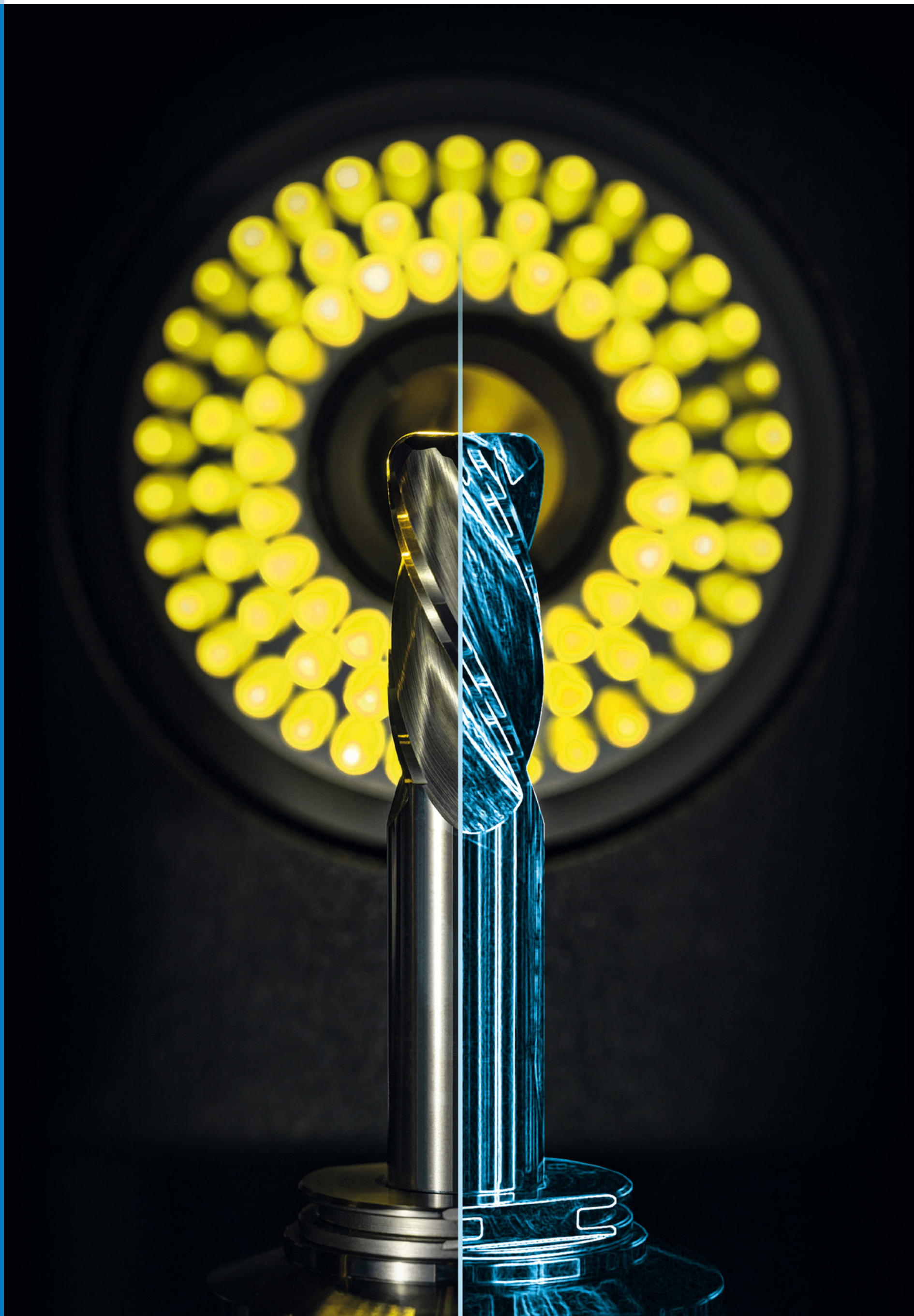

no. 2
year 2019
volume 65

Strojniški vestnik – Journal of Mechanical Engineering (SV-JME)

Aim and Scope

The international journal publishes original and (mini)review articles covering the concepts of materials science, mechanics, kinematics, thermodynamics, energy and environment, mechatronics and robotics, fluid mechanics, tribology, cybernetics, industrial engineering and structural analysis.
The journal follows new trends and progress proven practice in the mechanical engineering and also in the closely related sciences as are electrical, civil and process engineering, medicine, microbiology, ecology, agriculture, transport systems, aviation, and others, thus creating a unique forum for interdisciplinary or multidisciplinary dialogue.
The international conferences selected papers are welcome for publishing as a special issue of SV-JME with invited co-editor(s).

Editor in Chief
Vincenc Butala
University of Ljubljana, Faculty of Mechanical Engineering, Slovenia

Technical Editor
Pika Škraba
University of Ljubljana, Faculty of Mechanical Engineering, Slovenia

Founding Editor
Bojan Kraut
University of Ljubljana, Faculty of Mechanical Engineering, Slovenia

Editorial Office
University of Ljubljana, Faculty of Mechanical Engineering
SV-JME, Aškerčeva 6, SI-1000 Ljubljana, Slovenia
Phone: 386 (0)1 4771 137
Fax: 386 (0)1 2518 567
info@sv-jme.eu, http://www.sv-jme.eu

Print: Papirografika, printed in 300 copies

Founders and Publishers
University of Ljubljana, Faculty of Mechanical Engineering, Slovenia
University of Maribor, Faculty of Mechanical Engineering, Slovenia
Association of Mechanical Engineers of Slovenia
Chamber of Commerce and Industry of Slovenia, Metal Processing Industry Association

President of Publishing Council
Mitjan Kalin
University of Ljubljana, Faculty of Mechanical Engineering, Slovenia

Vice-President of Publishing Council
Bojan Dolšak
University of Maribor, Faculty of Mechanical Engineering, Slovenia

Cover:
Universal presetting & measuring device Zoller Smile 420 for no-contact measuring and presetting of cutting tools is installed in Laboratory for machining processes (LABOD), Faculty of Mechanical Engineering, University of Maribor. Along with quick and precise measurements, direct and secure transmission of tool data to the machine tools and monitoring systems it is ideal for integrating in smart cyber-physical machining systems.

Image courtesy:
ZOLLER Austria GmbH

ISSN 0039-2480, ISSN 2536-2948 (online)

General information

Strojniški vestnik – Journal of Mechanical Engineering is published in 11 issues per year (July and August is a double issue).

Institutional prices include print & online access: institutional subscription price and foreign subscription €100,00 (the price of a single issue is €10,00); general public subscription and student subscription €50,00 (the price of a single issue is €5,00). Prices are exclusive of tax. Delivery is included in the price. The recipient is responsible for paying any import duties or taxes. Legal title passes to the customer on dispatch by our distributor. Single issues from current and recent volumes are available at the current single-issue price. To order the journal, please complete the form on our website. For submissions, subscriptions and all other information please visit: *http://www.sv-jme.eu.*

You can advertise on the inner and outer side of the back cover of the journal. The authors of the published papers are invited to send photos or pictures with short explanation for cover content.

We would like to thank the reviewers who have taken part in the peer-review process.

The journal is subsidized by Slovenian Research Agency.

Strojniški vestnik - Journal of Mechanical Engineering is available on *https://www.sv-jme.eu*.

Contents

Strojniški vestnik - Journal of Mechanical Engineering
volume 65, (2019), number 2
Ljubljana, February 2019
ISSN 0039-2480

Published monthly

Papers

Strojniški vestnik - Journal of Mechanical Engineering 65(2019)2, 67-77

DOI:10.5545/sv-jme.2018.5792
Original Scientific Paper
Received for review: 2018-10-13
Received revised form: 2018-12-06
Accepted for publication: 2019-01-14

A Cyber-Physical System for Surface Roughness Monitoring in End-Milling

Uroš Županl* – Franci Čuš
University of Maribor, Faculty of Mechanical Engineering, Slovenia

The main focus of this paper is to describe the structure of the cyber-physical machining system developed for on-line surface roughness monitoring via cutting chip size control in end-milling. The two level cyber- physical machining system is realized by connecting the computing resources in the developed cloud machining platform to the machine tool with its smart sensor system. The smart optical sensor system is developed to acquire and transfer in real time the values of the cutting chips sizes to the cloud level. The cloud based machining platform with the developed internet of things applications is employed to perform instant surface roughness monitoring and cutting chip size control based on advanced sensor signal processing, edge computing, process feature extraction, machine learning, process modeling, data analyzing and cognitive corrective process control acting. These actions are performed as cloud services. A cloud application with an adaptive neural inference system is applied to model and on-line predict surface roughness based on the determined cutting chip size. Based on the in-process predictions, a novel application for cognitive corrective control acting is employed to control the cutting chip size by modifying the machining parameters and consequently keeping surface roughness constant. The results of the machining experiment are presented to demonstrate that this proposed system where the cloud computing resources and services are linked with the machine tool is feasible and could be implemented to monitor surface roughness during milling operation.
Keywords: machining, end milling, chip size control, surface roughness, monitoring

Highlights
- *Cyber-physical machining system is developed to realize end-milling process monitoring.*
- *A new way for controlling the chip size and monitoring the surface roughness is developed.*
- *An adaptive neural inference system is applied to in-process predict the surface roughness.*
- *A visual system is employed to detect the cutting chip size.*
- *Machining experiment for testing the cloud based machining platform is provided.*

0 INTRODUCTION

Modern machining systems dealing with variety of products in small series demand real-time monitoring abilities that are adaptive to the sudden changes of cutting conditions. The modern computer numerical control (CNC) controllers and smart sensors are now efficient and intelligent enough to communicate with devices and process the raw data during machining. Internet of Things (IoT) and cloud manufacturing technologies provide an efficient environment for integrating and connecting knowledge, software, computing and physical parts of distributed machining equipment together. These new cloud technologies can be employed for efficient machining process monitoring and control applications. They can be used to connect machine tool and smart sensors together with cloud based monitoring capabilities via the internet networking infrastructure. Such systems that connect the cyber-world of computing, service resources and communications in the cloud with the physical devices are referred to as cyber-physical systems (CPSs) [1]. The cloud based smart monitoring systems may consequentially increase productivity, reduce machining cost and improve surface quality by efficient system adaptation.

Self-monitoring, analysis, and reporting technology (Smart or S.M.A.R.T) is a monitoring system with the aim to predict or anticipate the potential process problems or failures. It includes sensing, actuation and control functions in order to analyze a process and perform actions based on the available data in an adaptive manner. The smartness of the system is often attributed to autonomous operation based on closed loop control and networking capabilities [1]. Recently, a few smart machining systems have been designed to carry out adaptive control of machine tools. Wang et al. [2] presented a concept and innovative use of adaptive smart machining based on using constant cutting force and a smart cutting tool, developed by authors. Teti et al. [3] reviewed advanced monitoring achievements in machining operations, from sensorial perception and feature extraction to cognitive decision making and action.

Nowadays, surface finish monitoring control becomes increasingly important for the smooth operation of modern machine tools.

*Corr. Author's Address: University of Maribor, Faculty of Mechanical Engineering, Smetanova 17, Maribor, Slovenia, uros.zuperl@um.si

Recently, the research efforts to improve surface finish of machined parts have been oriented towards developing of advanced surface finish control systems which contain reliable in-process models that can efficiently predict surface roughness. A statistical model to correlate surface roughness and cutting force in end-milling operations is employed in a research of Chen and Huang [4]. Abburi and Dixit [5] apply machining parameters and two cutting force components for online prediction of surface finish. Rao et al. [6] use singular spectrum analysis to decompose the vibration signals for in-process prediction of surface roughness in turning. Oborski [7] investigates time series analysis of vibration acceleration signals for real-time prediction of surface roughness. Marinescu and Axinte [8] and Axinte et al. [9] use AE signals and cutting force data to detect surface anomalies in milling of aerospace materials. Some systems of surface roughness control have been developed for turning operations, with only a few for end milling operations. Yang et al. [10] developed a fuzzy-nets-based in-process surface roughness adaptive system in end milling. The developed system has the ability to change cutting parameters to produce a high-quality product in-process using a fuzzy-nets adaptive feed rate control system. Zhang and Chen [11] employed a multiple linear regression algorithm to establish an in-process surface roughness evaluation system and an in-process adaptive parameter control (IAPC) system. Zuperl and Cus [12] employ in their model reference adaptive control system (MRAC) a dynamometer as an in-process sensor to indirectly measure and control the surface roughness in milling. The same technique was also applied to the turning process [13]. To address the challenges caused by indirect measuring and control of surface roughness, a new cyber-physical machining system (CPMS) for controlling the cutting chip size and monitoring the surface roughness through internet applications is presented in this paper. In this approach a visual measuring system acquires and transmits the signals of the cutting chip size through the internet to a cloud-based application for control decision making and acting. The latter is responsible for adjusting the optimal cutting parameters.

The paper is organized as follows: In the second section of the paper a CPMS for surface roughness monitoring is presented. Section 3 describes architecture of cloud based machining platform with detailed descriptions of integrated Internet of Things (IoT) applications. Section 4 presents physical resources, experimental results and discussion. Finally, section 5 concludes the paper.

1 CYBER-PHYSICAL MACHINING SYSTEM FOR ROUGHNESS MONITORING

The goal of this research is to develop a CPMS for surface roughness monitoring and control during milling. The proposed system is intended for machining of difficult to cut materials, where small spiral, arc or short coma chips were produced without high pressure cooling. These chip shapes are typically produced when machining workpiece materials with high hardness and low thermal conductivity, such as titanium alloys, nickel alloys and hardened steels (AISI D2 steel of 62 HRC). The CPMS adapts on-line the machining parameters in order to maintain the cutting chip size constant and therefore, to attain the desired value of the machined surface finish. The CPMS serves as a cloud surface roughness monitoring system and is based on the structure shown in Fig. 1. The proposed system is built in two levels. The lower level is a factory or machine level. This level incorporates physical assets (machine tool, optical vision system) and software resources (data acquisition) located in the machining system. The physical resources are connected to the computing resources (monitoring, analysing, data visualization, decision making) in the IoT machining platform located in the upper, cloud level. By linking these two levels a complex cyber-physical machining system is formed. During machining, the two level system collects the signals from vision system and employs them for surface roughness monitoring and feedback control actions. The sensor signal pre-processing is executed on the local machine level. The sensor data are collected, reduced, transformed into data packages and transferred to the IoT machining platform over the local area network (LAN). The cloud machining platform accepts the signal packages, processes the signals, saves the data, assesses the cutting chip size, calculates the chip size average, predicts the machined *Ra*, visualizes the machining data and selects the control actions in order to monitor the machining process. After all the listed tasks have been performed, the IoT platform sends back the control actions/decisions signals with the graphical representation of monitoring results to the lower machine level (local communication terminal). The executed control actions with alerts and explanations are visualized for machine tool operator on the control panel of the local terminal. The local terminal serves as a communication link between CNC unit, machining IoT platform and machine tool operator.

2 CLOUD BASED MACHINING PLATFORM

The IoT machining platform serves as the monitoring platform by using the advantages of the cloud capabilities such as outsourcing signal processing activities, graphical data visualisation, process value predicting and cognitive control decision making. The IoT machining platform is connected to the private machining cloud LAN.

The machining platform consists of seven parts. The first part is an IoT gateway which implements security, enables communication bridging, collects the enormous amount of sensorial data and filters data volume. These are edge computing activities. The IoT gateway collects the pre-processed data and reduces it to the amount needed by the monitoring process. The data is sorted according to the time filter. The data ends up in a machine tool business system, where it is combined with existing machine tool system data such as meta data or transaction data (part 2). In the third part, further signal processing is carried out in order to extract the relevant features for surface roughness monitoring process. For this purpose, an IoT application is built to detect the cutting chip size as relevant feature from the acquired sensor data. The fourth application is used to estimate the surface roughness *Ra* through ANFIS based prediction approach. The fifth application calculates the chip size. The sixth application is used for cognitive control actions such as process parameters corrections. The final application performs the graphical data visualization.

2.1 Application for Cutting Chip Size Acquiring

A sensor signal feature (cutting chip size) which provides the adequate information about the machined *Ra* is extracted from the pre-processed sensorial data in this IoT application.

An algorithm for cutting chip size acquiring was developed In Labview and is described in the research [14]. The five main steps (a-e) of the algorithm are

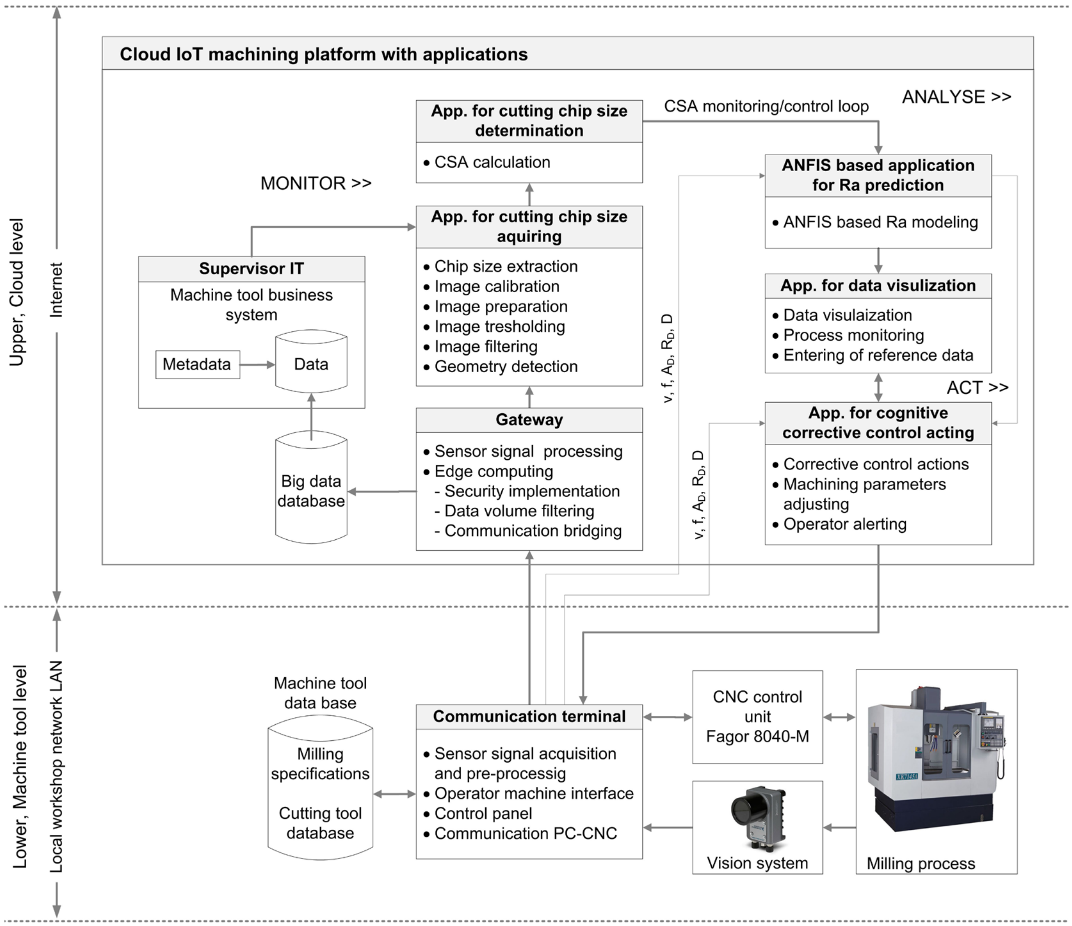

Fig. 1. *The basic structure of the two level CPMS*

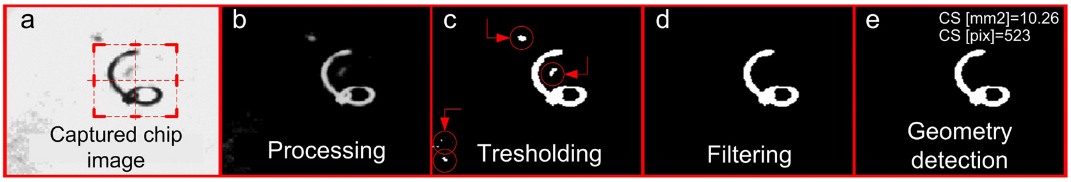

Fig. 2. *Steps of the cutting chip size acquiring algorithm*

presented in Fig. 2. Fig. 2 shows the result of the chip image capturing, processing, tresholding, filtering, geometry detection and variable determining process. Data transition between the IoT applications is accomplished via 6 system variables which contain data of the acquired chips for particular iteration of detection.

2.2 Application for Cutting Chip Size Determination

The optical sensor detects a great number of chips with diverse sizes; hence the determination of the chip size average (CSA) is required. The *CSA* is determined based on shift registers and system variables for every 25 consecutive detected cutting chips. The number of samples for calculating of the *CSA* is arbitrary defined in the range from 2 to 70 on the control panel for *Ra* monitoring and *CSA* control (Fig. 3).

The vision system is able to precisely detect chip sizes in the range from 0.05 mm² (CS_{min}) to 250 mm² (CS_{max}).

The *CSA* actually represents average surface of the chips projections in mm² on the plane perpendicular to the optical axis of the vision system. Therefore, the *CSA* depends on the shape and size of the chips. The shape of the chip depends on the chip thickness ratio, cutting speed, feed rate, depth of cut, workpiece material, workpiece surface quality, lubricant, tool material and tool geometry [15].

Many performed analyses of machining of NiCrMo heat-treated alloy steel, showed that there are relationships between the chip size and cutting conditions [16]. Therefore, in future research, it would be sensible to determine with intelligent modelling methods (ANFIS or genetic programming) the correlation between the *CSA* and cutting parameters.

The tool wear causes changes in tool tip geometry and changes on the tool flank surface. Both have significant influence on the chip forming process and chip geometry [17]. The changes in the geometry of the machined chips with the progress of tool wear for given cutting conditions were investigated in the study of Dargusch et al. [17]. Significant change in chip geometry was observed in the chips which were produced first with the new tool and then with the worn tool. It was also found that the chip geometry changes with an increase in the volume of material removed, which is believed to be the result of progressive changes in the tool geometry and an increase in cutting temperature due to tool wear [18]. Since the *CSA* is correlated with geometry and size of the chip, the tool wear has a significant impact on the *CSA*.

The *CSA* value is the input to the ANFIS based application for *Ra* prediction, the application for data visualization and the application for cognitive corrective control acting. The *CSA* value is connected with the indicator on the human machine interface.

2.3 ANFIS Based Application for *Ra* Prediction

The second platform application is devoted to on-line predict the *Ra* by automatically finding the connections between machining parameters, *D*, *CSA* and *Ra*. The testing error of the developed model was found to be less than 4 %. The detail adaptive neural fuzzy inference system (ANFIS) architecture employed for *Ra* prediction procedure is shown in Fig. 4.

The ANFIS model is developed based on training. The internal structure of the finished model is fixed, thus it acts as deterministic model where the input data vector always returns a specific output *Ra* value. The performance of ANFIS prediction mainly depends on the completeness of the input data. It is, therefore, necessary to evaluate the ANFIS performance via various calibration samples in order to estimate the model uncertainty caused by changes in input data.

In order to calculate the uncertainty in the *Ra* prediction, a Monte Carlo (MC) simulation is performed by running the *Ra* model many times either varying randomly the input data (training and validation set) or the training parameters (neural weights), or a combination of both.

The ANFIS system has been incorporated into the MC sampling structure as prescribed by Marcé et al. [19]. Three main steps are performed in prescribed procedure: multiple constituting a random vector

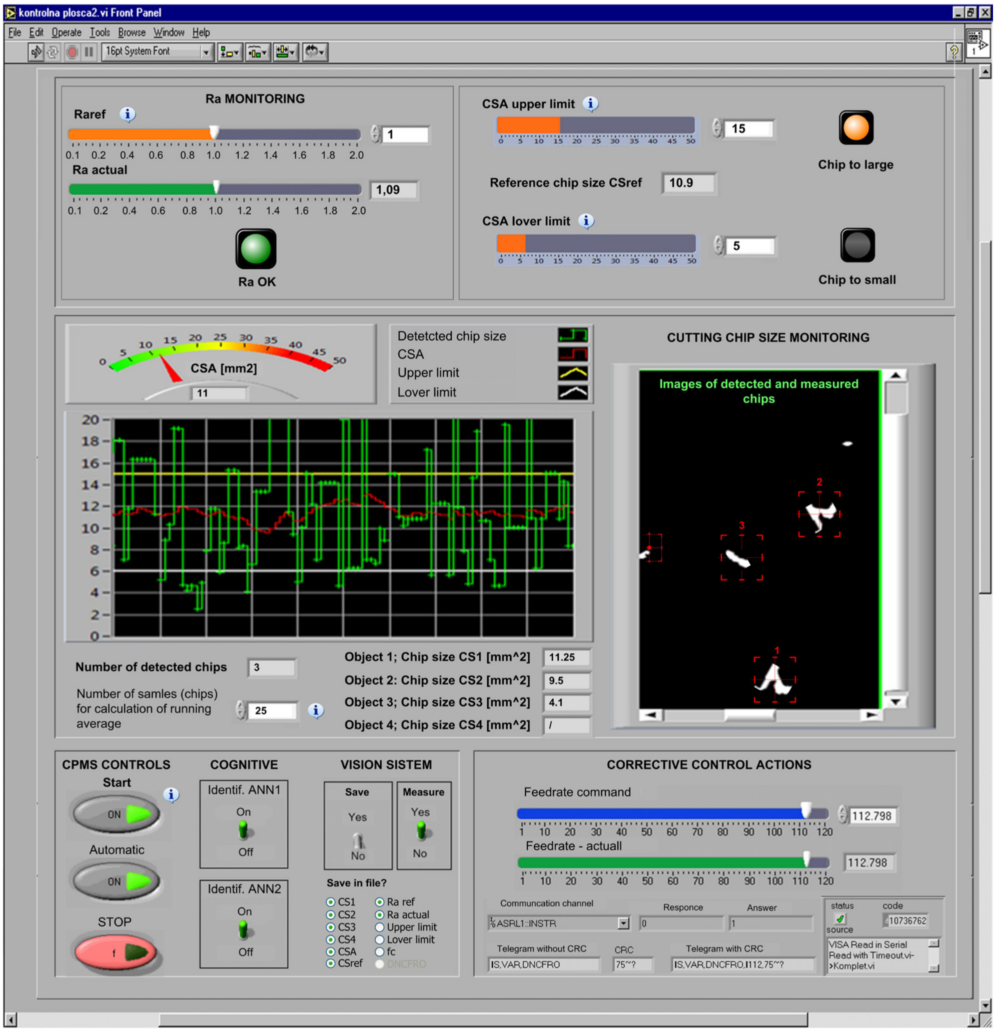

Fig. 3. *Graphical user interface for Ra monitoring and CSA control*

of parameters from their probability distributions, assessing the output (*Ra*), computing the statistics of the output and plotting the distributions of resulting statistical performances. The uncertainty of the model estimations of the measured and predicted *Ra* during the training and testing process has been determined by estimating the confidence intervals of simulation outputs. The 95 % confidence intervals are determined by finding the 2.5th and 97.5th percentiles of the associated distribution of the simulation results.

The results of the MC simulations indicate that almost all of predicted *Ra* values are within the 95 % confidence intervals. The simulation results reveal that the ANFIS prediction model sometimes underestimated the values of *Ra* during machining at small feed rates and at small chip sizes. However, just a 1.8 % of the predicted-observed values were found above the upper bound. The extent of these intervals with respect to the observed values was 92 %.

The low model accuracy at small feed rates and small chip sizes is probably due to the missing values in the training data set which created the model too sensitive. The second reason is the inability to produce appropriate fuzzy rules based on training data.

The investigation of the uncertainty attributed to the ANFIS structure would require large computational effort; therefore it is not examined in this study. It is also assumed that the model structure and the input data are correct.

The uncertainty of the predicted results, obtained from the proposed methodology, can be characterized as small, hence it can be concluded that the ANFIS adequately predicted the *Ra*. The average percentage prediction error of the trained ANFIS model is less than 3.7 %.

The monitoring process is based on visual sensor signal acquisition of the CS. Sensor signals are sent to the gateway on the cloud machining platform. The gateway sequentially buffers the sensor signal parts, which are then transported to the application for the extraction of the relevant cutting chip features by using wavelet packet transform method. The extracted features are fed into the application to determine the *CSA*. The *CSA* together with the cutting conditions from the local communication terminal are fed into the ANFIS system for *Ra* prediction. The output from the ANFIS is *Ra* in micrometers. The *Ra* monitoring is performed twice per second. When the predicted *Ra* exceeds the desired surface roughness (*Raref*), the monitoring output is sent to the application for cognitive corrective control acting. The latter alerts the machine tool operator via the application for visualisation or sends the corrective control commands to CNC control in order to adjust the machining parameters via DNC control functions. The application for data visualisation visualises the alert with the indicators that the upper *Ra* boundary has been exceeded.

2.4 Application for Data Visualization

This application is built as a human machine interface in order to visualize a large amount of captured data from the sensor. It also serves as a control panel for *Ra* monitoring and *CSA* control system. Fig. 4 shows the graphical user interface (GUI) of the developed application, built in Labview. The input to the application is the reference *Ra* or the range of the *CSA* which is entered by two graphical sliders in an upper right part of the GUI. Three warning indicators inform the user about the exceeded value of the machined *Ra* and unsuitable cutting chip size. The centre part of the GUI displays the acquired cutting chip images with the diagram of corresponding *CSA* values and the allowed chip size range. The GUI is projected on the local communication terminal.

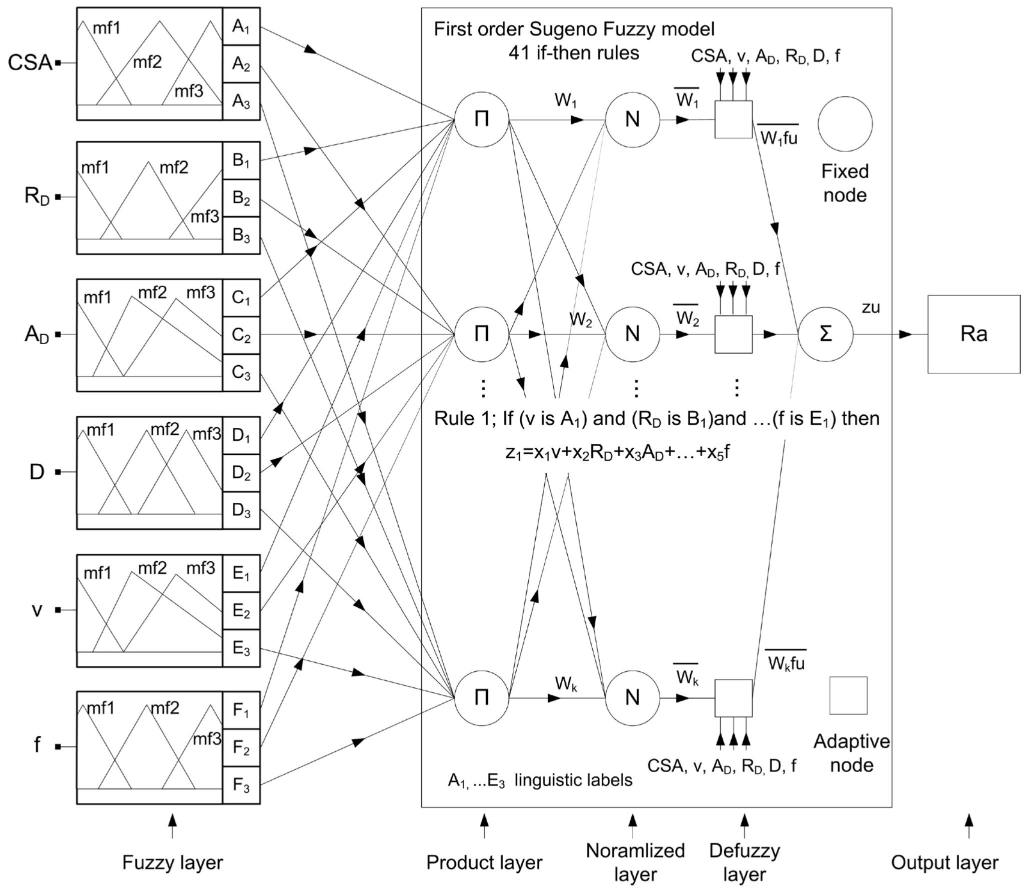

Fig. 4. *Structure of ANFIS based Ra predicting (multi–input Sugeno fuzzy model, generated rules, multi membership functions for each input)*

2.5 Application for Cognitive Corrective Control Acting

When the ANFIS based application predicts the *Ra* and the user enters the Ra_{ref}, the cognitive corrective control actions are taken in this application. Application is built as a cognitive control system and has adaptive process parameter adjustment capability. If the significant change of the *CSA* is identified, the control actions are taken within 10 ms after the occurrence. Three steps are required to execute a control action: In step one, the reference module A1 predicts the *CSref*. The A1 is the inverse model of the model located in the cloud ANFIS based application for *Ra* prediction. In step 2, the feed rate adaptation is performed. During this stage, the cognitive control system adjusts the feed rate values in order to minimize the difference between *CSref* and *CSA*. Finally in the last step the *f* value is sent to the application for data visualization and to the local communication terminal, where the feed rate command telegram is built and forwarded to the CNC control unit.

Fig. 5 shows the block diagram of the application for cognitive corrective control acting.

The principal control acting principle is based on a cognitive neural control system (CNCS). Its general structure consists of two elements and is depicted in Fig. 5.

The first part of the CNCS is a conventional control loop known as external feedback. The second, fundamental part is a sub-system of two connected artificial neural networks (ANN) with self learning capabilities. The loop connected with neural network 1 (ANN1) works as an internal feedback loop which is faster than the external feedback loop due to sensory delays.

The ANN1 monitors the process input *f* and output *CSA* and learns the process dynamics. When trained on-line, it can precisely predict the process output *CSA**. It operates as the cognitive process dynamics identifier. The second artificial neural network (ANN2) learns the process inverse dynamics and monitors the *f* and the *CSref*. After on-line training, it can predict appropriate *f** based on received input command *CSref*. *f**and *CSA** are the predicted process input and output by the two neural networks.

The CNCS acts as follows. The external feedback which assures a conventional feedback signal to control the milling is efficient particularly in the training phase. In this phase, the ANN1 learns the process dynamics and the ANN-2 learns the inverse

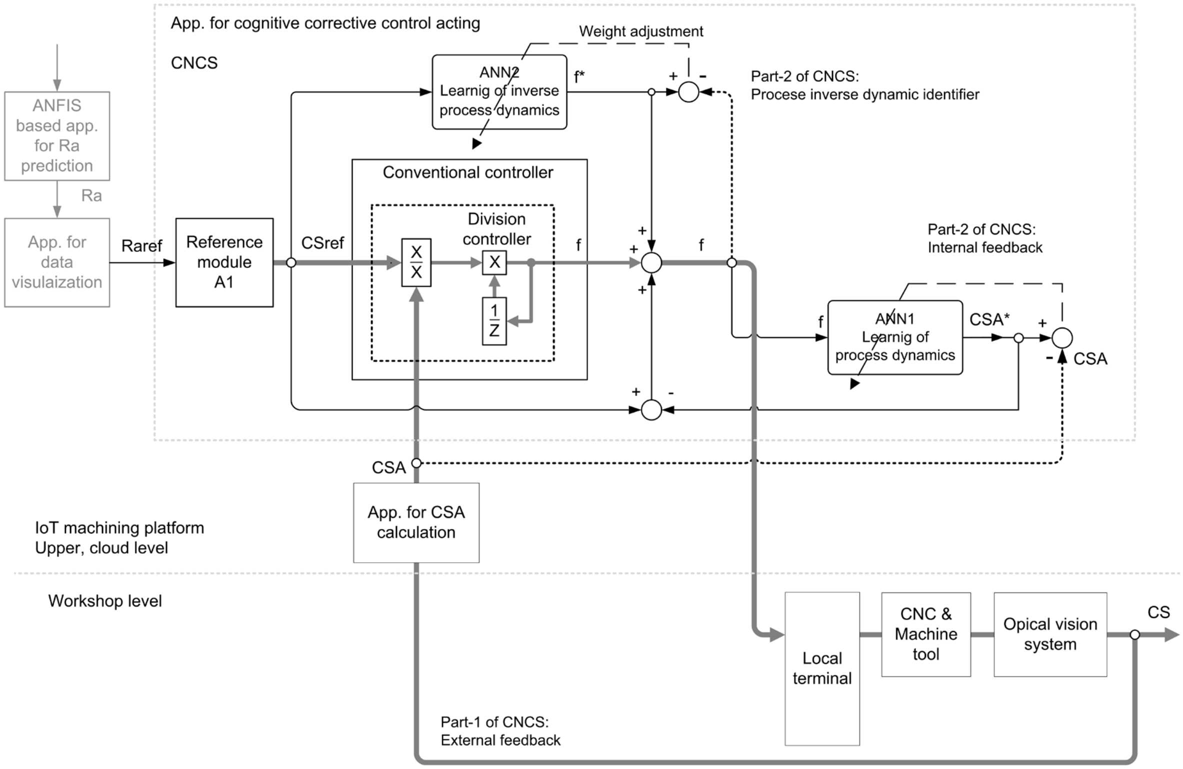

Fig. 5. *General block diagram of the neural control system*

dynamics. As training progresses, the internal feedback progressively prevails over the external feedback. After a certain learning stage, the ANN2 will completely substitute the external feedback control. The result is that the milling process is controlled above all by the feedforward controller. To automatically learn the process dynamics and inverse dynamics in the CNCS, two four-layer feedforward ANN were employed. The architecture of these two ANNs is described in the work of Zuperl and Cus [12].

The employed conventional controller is very well known division controller which is very easy to implement and has fast response. The control algorithm determines the new feed rate corrective command based on previous command and the quotient between the *CSref* and the *CSA*.

3 LOCAL COMMUNICATION TERMINAL

The communication terminal serves as an interface for the local machine tool operator and as a communication link between CNC unit and the gateway on the cloud machining IoT platform. The local terminal visualizes the condition of machining process, displays the results of cloud machining platform monitoring, shows the performed control commands and displays the alerts. The terminal is also employed to pre-process the optical sensor signals, to transfer the sensor signals to the cloud platform and to send the control telegrams to the CNC control unit. During signal pre-processing, thousand of information bits from the optical sensor are collected and reduced by removing the transient conditions. The pre-processed signals are then transmitted via hyper text transfer method to the cloud machining platform in order to perform the surface roughness monitoring process.

4 EXPERIMENTAL DEMONSTRATION

To test the feasibility of the cloud based machining platform for monitoring of end-milling, one successful cutting experiment with variable milling depth has been carried out, in which the axial depth of cutting is varying between 4.75 mm and 9.5 mm.

The workpiece material is a 16MnCr5 steel. The shape of the workpiece consists of two steps and two ramp parts, as shown in Fig. 6. The machining of these four parts of the workpiece has been performed in order to evaluate the stability and robustness of the CNCS to control the *CSA*. The cutting experiment has been carried out using the CNC machine tool Heller equipped with an optical vision system. A vision system consisting of a high speed smart camera NI 1772C was used to acquire useful information for *Ra* monitoring and *CSA* control from the cutting chip images. The maximum output is 64.995 frames per second (fps). The data are transferred to the cummunication terminal via giga ethernet cable. A ball-end milling tool of 16 mm diameter was used. After machining, the machined *Ra* was examined off-line by 7061 MarSurf PS1 surface roughness tester. The tester has 8 nm resolution at 0.09 mm vertical range. The objective of the cutting experiment is to keep the *Ra* constant by minimizing the error between the *CSref* and process output *CSA*. The initial *Raref* was chosen equal to 1.9 µm and the permitted control error was set to be less than 5 %. Based on the *Raref*, the *CSref* was set to 2.9 mm^2 according to the prediction module A1. The spindle speed (n) is set to 985 rpm, and the radial depth of cut (*RD*) is set to 8 mm. To achieve the *Ra* of 1.7 µm, the *CSA* must be fixed at 2.9 mm^2 and the feed rate must be below 835 mm/min. The starting feed rate command was set to 835 mm/min with allowable adjusting rate in the range form 400 mm/min to 1050 mm/min. The cutting experiment was started first without and then with the CNCS control. The result of the cutting experiment is presented in Fig. 6. The cutting experiment started with conventional cutting of the ramp part of the workpiece (0 mm to 40 mm). The feed rate was kept constant. Without adjustment of feed rate, the *CSA* changed from 13.5 mm^2 to 8.5 mm^2 and the *Ra* decreased from 2.02 µm to 1.88 µm. Fig. 6a shows the response signal of the *Ra*. Fig. 6f presents the *CSA* response. The control action was employed at t = 2 s (position B). In the ramp part (45 mm to 70 mm), the feed rate was adapted according to the value of the *CSA*. Firstly, the CNCS reduced the feed rate to 665 mm/min, as shown in Fig. 6i. As the A_D decreased continuously, the feed rates increased accordingly and thus maintained the *Ra* at 1.7 µm. During cutting of the ramp part (segment A-B), the *CSA* is kept constant so that the *Raref* can be attained. Fig. 6f and g show the *CSA* variations without and with control action. The results indicate that the *CSA* control system operated well and had advantage over non-control. When, at the position C (L = 70 mm), the tool partially run into a step, a high peak of the *CSA* appeared and the f decreased suddenly to keep the *Ra* at 1.7 µm. The CNCS was capable to compensate the induced perturbation. Fig. 6c shows the *Ra* response. Fig. 6m shows the corresponding f response. The feed rate dropped to the value between 460 mm/min and 510 mm/min to maintain the *CSA* average at 2.95 mm^2. At the tool engagement, the maximum *CSA*

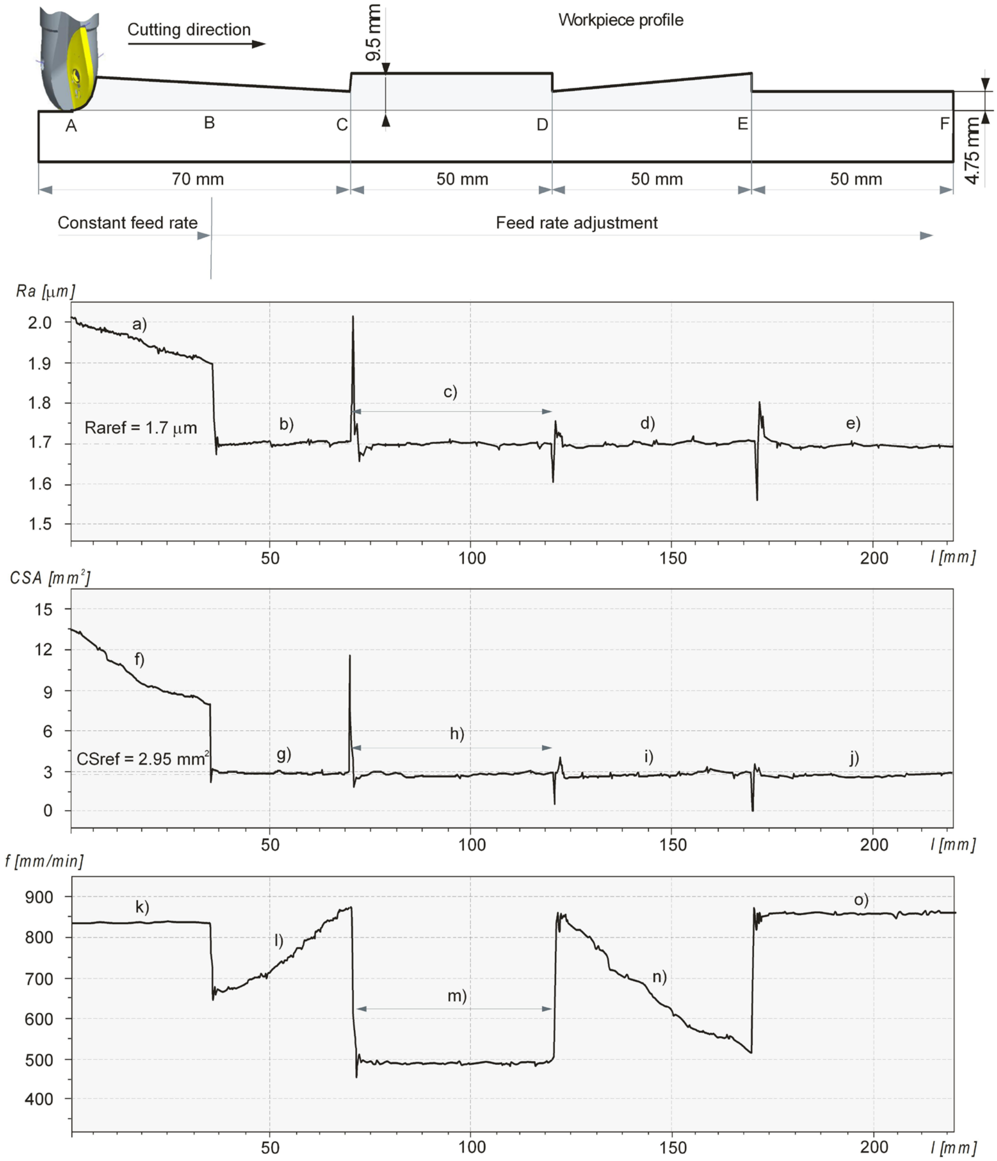

Fig. 6. *Cutting experimental results of Ra, CSA and feed rate control command responses to the variable axial depth of cutting*

was 11.6 mm2 and during the pass it was 2.95 mm2. In the range of step part (70 mm to 120 mm) where AD is maximal, the feed rate command was almost constant. Fig. 6h shows the response of the *CSA*. At the position D (L = 120 mm) where the A_D decreased, f increased suddenly to keep the *CSA* at the desired level. When the cutter encountered the slope, the feed rate started to decrease. In the ramp part (position E, L = 170 mm), where the A_D fell, f increased suddenly. When the tool is out of the step, the feed rate control signal stabilized at 857 mm/m. In the range of step part (170 mm to 230 mm) where the A_D is 4.75 mm, the feed rate command was nearly constant after the transitional stage.

During the cutting experiment the ***CNCS*** manages to return the *CSA* to the reference chip size within 0.48 s. The CPMS performs the *Ra* monitoring loop every 0.07 s.

The cutting experiment outlined that the *Ra* is kept constant by regulating the *CSA*.

5 CONCLUSIONS

In this paper, a cyber-physical machining system CPMS has been employed with the aim of monitoring the surface roughness by controlling the cutting chip size. The two layered complex CPMS was realized by integrating the cloud based IoT machining platform for process control to the machine tool with the visual system. The machining platform with the IoT applications offers instant on-line chip size and surface roughness monitoring based on visual sensorial data acquired at the workshop level and the ANFIS algorithm. Based on the cloud monitoring results, the cognitive neural control system CNCS determines the required corrective feed rate adaptation. The local communication terminal in connection with the CNC unit executes the cloud based corrective control actions.

The important advantage of the IoT machining platform is the increased distributed analytic and data storage/processing capacity which significantly improves the surface roughness monitoring efficiency and enable more robust corrective process control actions. The CPMS provides a novel way for controlling the cutting chip size and monitoring the surface roughness in milling processes through internet applications.

One cutting experiment with variable axial milling depth has been carried out to test the feasibility of the CPMS for surface roughness monitoring in end-milling. The results indicate the following:

- The proposed system, where the cloud computing resources and services are linked with the machine tool via hyper text transfer protocol, is feasible and could be efficiently implemented to monitor surface roughness during milling operation.
- The applied cloud based CNCS is stable which is reflected in improved surface quality.
- The application for cognitive corrective control acting manages to return the *CSA* to the reference chip size within 0.48 s.
- The corrective control actions are taken within 10 ms after the significant change of the *CSA* is identified.
- The optical cutting chip size detecting was successfully used to control the machined *Ra*.
- Controlled *Ra* does not deviate from the desired value for more than 10 %.
- The *Ra* is kept constant by regulating the *CSA*.
- The CPMS performs the *Ra* monitoring loop every 0.07 s.
- The uncertainty associated with the prediction of surface roughness can be characterized as small, hence the ANFIS could properly predict the *Ra*. Uncertainty analysis demonstrated that 98.2 % of predicted values fall within the 95 % confidence intervals. ANFIS in 1.8 % of cases underestimated the values of *Ra* at small feed rates and at small chip sizes. The extent of these intervals with respect to the observed values was 92 %.

The research limitations of the introduced concept are summarized from the viewpoint of cloud computing, chip size acquiring and ANFIS based modelling. The limitations are given as follows:

- Massive amount of data to be processed. To perform the real-time monitoring a large amount of data, due to a measurement technique with high sampling rate is required for cyber machining. The impact of this limitation on the monitoring results can be minimized by reasonable selection of sensor type to achieve optimal ratio between data resolution and data processing quality and by deliberate selection of computing services to ensure the quality of data analysis.
- Cyber security and privacy limitation. Since sensing data and information for monitoring and corrective process control acting are no longer stored on the local pc-terminal, security and privacy issues become more serious in the *CPS*. A possible solution to protect the security of devices connected in the CPMS requires more advanced network traffic encryption technique such as secure socket layer and the transport layer for security.
- Limited data transfer speed. The speed of Internet connection limits the data transfer speed and affects successive data analysis performed by applications in the cloud. A solution to this problem is to perform preliminary signal pre-processing at local personal computer terminal and to extract features with compact data size, which are then transferred to the cloud for further analysis.
- Optimal illumination in visual system. For the future chip size detection system, it is still a challenge to control the adjustment of optimal illumination, which is a decisive factor for the quality of the images captured by a visual system.
- Wet machining. The proposed CPS can not be applied for wet machining, since the visual system of cutting chip size detecting is not efficient in wet conditions.
- Amount of data for modelling. The surface roughness model has to be built for each specific cutting tool geometry and tool diameter. Therefore, an extensive experimental testing has to be performed. However, the advantage of the

ANFIS method is that the model can be trained and extended in real time during machining.

The special interest of future activities is to perform more tests with different cutting conditions in order to validate the proposed concept. Future work will be also directed to supplement the cloud platform with IoT applications for energy consumption monitoring and tool condition monitoring.

6 REFERENCES

[1] Wang, L., Törngren, M., Onori, M. (2015). Current status and advancement of cyber-physical systems in manufacturing. *Journal of Manufacturing Systems*, vol. 37, p. 517-527, **DOI:10.1016/j.jmsy.2015.04.008**.

[2] Wang, C., Ghani, S.B., Cheng, K., Rakowski, R. (2013). Adaptive smart machining based on using constant cutting force and a smart cutting tool. *Proceedings of the Institution of Mechanical Engineers, Part B: Journal of Engineering Manufacture*, vol. 227, no. 2, p. 249-253, **DOI:10.1177/0954405412466233**.

[3] Teti, R., Jemielniak, K., O'Donnell, G., Dornfeld, D. (2010). Advanced monitoring of machining operations. *CIRP Annals-Manufacturing Technology*, vol. 59, no. 2, p. 717-739, **DOI:10.1016/j.cirp.2010.05.010**.

[4] Chen, J.C., Huang, B. (2003). An in-process neural network-based surface roughness prediction (INN-SRP) system using a dynamometer in end milling operations. *The International Journal of Advanced Manufacturing Technology*, vol. 21, no. 5, p. 339-347, **DOI:10.1007/s001700300039**.

[5] Abburi, N.R., Dixit, U.S. (2006). A knowledge-based system for the prediction of surface roughness in turning process. *Robotics and Computer-Integrated Manufacturing*, vol. 22, no. 4, p. 363-372, **DOI:10.1016/j.rcim.2005.08.002**.

[6] Rao, K.V., Murthy, B.S.N., Rao, N.M. (2013). Cutting tool condition monitoring by analyzing surface roughness, work piece vibration and volume of metal removed for AISI 1040 steel in boring. *Measurement*, vol. 46, no. 10, p. 4075-4084, **DOI:10.1016/j.measurement.2013.07.021**.

[7] Oborski, P. (2014). Developments in integration of advanced monitoring systems. *The International Journal of Advanced Manufacturing Technology*, vol. 75, no. 9-12, p. 1613-1632. **DOI:10.1007/s00170-014-6123-x**.

[8] Marinescu, I., Axinte, D.A. (2011). An automated monitoring solution for avoiding an increased number of surface anomalies during milling of aerospace alloys. *International Journal of Machine Tools and Manufacture*, vol. 51, no. 4, p. 349-357, **DOI:10.1016/j.ijmachtools.2010.10.005**.

[9] Axinte, D., Boud, F., Penny, J., Gindy, N., Williams, D.J. (2005). Broaching of Ti-6-4–Detection of workpiece surface anomalies on dovetail slots through process monitoring. *CIRP Annals - Manufacturing Technology*, vol. 54, no. 1, p. 87-90, **DOI:10.1016/S0007-8506(07)60056-0**.

[10] Yang, L.-D., Chen, J.C., Chow, H.-M., Lin, C.-T. (2006). Fuzzy-nets-based in-process surface roughness adaptive control system in end-milling operations. *The International Journal of Advanced Manufacturing Technology*, vol. 28, no. 3-4, p. 236-248, **DOI:10.1007/s00170-004-2361-7**.

[11] Zhang, J.Z., Chen, J.C. (2007). The development of an in-process surface roughness adaptive control system in end milling operations. *The International Journal of Advanced Manufacturing Technology*, vol. 31, no. 9-10, p. 877-887, **DOI:10.1007/s00170-005-0262-z**.

[12] Zuperl, U., Cus, F. (2012). System for off-line feedrate optimization and neural force control in end milling. *International Journal of Adaptive Control and Signal Processing*, vol. 26, no. 2, p. 105-123, **DOI:10.1002/acs.1277**.

[13] Čuš, F., Župerl, U. (2015). Surface roughness control simulation of turning processes. *Strojniški vestnik - Journal of Mechanical Engineering*, vol. 61, no. 4, p. 245-253, **DOI:10.5545/sv-jme.2014.2345**.

[14] Zuperl, U., Cus, F. (2015). Simulation and visual control of chip size for constant surface roughness. *International Journal of Simulation Modelling*, vol. 14, no. 3, p. 392-403, **DOI:10.2507/IJSIMM14(3)2.282**.

[15] Shaw, M.C., Cookson, J.O. (2005). *Metal Cutting Principles (vol. 2)*, Oxford university press, New York.

[16] Fenton, R.G., Oxley, P.L.B. (1969). Mechanics of orthogonal machining: predicting chip geometry and cutting forces from work-material properties and cutting conditions. *Proceedings of the Institution of Mechanical Engineers*, vol. 184, no. 1, p. 927-942, **DOI:10.1243/PIME_PROC_1969_184_068_02**.

[17] Dargusch, M.S., Sun, S., Kim, J.W., Li, T., Trimby, P., Cairney, J. (2018). Effect of tool wear evolution on chip formation during dry machining of Ti-6Al-4V alloy. *International Journal of Machine Tools and Manufacture*, vol. 126, p. 13-17, **DOI:10.1016/j.ijmachtools.2017.12.003**.

[18] List, G., Sutter, G., Bouthiche, A. (2012). Cutting temperature prediction in high speed machining by numerical modelling of chip formation and its dependence with crater wear. *International Journal of Machine Tools and Manufacture*, vol. 54-55, p. 1-9, **DOI:10.1016/j.ijmachtools.2011.11.009**.

[19] Marcé, R., Comerma, M., García, J.C., Armengol, J. (2004). A neuro-fuzzy modeling tool to estimate fluvial nutrient loads in watersheds under time-varying human impact. *Limnology and Oceanography: Methods*, vol. 2, no. 11, p. 342-355, **DOI:10.4319/lom.2004.2.342**.

Strojniški vestnik - Journal of Mechanical Engineering 65(2019)2, 78-86

DOI:10.5545/sv-jme.2018.5614
Original Scientific Paper
Received for review: 2018-06-28
Received revised form: 2018-10-25
Accepted for publication: 2018-11-28

An Analysis of the Surface Geometric Structure and Geometric Accuracy of Cylindrical Gear Teeth Manufactured with the Direct Metal Laser Sintering (DMLS) Method

Jadwiga Małgorzata Pisula – Grzegorz Budzik – Łukasz Przeszłowski
Rzeszow University of Technology, The Faculty of Mechanical Engineering and Aeronautics, Poland

This paper presents findings concerning the accuracy of the geometry of cylindrical spur gear teeth manufactured with the direct metal laser sintering (DMLS) method. In addition, the results of the evaluation of the tooth surface geometric structure are presented in the form of selected two-dimensional and three-dimensional surface roughness parameters. An analysis of the accuracy of the fabricated gear teeth was performed after gear sand-blasting and gear tooth milling processes. Surface roughness was measured before and after sand-blasting and gear tooth milling. The test gear wheel was manufactured from GP1 high-chromium stainless steel on an EOS M270 machine.
Keywords: direct metal laser sintering (DMLS) method, surface geometric structure, cylindrical spur gears, geometric accuracy

Highlights
- *An analysis of the geometric accuracy of a cylindrical spur gear made with the additive DMLS method allows us to appropriately select assumptions for the finishing process using cutting machining techniques.*
- *Sandblasting does improve the geometric structure of the surface of the gear, and the results comply with the manufacturer's data.*
- *The geometric structure of the gear tooth surface after the milling process using a universal tool is better than given in the manufacturer's data.*
- *The accuracy of a cylindrical spur gear fabricated by means of DMLS from GP1 material is classified outside accuracy class 12.*
- *Sandblasting does not improve the accuracy of gear teeth.*
- *The application of a universal tool for gear tooth machining of gears manufactured by DMLS reaches accuracy class 8 according to DIN 3962-1,2.*
- *Cylindrical spur gears made with the additive DMLS method and subjected to cutting machining may be used in single-piece and small-volume production.*

0 INTRODUCTION

The interest in three-dimensional (3D) printing of metallic material is constantly growing. Competition between various manufacturers and suppliers of machines using additive techniques encourages them to offer increasingly improved and more automated products, which inspires the search for new technologies. In addition, printing offers new geometric possibilities in terms of the design of the parts. Fabricating inner cooling channels of continuous design, openwork patterns or honeycomb structures has become a reality. The aircraft industry is already implementing such technologies, closely followed by the automotive sector [1].

The direct metal laser sintering (DMLS) method is an additive technology of fabricating parts from metal and a practical alternative to components manufactured by casting. Shorter single-piece or small-volume manufacturing time is a benefit of fabricating a part on the basis of a 3D computer-aided design (CAD) model. In manufacturing, DMLS provides precise, functional, and durable parts. Interest in the technology is confirmed by publications concerning microstructures and the mechanical properties of molten material. For example, in the papers [2] to [4], the results of experiments aimed at determining the mechanical properties of samples obtained with the DMLS method for various metallic powders are presented. In addition, works [3] and [4] investigated the impact of fabrication orientation, surface polishing upon mechanical behaviour of metallic alloys and their microstructural properties. In the paper [5], the microstructure and elemental composition stainless steel powder have been examined. In [6], the author studied the effect of processing parameters on the densification and microstructural evolution during direct laser sintering of metal powders. The sintering process and the resultant mechanical strength of nickel nanoparticles were studied in the paper [7] using molecular dynamics simulations. In work [8], the size and volume fraction of SiCp have been varied to analyse the crack and wear behaviour of the Al-based composite. Only in some studies do we find guidelines

*Corr. Author's Address: Rzeszow University of Technology, The Faculty of Mechanical Engineering and Aeronautics, Poland, jpisula@prz.edu.pl

on the selection of parameters of the melting process and their effect on the properties of the final product. The paper [9] describes how an optical in-process monitoring system for DMLS process can be set up and used for purposes of understanding the process and quality assurance. In work [10], the authors optimized the process parameters, such as the laser scan rate and scanning pattern, to obtain high-density parts of multicomponent iron base powder blend. In work [11], important parameters and restrictions in the production of customized titanium implants are described. Such publications rarely contain any information on designing parts fabricated with the DMLS method or the evaluation of the usefulness of printed parts. In work [12], how to manufacture isoelastic dental implant materials with optimized surface properties is reported, and in [13] how to provide complete control over the microarchitecture of porous titanium implants is described.

Depending on the application, gear transmissions should be characterized by suitable geometric and kinematic accuracy, as well as durability [14]. The structure of DLMS-fabricated gears is porous, which enables their impregnation by grease or the application of a layer improving the gear's strength [14]. This provides increased gear wear resistance and prevents excessive friction heating. In the present study, a set of cylindrical spur gears was made using the DMLS method. The gears were subsequently subjected to final cutting machining to produce an entirely adequate product. Next, the geometric accuracy of the gears was measured on a P40 by Klingelnberg coordinate measuring machine, and the geometric structure of the tooth surface at selected stages of the manufacturing process was analysed.

1 METHOD

1.1 The DMLS Method

DMLS (a registered trademark of EOS GmbH) is based on the laser beam melting (LBM) technology, a technique classified as power bed fusion process. Although the name DMLS contains the word 'sintering', this additive fabrication process uses a laser beam to fully melt metal particles [15]. Selective laser melting (SLM) is a more appropriate term for this process, but the name is a registered trademark of SLM Solutions. In the case under consideration, the EOS M270 machine uses Yb-fibre lasers. This type of laser provides an exceptionally high beam quality combined with performance stability [16]. The material is collected from a container and subsequently applied in the workspace in layers by means of a scraper. The thickness of the applied layer depends on the type of material in the container and may vary in the range from 0.01 mm to 0.08 mm. As the metal is fused, certain melting irregularities occur, which are removed by a blade attached to the scraper. Following the application of a particular layer of the material in the location of the fabricated model, a laser beam scans its geometry, fusing the metal across the respective sections of the model. After scanning the entire surface of a respective section of the model, the powder application and scanning process repeat in the entire powder bed. Correct model data processing and process simulation, which minimizes errors that may occur at the final stage of the additive process, play an essential role in the DMLS technique.

DMLS requires generating permanent anchoring structures due to the rapid contraction of metals after melting (due to a significant temperature difference between the atmosphere of the work chamber and molten metal). In this case, anchors prevent the metallic material from bending upwards due to a shrinkage caused by the material's phase transformations.

Materials commonly applied in the technique include aluminium, titanium, stainless steel, maraging steel, nickel alloys, and cobalt-chromium alloys [16].

1.2 Test Models

Test models were made on an EOS M270 machine on the basis of a 3D CAD-designed gear model, the profile of which was obtained by simulated machining [17]. Gear geometry parameters are included in Table 1. The choice of gear geometry was dictated by the dimensions of the EOS M270 machine's working die (250 mm × 250 mm, on which 9 parts were evenly distributed) (see Fig. 1). A small, odd number of gear teeth (z = 19) was intended to prevent tooth undercut and the presence of the gear to relevant axial planes.

Table 1. *Basic geometric data of the gear model*

Designation	Quantity
Number of teeth z	19
Normal module m_n	3.0 mm
Profile angle α_n	20 deg
Helix angle β	0.0 deg
Profile modification coefficient x	0.0
Clearance c	0.75 mm
Whole depth h	6.75 mm
Face width b	10.0 mm

Gears were modelled in several variants of allowance thickness, which resulted from the assumed technological process of gears and compensation for material shrinkage. Prior to melting, pre-production was performed, involving the use of the specialist software EOSTATE Magics RP by Materialise. This stage included preparing the model for the process and setting up the machine according to the manufacturer's recommendations. The preparation of the model included data processing (creating an .stl file of specific accuracy), determining the model's suitable location in the workspace and designing appropriate anchors.

Fig. 1. *A set of gears on the building platform after the melting process using the DMLS method*

Fig. 1 shows the gears after additive manufacturing. They are characterized by specific orientation with respect to each other and the machine's coordinate system. The assumed location of the gears on the building platform in the horizontal position resulted in a uniform structure of the gear's transverse plane, which is impossible when the gears are positioned vertically (which undoubtedly leads to tooth strength and stress variation along the circumference). In addition, in the case of vertical gear alignment, tooth geometry mapping on the circumference of the gear is uneven, and problems with post-processing arise. The use of special part marks made it possible, for example,. to carry out an analysis of the accuracy of model mapping depending on the machine's scraper location. Moreover, it enables testing the relationship between tooth strength and tooth location on the work platform as well as the parameters of the stress-relief process.

The EOS StainlessSteel GP1 material used for fabricating the gears consists of high-chromium stainless steel, the chemical composition of which complies with standard PN-EN-10027-2 steel 1.4542 [18]. GP1 steel is characterized by good mechanical properties, in particular, excellent ductility. The material is used in DMLS primarily for making functional prototypes of metal parts and finished products in single-piece and small-volume production, as well as for medical purposes. Parts made of GP1 stainless steel can be machined, welded, bead-blasted (sand-blasted), and polished; spark erosion and coating may also be applied [16]. Regarding the gear wheels, the material GP1 is used mainly in the chemical industry due to its anti-corrosive and self-lubricating properties, e.g., in gear pumps [19] and in drive systems of radial flow sedimentation tanks [20]. In this study, the smallest possible layer thickness in the processing of GP1 was 0.02 mm. The duration of the process depends on the number of layers applied and the size of the area which must be irradiated with a laser beam when fusing the subsequent layer. For the printed gear (as the semi-finished product with a pre-determined profile) the process lasted 9 h 34 min (see Fig. 2a). Important information on the process of fusing the gear model is shown in Table 2.

a)

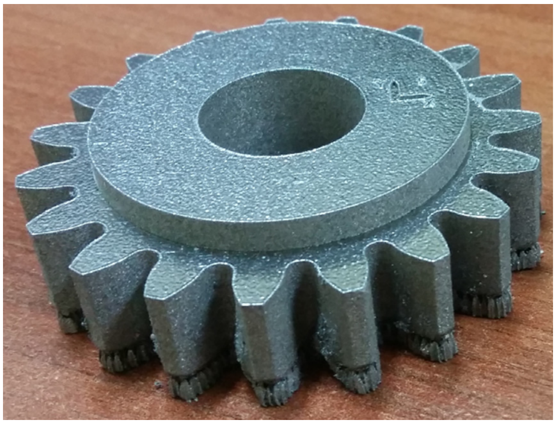

b)

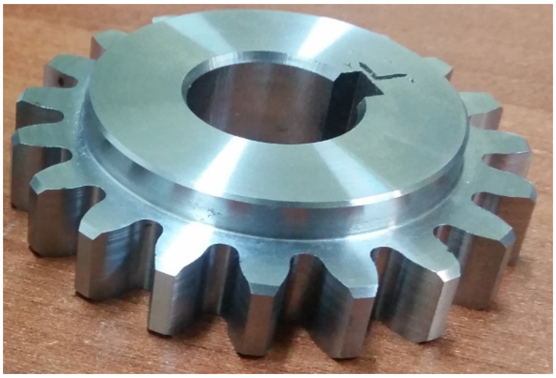

Fig. 2. *A test gear fabricated using the DMLS technology; a) after the melting process and after stress-relieving, and b) after the complete machining process*

Table 2. *Parameters used in melting the gear model (DMLS)*

Printer	EOSINT M270
Accuracy (p = 99.7%)	Parts are produced with the accuracy of ± 20 μm – 50 μm [16]
Material	GP1
Software	EOSTATE Magics RP by Materialise
Layer thickness	0.02 mm
Manufacturing time	9 h 34 min

After the additive manufacturing process, the post-processing stage begins. Apart from stress-relieving (to eliminate internal stress) and cutting the model off the building platform (by band-saw), post-processing included machining (dismantling anchors, machining datum planes and other surfaces, as well as tooth milling). A 3 mm shank-type end mill [21] was used in the gear tooth final milling process as a machining tool. The gear teeth machining process involved the application of contour milling, i.e., the cutting edges, placed on the cylindrical surface of the tool, was moving on the tooth gap profile of the gear defined directly in the CAD model. The entire removal machining process was performed on a CNC turning centre (ST-20Y by Haas). The parameters of the gear tooth milling process are shown in Table 3. The duration of the final machining was 4.1 min. In comparison, rough milling from a solid block in the gear lasted 41.05 min.

Table 3. *Parameters used in the machining process (Gear teeth milling process)*

Cutter machine	CNC turning centre ST-20Y by Haas
Tool	end mill VHM VHTS ϕ 3.0 mm × 6 mm × 10 mm × 57 mm, 4 flute (Van Horn)
Material	GP1 (EOS StainlessSteel GP1)
Cutting speed V_c	57.0 m·min^{-1}
Feed per tooth fn	0.005 mm·tooth^{-1}
Depth of cut ap	0.02 mm
Spindle speed n	6000 rpm
Duration of the final machining	4.1 min

Some gears were sand-blasted to evaluate the suitability of the process in terms of tooth geometry and surface geometry structure. In the sandblasting process Brown Fused Alumina (BFA) grain F80 according to FEPA 42 D 1984 Teil 2 standard was used. A gear after a complete machining process is shown in Fig. 2b.

1.3 Measurement of the Models

Gear measurements at each stage of the manufacturing process were performed on a P40 coordinate measuring machine by Klingelnberg, which utilizes a contact method for measurements. In this method, geometric features of the test object are measured on the basis of a set of measurement points, acquired by the coordinate measuring machine (CMM) by means of contact (probing) heads, as well as scanning heads in a single coordinate system without the need to adjust the mounts fixing the object. Gear geometry and parameters characterizing the gear blank and the tooth geometry are acquired by means of special software for, respectively, axial-symmetrical elements and cylindrical gear measurements. The selected machine parameters P40 of the Klingelnberg used for gear measurements are presented in Table 4.

Table 4. *Parameters used to measure the gears*

Measuring machine	Klingelnberg Gear Measuring Centre P40
Probe System	K3D (M44)
Resolution	<0.01 mm
Probe, head diameter	1.5 mm
Evaluation range $L\alpha$ for the profile	7.0 mm
Evaluation range $L\beta$ for the lead	10.94 mm
Length measurement uncertainty	according to VDI /VDE 2617 U1 = 18+ L /250 [mm] L = length in mm
Teeth to be checked (profile, lead)	3 teeth (evenly around the gear circumference)

The measurements were performed in order to determine the accuracy of cylindrical spur gears made by means of the DMLS technology. Gears were tested after melting, tooth sanding, and tooth milling. In each case, the same datum references were considered, i.e., the cylindrical surface and the end face.

An evaluation of the accuracy of the geometric surface structure of gear teeth fabricated using the DMLS technology at selected stages of the manufacturing process was performed. Tooth flank topography measurements were taken by means of the contact method using a Talyscan 150 3D scanning instrument with a sample spacing of 5 µm in directions X and Y, and a measuring needle with a rounding radius of 2 µm. Surface topographies were recorded for an area of 2.5 mm by 2.5 mm so that the centre was located at the intersection of the pitch diameter in mid-width of the toothed ring. The measurement was performed in 501 passes, with 501 points recorded in a single pass with the speed of V = 2000 µm/s. Measurement data processing and the calculation of the topographic parameters of the analysed surfaces were performed in TalyMap Expert and Mountains Map Universal applications by the company Taylor Hobson. Due to shape removal and levelling issues, the area selected for analysis was narrowed down.

2 RESULTS AND DISCUSSION

2.1 An Analysis of the Accuracy of Teeth and the Datum Plane of the Gear

For the gear tooth accuracy assessment, parameters characterizing the tooth geometry that define the gear accuracy class [22] and [19] are considered. Table 5 contains the results of gear tooth measurements, in which only the parameters defining tooth profile, tooth line, and pitch accuracy class were provided after melting and sand-blasting without datum reference machining.

Table 5. Accuracy classes with values of class-defining of parameters: after melting and sand-blasting without datum reference machining [22]

	Profile accuracy class	Tooth line accuracy class	Pitch accuracy class
After melting	>> $f_{H\alpha} = -72.5\ \mu m$	>> $f_{f\beta} = 85.1\ \mu m$	12 $f_{p\,max} = 50.5\ \mu m$ $f_{u\,max} = 91.7\ \mu m$
After sand-blasting	>> $f_{H\alpha} = -73.3\ \mu m$	11 $f_{H\beta} = 48.1\ \mu m$ $f_{f\beta} = 34.5\ \mu m$	11 $f_{p\,max} = 40.9$ mm $f_{u\,max} = 62.0$ mm

Table 6. Accuracy classes together with class-defining parameters: before tooth machining and after milling with machined datum planes [22]

	Profile accuracy class	Tooth line accuracy class	Pitch accuracy class
Before tooth machining (after melting)	12 $f_{H\alpha} = -62.9$ mm $f_{\alpha} = 82.2$ mm $f_{f\alpha} = 63.0$ mm	>> $f_{f\beta} = 66.4$ mm	11 $f_{p\,max} = 34.6$ mm $f_{u\,max} = 47.9$ mm
After tooth milling process	7 $f_{H\alpha} = 7.3$ mm	7 $f_{H\beta} = 10.3$ mm $f_{f\beta} = 6.9$ mm	8 $f_{u\,max} = 12.8$ mm

A gear subjected to the melting process is outside accuracy class 12, according to DIN 3962. The main reasons are high values of the tooth profile position deviation ($f_{H\alpha}$) as well as large deviations of the tooth line position and shape ($f_{H\beta}$, $f_{f\beta}$). Despite a pitch accuracy class of 12 (maximum values obtained for the maximum unit pitch deviation $f_{p\,max}$ and the greatest pitch interval deviation $f_{u\,max}$), the gear class is determined by the results obtained from the tooth line and profile accuracy classes. Gear tooth accuracy after sanding is also outside the accuracy class due to the profile, whose position deviation ($f_{H\alpha}$) is as high as after melting. Sanding does not affect the profile position but instead improves other ratings of the tooth profile ($f_{f\alpha}$ is the tooth profile shape deviation and F_{α} the total profile deviation), i.e., by decreasing them. Sand-blasting enables only a slight improvement of the tooth line and the gear pitch, both of which attain accuracy class 11.

For the second set of gears fabricated with the DMLS technology, datum surfaces were machined by turning. The datum surfaces were the cylindrical surface of the hole and the butting plane of the gear hub. This is the butting plane from which the supporting structures were cut off. To make the datum surfaces, the gears were mounted in a three-jaw chuck covering the cylindrical and abutting surface of the hub, which was designed for this purpose. Next, the teeth were milled. When measuring gear teeth, the same datum references as in the previous gear set (cylindrical surface and end face) were considered. The mean radial and axial runout values for the datum planes after turning are 0.0062 mm and 0.0093 mm, respectively. Table 6 presents the results of gear teeth measurements, in which only the parameters determining tooth profile, tooth line and pitch accuracy class before tooth machining and after milling were provided.

Datum reference accuracy plays a vital role in tooth geometry measurements. A comparison of results from Tables 5 and 6 before tooth machining (after melting) and results with and without datum plane machining indicates an improvement (reduction) of the values characterizing the class of the tooth profile ($f_{H\alpha}$, $f_{f\alpha}$ and F_{α}), tooth line ($f_{f\beta}$) and pitch ($f_{p\,max}$, $f_{u\,max}$). Since tooth line accuracy is outside the class, the entire gear falls outside the accuracy class 12. The tooth milling process keeps the gear within accuracy class 8. The main reason is the high value of the greatest pitch interval deviation ($f_{u\,max}$). Tooth profile and tooth line are significantly improved; in both cases, accuracy class 7 was achieved.

2.2 An Analysis of the Accuracy of Tooth Geometric Surface Structure

Selected surface and profile parameters were used for the evaluation of two-dimensional and three-dimensional characterization of the surface structure and its directionality. Fig. 3 presents results obtained by means of the Talyscan 150 3D scanning instrument. Surfaces of the test samples were reviewed by analysing selected roughness parameters [23] or [24] shown in Tables 7 and 8.

The geometric structure of the surface after melting and sand-blasting can be described as non-oriented (random isotropic surface). Meanwhile, in the milled geometric surface structure, a periodic component – its presence related to traces left by individual mill bits – and a random component (mixed anisotropic surface) is manifested. *Sq*, *St* amplitude parameters, in line with expectations, decrease with the application of sand-blasting and milling. Skew index *Ssk* and concentration index *Sku* are sensitive to local hills or pits. The *Ssk* index for all test surfaces is very low; for negative values (fused surface), surfaces with rounded, plateau-like hills are indicated. A positive *Ssk* value suggests sharp-edged hills (sand-blasted and milled surfaces), although for the milled surface its value nears zero (0.00784). The Sku parameter value for all surfaces is close to 3, which means that ordinate distribution approaches a normal distribution. For a fused surface, the *Sku* parameter is 2.634 and displays lower concentrations than a normal distribution, while for a sand-blasted surface it shows greater concentrations (3.999).

The Abbott-Firestone bearing area curve (BAC) is most favourable for the milled surface, for which core roughness height *Sk* is 1.2034 µm, whereas reduced hill height *Spk* and reduced pit depth *Svk* have similar levels. Key 2D roughness parameters were specified in the direction perpendicular to the projected (theoretical) line of contact of gear teeth in meshing. After the sand-blasting process, the *Ra* parameter is 3.474, which complies to the *Ra* value specified by

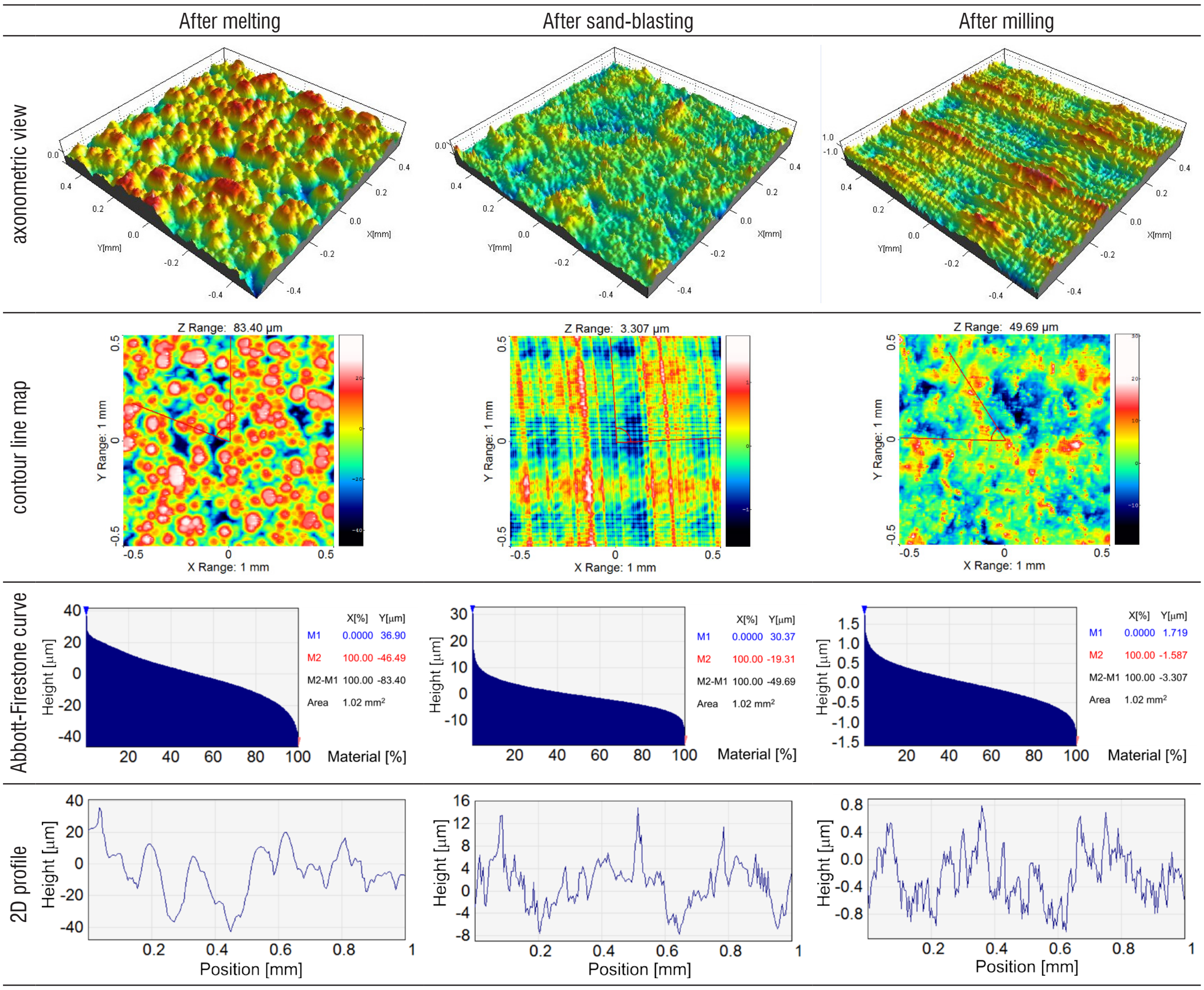

Fig. 3. *Micro-geometry of test surfaces*

the manufacturer (2.5 µm to 4.5 µm). Likewise, the *Rz* parameter is contained within the range of 15 µm to 40 µm [16]. A satisfactory value of the *Ra* parameter (0.387 µm) was obtained after milling, as it had been assumed that *Ra* for the tooth flank surface would be 1.6 µm. The distribution of profile ordinates reveals a concentration index (*Rku*) of 2.3156, which allows us to conclude that the distribution deviates from normal (i.e., is more flattened) and demonstrates left-sided asymmetry (most results above the mean), with the skewness index *Rsk* equal to -1.1516.

Table 7. *Surface roughness parameters*

Parameters	Surface after printing	Surface after sanding	Surface after milling
Sa [µm]	11.292	3.863	0.37097
Sq [µm]	13.931	4.9732	0.46429
Ssk [-]	–0.29245	0.47266	0.078346
Sku [-]	2.635	3.9992	2.95
Spk [µm]	7.6112	7.2297	0.51499
Sk [µm]	36.797	11.775	1.2034
Svk [µm]	14.133	3.9158	0.39615
Sz [µm]	83.397	49.687	3.3066

Table 8. *Profile roughness parameters*

Parameters	Profile after printing	Profile after sanding	Profile after milling
Ra [µm]	12.478	3.475	0.38745
Rq [µm]	16.198	4.2962	0.46656
Rsk [-]	–1.0655	1.0232	–1.1516
Rku [-]	3.1495	3.4612	2.3156
Rpk [µm]	27.167	10.681	0.51309
Rp [µm]	35.7	14.799	0.78726
Rv [µm]	42.879	7.7116	1.0655
Rz [µm]	78.579	22.51	1.8527

3 CONCLUSIONS

Due to the complexity of the DMLS process, the correct use of workpieces depends on the knowledge of materials used in the process as well as mechanisms at work during the melting process. Correct model fabrication means the most accurate real-time geometry in reference to the geometry of the CAD model. To achieve this, the following conditions must be satisfied:

- correct data processing (selection of export parameters of models to STL format);
- correct preparation of the manufacturing process (e.g., generating anchoring structures);
- correct positioning of the component to be produced in the machine's workspace;
- allowances for post-processing operations.

In the analysed case of a spur gear, the application of the machining process, i.e., turning datum planes of the gear blank, gave appropriate results. The results obtained from measuring the gears after the melting process with datum reference machining were more accurate than the results obtained from the measurement of gears without datum reference machining. This is due to the form deviation of the datum surfaces. For both cases, after the melting process, the gears are outside accuracy class 12 according to DIN 3962. A similar conclusion may be drawn for the gear tooth milling process using a universal tool, which in this case was an end mill. This solution helps achieve gear accuracy class 8. It may be supposed that the application of specialist tooth machining tools, used in generating or profiling, should yield even a higher accuracy class. To fully evaluate the workability of the GP1 material, gear teeth must be tested after a corresponding heat treatment followed by grinding.

As expected, the parameters that characterize the geometric structure of the surface after tooth milling are reduced by 96.8 % in comparison to parameters obtained following the melting process. *Ra* profile parameter of 12.5 µm was reduced to 0.4 µm.

Sand-blasting helps achieve a far superior tooth surface geometry structure compared to the surface after printing, but it fails to significantly upgrade gear accuracy class.

Tooth measurements on a coordinate measuring machine after melting and sand-blasting demonstrated that the profile angle for the right- and left-hand sides is lower than assumed for the model (negative deviation of profile position). It can be caused by shrinkage of the material. Surface topography, not shown in this study, confirms the consistency of profile angle position deviation along the width of the ring. Moreover, cylindrical surface measurements on the gear's blank indicate that such surfaces are in fact elliptical. It was also observed that the shape deviations became larger with increasing distance of the workpiece from the central position on the building platform.

Manufacturing cost and time in additive methods often differ from those characterizing conventional manufacturing approaches. This is due to the specifics of additive manufacturing. In the analysed case, the manufacturing time for a gear wheel made by means of DMLS is ten times longer than that of manufacturing a single gear from full material. Meanwhile, the cost of manufacturing is over ten times higher than the cost of fabricating the same gear using conventional methods. The main cost drivers in the DMLS include materials, manufacturing, machine depreciation and labour. In spite of a preliminary gear wheel design, some post-processing is required, which significantly impacts part fabrication time and costs. Please note, however, that the analysed manufacturing method is far from inexpensive, but its cost-effectiveness increases with the complexity of the shape to be obtained [25]. The DMLS sintering process with appropriately selected parameters could be an alternative for manufacturing soft cylindrical gears in single-piece and small-volume production.

In further work, the authors intend to study the effect of gear positioning across the building platform on tooth strength.

4 REFERENCES

[1] Bremen, S., Meiners, W., Diatlov, A. (2012) Selective laser melting. A manufacturing technology for the future? *Laser Technik Journal*, vol. 9, no. 2, p. 33-38, **DOI:10.1002/latj.201290018**.

[2] Rontescu, C., Pacioga, A., Iacobescu, G., Amza, C.-G. (2016). Research on the mechanical properties of titanium biocompatible alloys obtained by sintering. *U.P.B. Scientific Bulletin, Series B: Chemistry and Material Science*, vol. 78, no. 2, 195-202.

[3] Mower, T.M., Long, M.J. (2016). Mechanical behavior of additive manufactured, powder-bed laser-fused materials. *Materials Science and Engineering: A*, vol. 651, p. 198-213, **DOI:10.1016/j.msea.2015.10.068**.

[4] Manfredi, D., Calignano, F., Krishnan, M., Canali, R., Ambrosio E.P., Atzeni, E. (2013). From powders to dense metal parts: Characterization of a commercial AlSiMg alloy processed through direct metal laser sintering. *Materials*, vol. 6, no. 3, p. 856-869, **DOI:10.3390/ma6030856**.

[5] Zhang, J., Zhang, Y., Guo, X., Lee, W. H., Hu, B., Lu, Z., Jung, Y.-G., Lee, H. (2016). Characterization of microstructure and mechanical properties of direct metal laser sintered 15-5 Ph1 stainless steel powders and components. *145th Annual Meeting & Exhibition: Supplemental Proceedings* John Wiley & Sons, Inc., Hoboken, **DOI:10.1002/9781119274896.ch2**.

[6] Simchi, A. (2006). Direct laser sintering of metal powders: Mechanism, kinetics and microstructural features. *Materials Science and Engineering: A*, vol. 428, no. 1-2, p. 148-158, **DOI:10.1016/j.msea.2006.04.117**.

[7] Zhang, Y., Zhang, J. (2016). Sintering phenomena and mechanical strength of nickel based materials in direct metal laser sintering process – A molecular dynamics study. *Journal of Materials Research*, vol. 31, no. 15, p. 2233-2243, **DOI:10.1557/jmr.2016.230**.

[8] Ghosh, S.K., Saha, P. (2011). Crack and wear behavior of SiC particulate reinforced aluminium based metal matrix composite fabricated by direct metal laser sintering process. *Materials & Design*, vol. 32, no. 1, p. 139-145, **DOI:10.1016/j.matdes.2010.06.020**.

[9] Grünberger, T., Domröse, R. (2015). Direct metal laser sintering - Identification of process phenomena by optical in-process monitoring. *Laser Technik Journal*, vol. 12, no. 1, p. 45-48, **DOI:10.1002/latj.201500007**.

[10] Simchi, A., Petzoldt, F., Pohl, H. (2003). On the development of direct metal laser sintering for rapid tooling. *Journal of Materials Processing Technology*, vol. 141, no. 3, p. 319-328, **DOI:10.1016/S0924-0136(03)00283-8**.

[11] Bertol, L.S., Kindlein Júnior, W., da Silva, F.P., Aumund-Kopp, C. (2010). Medical design: Direct metal laser sintering of Ti-6Al-4V. *Materials & Design*, vol. 31, no. 8, p. 3982-3988, **DOI:10.1016/j.matdes.2010.02.050**.

[12] Traini, T., Mangano, C., Sammons, R.L., Mangano, F., Macchi, A., Piattelli, A. (2008). Direct laser metal sintering as a new approach to fabrication of an isoelastic functionally graded material for manufacture of porous titanium dental implants. *Dental Materials*, vol. 24, no. 11, p. 1525-1533, **DOI:10.1016/j.dental.2008.03.029**.

[13] Mangano, F., Chambrone, L., van Noort, R., Miller, C., Hatton, P., Mangano, C. (2014). Direct metal laser sintering titanium dental implants: A review of the current literature. *International Journal of Biomaterials*, vol. 2014, art. ID 461534, p. 1-11, **DOI:10.1155/2014/461534**.

[14] Radzevich, S.P. (2012). *Dudley's Handbook of Practical Gear Design and Manufacture, 2nd Ed.*, CRC Press, Boca Raton, **DOI:10.1201/b11842**.

[15] Kruth, J-P., Mercelis, P., Van Vaerenbergh, J., Froyen, L., Rombouts, M. (2005). Binding mechanisms in selective laser sintering and selective laser melting. *Rapid Prototyping Journal*, vol. 11, no. 1, p. 26-36, **DOI:10.1108/13552540510573365**.

[16] EOS GmbH (2016). Electro Optical Systems from *http://www.eos.info/*, accessed on 2016-09-25.

[17] Dziubek, T., Pisula, J. (2013) Analysis of the accuracy of the 3D-CAD model of cylindrical gear obtained by the machining simulation for parametric surface models. *Mechanik*, no. 2, p. 1-12. (in Polish)

[18] Nelik, L. (1999). *Centrifugal and Rotary Pumps: Fundamentals with Applications*. CRC Press, Boca Raton, **DOI:10.1201/9781420049725**.

[19] Batsch, M., Pisula J., Przeszłowski, J., Bernaczek J. (2016). Tests and analyses of variants of a scraper with an integrated planetary gearing. Report No. 3 from studies carried out as part of project "*Development of an Innovative Type of a Scraper with an Integrated Planetary Drive for New or Modernized Sedimentation Tanks*" (POIR.01.01.01-00-0286/15-00).

[20] Bagci E., Yüncüoğlu E.U. (2017). The effects of milling strategies on forces, material removal rate, tool deflection, and surface errors for the rough machining of complex surfaces. *Strojniški vestnik - Journal of Mechanical Engineering*, vol. 63, no. 11, p. 643-656, **DOI:10.5545/sv-jme.2017.4450**.

[21] DIN 3962-1,2 (1978). *Tolerances for cylindrical gear teeth. Part 1: Tolerances for deviations of individual parameters. Part 2: Tolerances for tooth trace deviation*. Deutsches Institut für Normung, Frankfurt am Main.

[22] Oczos, K.E., Lubimov, V. (2003). *Geometrical surface structure product specifications. Basis of classification including an atlas of characteristic shaped surfaces*. Rzeszow University of Technology Publishing House, Rzeszow (in Polish).
[23] ISO/DIS 25178-2:2012. *Geometrical product specifications (GPS) – Surface texture: Areal – Part 2: Terms, definitions and surface texture parameters.* The International Organization for Standardization, Geneva.
[24] Atzeni, E., Salmi, A. (2012). Economics of additive manufacturing for end-usable metal parts. *The International Journal of Advanced Manufacturing Technology*, vol. 62, no. 9-12, p. 1147-1155, **DOI:10.1007/s00170-011-3878-1**.

Strojniški vestnik - Journal of Mechanical Engineering 65(2019)2, 87-102

DOI:10.5545/sv-jme.2018.5677

Original Scientific Paper

Received for review: 2018-07-25
Received revised form: 2018-12-12
Accepted for publication: 2019-01-14

Multi-Objective Optimization of the Dressing Parameters in Fine Cylindrical Grinding

Irina Stefanova Aleksandrova
Technical University of Gabrovo, Bulgaria

The optimum conditions for dressing grinding wheels determined and recommended in the literature are valid only for particular types and tools of dressing and grinding. In this paper, an attempt has been made to optimize the dressing process parameters in fine cylindrical grinding. To define the optimum values of the dressing process variables (radial feed rate of diamond roller dresser f_{rd}, dressing speed ratio q_d, dress-out time t_d, diamond roller dresser grit size/grinding wheel grit size ratio q_g, type of synthetic diamonds and direction of dressing), a multi-objective optimization has been performed based on a genetic algorithm. In the capacity of the optimization parameter, a generalized geometric-mean utility function has been chosen, which appears to be a complex indicator characterizing the roughness and accuracy of the ground surface, the grinding wheel lifetime and the manufacturing net costs of the grinding operation. The optimization problem has been solved in the following sequence: 1) a model of the generalized utility function has been created reflecting the complex effect of the dressing system parameters; 2) the optimum conditions of uni-directional and counter-directional dressing of aluminium oxide grinding wheels by experimental diamond roller dressers of synthetic diamonds of AC32 and AC80 types and different grit size at which the generalized utility function has a maximum have been determined; 3) a Pareto optimum solution has been found (f_{rd} = 0.2 mm/min; q_d = 0.8; t_d = 4.65 s; q_g = 2.56), which guarantees the best combination between the roughness and the deviation from cylindricity of the ground surface, the grinding wheel lifetime and the manufacturing net costs of the grinding operation.

Keywords: fine cylindrical grinding, dressing parameters, diamond roller dressers, multi-objective optimization

Highlights

- *A new multi-objective optimization approach based on a genetic algorithm and a generalized utility function to define the optimum values of the dressing system parameters in fine cylindrical grinding has been performed.*
- *Regression models for the response variables of the fine grinding process depending on the dressing system parameters have been built.*
- *Theoretical-experimental models have been created for determining the generalized utility function as a complex indicator characterizing the response variables of the fine grinding process.*
- *The optimum conditions of the uni-directional and counter-directional dressing of aluminium oxide grinding wheels by diamond roller dressers of synthetic diamonds of AC32 and AC80 types have been determined.*
- *A Pareto optimum solution has been found that guarantees the best combination between the roughness and the deviation from the cylindricity of the ground surface, the grinding wheel lifetime, and the manufacturing net costs.*

0 INTRODUCTION

The grinding process is characterized by a great number of response variables: economic (production rate, net costs), dynamic (cutting forces and power rate), and manufacturing (grinding wheel lifetime and cutting ability, roughness and accuracy of the machined surface). It has been found that these variables depend both on the cutting conditions during grinding and on the micro- and macro-geometry of the grinding wheel cutting surface formed during dressing [1] to [4].

The dressing process and its effect on the grinding response variables were studied in several publications. Cebalq [5] found that the different combinations between the dressing mode, dressing conditions, and the grinding wheel specification lead to different inter-grit spacing between the abrasive grits of the grinding-wheel cutting surface and, as a result, different response variables of the grinding process (equivalent grinding thickness, specific metal removal rate, roughness of the grinding-wheel cutting surface, roughness of the ground surface, etc.). Baseri et al. [6] and [7] and Baseri [8], Wegener et al. [9] and Palmer et al. [10] proved that the grinding-wheel topography and the conditions under which it is prepared have a profound influence upon the grinding performance, defined by the grinding forces, the power consumption, the cutting zone temperature, the radial wear of the wheel and also the surface finish of the workpiece. Chen et al. [11] found that a satisfied and stable grinding process can be controlled in real-time by means of utilizing the combination of optimal parameters, such as spindle speed, effective pack density, and the cutting space of abrasive grits. A similar conclusion is also drawn in the publications of other authors [12] to [15].

*Corr. Author's Address: Technical University of Gabrovo, 4 H. Dimitar St, Gabrovo, Bulgaria, irina@tugab.bg

Despite the significant influence of the dressing process on the response variables of the grinding process, its setup is often done based on the experience of the qualified staff or with the help of data handbooks [5], [8] and [16]. However, the dressing conditions selected by such practice are usually standard and they cannot satisfy certain economic criteria. Therefore, recently, some researchers [17] to [22] have applied, during cylindrical grinding, various techniques to optimize the grinding process parameters (grinding wheel speed, workpiece speed, depth of dressing, lead of dressing, contact area, grinding fluid, etc.) using a multi-objective function model with a weighted approach. The production costs, the production rate and the surface quality have been evaluated for the optimal grinding conditions, subject to constraints of thermal damage, wheel-wear parameters, and machine-tool stiffness. Amitay et al. [23] describes a technique for grinding and dressing optimization so that the maximum workpiece removal rate is ensured subject to constraints on workpiece burn and surface finish in an adaptive control grinding system. In his study, Baseri [8] used a feed-forward back-propagation neural network and a simulated annealing algorithm for the simultaneous minimization of the tangential cutting force and the surface roughness. During the experimental procedure, the grinding conditions were constant while the dressing conditions varied. The dressing parameters considered during the experiments were the dressing speed ratio, the dressing depth, and the dressing cross-feed. Klancnik et al. [24] presented a new and effective method of multi-criterion optimisation based on the evolutionary approach. This method can be introduced into the process of automatic programming of machine tools, including grinding machines. The analysis of the results provided by some authors in [8] and [17] to [22] shows that the optimization of the grinding process, depending on the dressing conditions, is a complicated non-linear optimization problem with constraints and multi-modal characteristics. The optimization problems have been solved under specific conditions of grinding and dressing. The defined optimum dressing parameters depend on the dressing method and dressing tool used. Further difficulties during optimization are associated with the fact that no comprehensive grinding models exist relating the dressing conditions to all response variables of the grinding process. At present, there is no comprehensive mathematical model that encompasses all aspects of grinding. In addition, the objective of optimization can vary depending on its application. All this shows that the optimization of the dressing conditions during cylindrical grinding should be performed considering the particular grinding and dressing conditions.

In a previous study [25], the results of multi-objective optimization of dressing grinding wheels made of aluminium oxide by using diamond roller dressers with medium- and high-strength synthetic diamonds of AC32 and AC80 types with different grit size during rough cylindrical grinding were presented. The generalized utility function was chosen in the capacity of the optimization parameter. The defined optimum dressing system parameters (dressing speed ratio, radial feed rate of the diamond roller dresser, dress-out time, diamond roller dresser grit size/grinding wheel grit size ratio, type of synthetic diamonds and direction of dressing) guarantee the maximum lifetime and maximum cutting ability coefficient of grinding wheels, the minimum tangential cutting force, and the maximum production rate of the grinding process. Taking into account the fact that grinding is widely used as a finishing process, it is necessary to define the dressing system parameters providing minimum roughness and maximum accuracy of the ground surfaces, together with maximum lifetime of the grinding wheel and minimum manufacturing net costs.

The objective of this paper is to determine the optimum dressing system parameters for grinding wheels made of aluminium oxide with experimental diamond roller dressers of medium- and high-strength synthetic diamonds of AC32 and AC80 types with different grit size during fine cylindrical grinding.

1 STUDY AND MODELLING OF FINE GRINDING RESPONSE VARIABLES

1.1 Equipment, Materials, and Methods

The task of this study is to find the correlations between the fine cylindrical grinding response variables and the parameters of uni-directional and counter-directional dressing of grinding wheels by employing diamond roller dressers, which have a layer of medium- and high-strength synthetic diamonds. The dressing speed ratio q_d, the radial feed rate f_{rd} [mm/min], the dress-out time t_d [s] and the ratio q_g between the grit sizes of the diamond roller dresser and grinding wheel are selected as control factors.

The experimental studies have been carried out on a KUF 250/500 cylindrical grinder (Fig. 1) under the following grinding conditions: grinding wheels: 1-350×125×22.5, 95A80K8V38, 95A60K8V38, 95A46K8V38, produced by the Abrasive Tools

Table 1. *Diamond grit properties [27] to [29]*

Grit size	Brand of synthetic diamonds			
	AC 32		AC80	
	Static compressive strength [N]	Arithmetic mean of the compressive strength for all grit sizes [N]	Static compressive strength [N]	Arithmetic mean of the compressive strength for all grit sizes [N]
D107 (100/80)	18.4	32	40	80
D251 (250/200)	23.5		78	
D426 (400/315)	49.6		109	

Factory – Berkovitsa, Bulgaria [26]; material to be machined – hardened steel 150Cr14 with hardness of 64 HRC in the shape of cylindrical workpieces with diameter d_w = 30 mm and length L_w = 150 mm; method of grinding – plunge grinding; cutting speed v_c = 30 m/s; cutting depth a_e = 0.1 mm; speed ratio q = 60; radial in-feed f_r = 0.01 mm/rev; coolant lubricant – sulfofresol (emulsion with 5 % concentration, which is fed through a free-falling jet through an open nozzle, the flow rate being approximately 1 m/s, and the consumption – approximately 9 l/min).

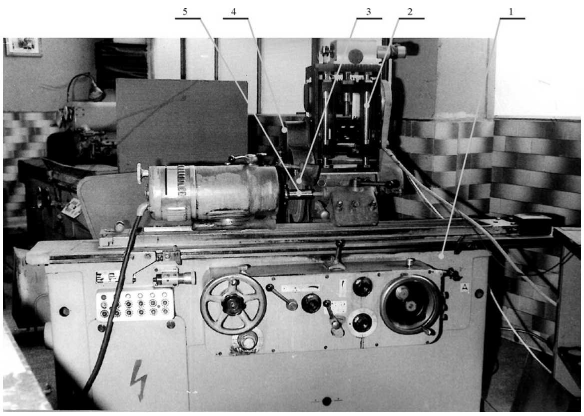

Fig. 1. *Experimental setup; 1. Cylindrical grinder KUF 250/500; 2. Special attachment; 3. Grinding wheel; 4. Diamond roller dresser; 5. Workpiece*

The grinding wheels are dressed using diamond roller dressers with a diameter of 92 mm produced by electroplating, with a layer of medium- and high-strength synthetic diamonds of AC32 and AC80 types by the Russian State Standard 9206-80 and the Ukrainian State Standard 3292-95 with grit sizes D426, D251 and D107 (Table 1) [27] to [29]. AC32 and AC80 are brands of synthetic diamond grinding powders of varying strength manufactured by the V. Bakul Institute for Superhard Materials.

The different grit sizes of the diamond roller dressers and grinding wheels provide values of the control factor q_g = 1.2 to 2.56.

In order to perform dressing with diamond roller dressers by using the plunge grinding method, a special attachment [30] has been designed. It is fixed on the grinding saddle of cylindrical grinder KUF 250/500. The control system of the attachment makes possible uni-directional and counter-directional dressing as well as variation of the control factors (radial feed rate f_{rd}, dressing speed ratio q_d and dress-out time t_d) within the following limits: f_{rd} = 0.2 mm/min to 1.4 mm/min, q_d = 0.2 to 0.8, t_d = 1 s to 9 s. These conditions guarantee the quality of the machined surfaces and the lifetime of the dressing tool and dressed tool [25], [30], and [31].

The studied response variables are: the roughness $Ra_{w,ih}$ [μm] and accuracy $\delta_{w,ih}$ [μm] of the ground surface, the grinding wheel lifetime $T_{s,ih}$ [min] and the manufacturing net costs of the grinding operation C_{ih} [€/pc] (ih is the combination of the code of the synthetic diamond brand and the type of dressing, see Table 2).

The ground surface roughness, evaluated by the arithmetic mean deviation of the profile, is measured with Mitutoyo SJ-201 profilometer. The accuracy of the ground surface shape is evaluated by the complex indicator: deviation from cylindricity, employing an apparatus for measuring deviation from roundness and cylindricity Roundtest RA-114/116 of the Mitutoyo company.

Table 2. *Code of the combination: brand of synthetic diamonds, dressing method'*

Dressing method, h	Brand of synthetic diamonds, i	
	AC32 (i = 1)	AC80 (i = 2)
Uni-directional (h = 1)	11	21
Counter-directional (h = 2)	12	22

The grinding wheel lifetime corresponds to the tool operation time between two dressing events. The criterion showing the necessity of dressing is the roughness occurring on the ground surface Ra_w = 2.5 μm.

The manufacturing net costs of the grinding operation is defined as the sum of labour costs and variable additional costs including grinding wheel dressing costs, grinding wheels costs, and electric power costs. The relative shares of the manufacturing net costs components depend on the manufacturing conditions and they are not identical. The electric power costs are very rarely significant (e.g., for intensive grinding), and the grinding wheel costs are high only when the tool price is high or during operation in self-grinding mode. Therefore, it could be assumed with sufficient accuracy that the manufacturing net costs of the grinding operation is defined by the relationship:

$$C_{ih} = C_{m,ih} + C_{d,ih}, \tag{1}$$

where the labour costs $C_{m,ih}$ and the dressing costs $C_{d,ih}$ are defined by the following formulae:

$$C_{m,ih} = C_m \cdot t_{m,ih}, \tag{2}$$

$$C_{d,ih} = \frac{C_m \cdot t_{d0} + S_s \cdot W_s + S_d / T_{d,ih}}{T_{s,ih}} \cdot t_{m,ih}, \tag{3}$$

where: C_m [€/min] is average labour costs; $t_{m,ih}$ [min] is grinding time: $t_{m,ih} = W_w / Q_{w,ih}$ (W_w [mm^3] is the volume of cut layer removed during grinding; W_w = const at constant cutting conditions during grinding; $Q_{w,ih}$ [mm^3/min] is the production rate of grinding process determined in [25]); t_{d0} [min] is dressing time: $t_{d0} = a_d / f_{rd} + t_d$ ($a_d = 0.03$ mm is a depth of dressing); S_s [€/mm^3] is the cost per unit volume of the grinding wheel; W_s [mm^3] is the volume of abrasive layer removed during dressing; S_d [€] is the price of diamond roller dressers; $T_{d,ih}$ is the diamond roller dresser lifetime evaluated by the number of working runs carried out up to reaching the permissible deviation of the grinding wheel profile after dressing $\delta_w = 0.02$ mm (they are counted by a mechanical counter comprised into the control system of the dressing attachment).

On the basis of preliminary experimental studies conducted [30], it is assumed that the general form of the model describing the relation between the chosen response variables of fine cylindrical grinding Y_j and the group of independent variables are the control factors f_{rd} (X_1), q_d (X_2), t_d (X_3) and q_g (X_4), is:

$$Y_j = E_j \cdot X_1^{b_{1j}} \cdot X_2^{b_{2j}} \cdot X_3^{b_{3j}} \cdot X_4^{b_{4j}}, \tag{4}$$

where $Y_1 = Ra_{w,ih}$; $Y_2 = \delta_{w,ih}$; $Y_3 = T_{s,ih}$; $Y_4 = C_{ih}$; b_{1j}, b_{2j}, b_{3j}, b_{4j} are exponents that determine the magnitude and the type of effect of control factors on the studied response variable Y_j of the grinding process; E_j is a coefficient accounting for the effect of the control factors (kinematic cutting parameters in grinding, physical-mechanical properties of the material to be machined, shape and size of the grinding wheel, type and quantity of the coolant lubricant, etc.).

In order to build the model in Eq. (4), it is linearized by a logarithmic transformation, as follows:

$$\ln Y_j = \ln E_j + b_{1j} \ln X_1 + b_{2j} \ln X_2 + b_{3j} \ln X_3 + b_{4j} \ln X_4. \tag{5}$$

Taking into account the interactions between the control factors, Eq. (5) can be written in this form:

$$Y_j' = b_{0,j} + \sum_{p=1}^{4} b_{p,j} A_p + \sum_{\substack{p=1 \\ p<t}}^{4} b_{pt,j} A_p A_t + \sum_{\substack{p=1 \\ p<t<l}}^{4} b_{ptl,j} A_p A_t A_l + b_{1234} A_1 A_2 A_3 A_4, \tag{6}$$

where $Y_j' = \ln Y_j$, $b_{0j} = \ln E_j$, $A_1 = \ln X_1 = \ln f_{rd}$, $A_2 = \ln X_2 = \ln q_d$, $A_3 = \ln X_3 = \ln t_d$, $A_4 = \ln X_4 = \ln q_g$.

Table 3. *Factor levels in the experimental design*

Factor levels	Coded x_p	Factors: Natural X_p $X_1=f_{rd}$ [mm/min]	$X_2=q_d$	$X_3=t_d$ [s]	$X_4=q_g$
lower x_{pl}, X_{pl}	-1	0.2	0.2	1	1.2
upper x_{pu}, X_{pu}	+1	1.4	0.8	9	2.56
basic x_{po}, X_{po}	0	0.5	0.4	3	1.75

$$x_p = \frac{2\left(\ln X_p - \ln X_{pu}\right)}{\ln X_{pu} - \ln X_{pl}} + 1, \quad X_{po} = 0.5\left(\ln X_{pu} + \ln X_{pl}\right)$$

To build model in Eq. (6), the first order design of experiment is applied, in particular a full factorial design of experiments is used. The minimum number for the levels of factor variation is two (Table 3), and the required number of runs is $N = 2^p = 2^4 = 16$ ($p = 4$ is the number of the control factors). The design of the experiments and the processing of the experimental results have been performed following the methodology presented in [32]. The models of grinding wheel lifetime $T_{s,ih}$, roughness $Ra_{w,ih}$ and accuracy $\delta_{w,ih}$ of the ground surface are synthesized according to actually measured values of the response variables in fine cylindrical grinding with grinding wheels dressed under certain conditions with diamond dresser rollers with a layer of synthetic diamonds of medium and high strength. The model of the manufacturing net costs C_{ih} is built on the basis of values calculated according to Eq. (1). The coefficient of multiple correlation R_j, the standard quadric mean deviation and the regression coefficients are determined by means of linear regression analysis. To check the significance of the regression coefficients, the model adequacy and the process description quality, the basic level (radial feed rate f_{rd}=0.5 mm/min; speed ratio q_d=0.4; dress-out time t_d=5 s; ratio between the grit sizes of the diamond roller dresser and the grinding wheel q_g=1.85, Table 3) has been selected as the most informative point, where four observations have been performed (n=4).

1.2 Experimental Results and Modelling

The designs of the experiments with the values of the response variables of the fine cylindrical grinding process are presented in Tables 4 and 5.

After statistical analysis of the experimental results and transformation of the independent variables from coded to natural type (Table 3), theoretical-experimental models of roughness and accuracy of the ground surface, grinding wheel lifetime and the manufacturing net costs have been built and their general form is the following:

$$Y_j = E_{j,ih} \cdot f_{rd}^{b_{1j,ih}} \cdot q_d^{b_{2j,ih}} \cdot t_d^{b_{3j,ih}} \cdot q_g^{b_{4j,ih}}, \qquad (7)$$

The determined values of the constants $E_{j,ih}$ and exponents $b_{1,ih}$, $b_{2,ih}$, $b_{3,ih}$, $b_{4,ih}$ in the regression models in Eq. (7) are given in Table 6. The values of the standard deviation for each of the experiments carried out, characterizing the repeatability of the experimental results and used for determining the empirical values of the Fisher criterion $\widehat{F}_{j,ih}$ and the multiple correlation coefficient $\widehat{R}_{j,ih}$, are $S^2_{Rj,ih}$ = 0.0004 to 0.0045. They have been determined on the basis of the four observations performed for each of the response variables of the fine grinding process at a combination of the main levels of the control factors (f_{rd}=0.5 mm/min; q_d=0.4; t_d=5 s; q_g=1.85), Tables 4 and 5. The constructed models are adequate, which is proved by comparing the empirical $\widehat{F}_{j,ih}$ and tabular $F^t_{j,ih}$ values of the Fisher criterion ($\widehat{F}_{j,ih} < F^t_{j,ih}$, Table 6). They describe with high accuracy the dependencies between the response variables and the control factors (the values of the coefficient of multiple correlation are $\widehat{R}_{j,ih}$ = 0.981 to 0.998).

Table 4. *Design of the experiment and response variables of the grinding process (in dressing with diamond roller dressers of synthetic diamonds AC32)*

Control factors				Response variables of the grinding process							
				Uni-directional dressing				Counter-directional dressing			
f_{rd} [mm/min]	q_d	t_d [s]	q_g	Ra_{w11} [μm]	δ_{w11} [μm]	T_{s11} [min]	C_{11} [€/pc]	Ra_{w12} [μm]	δ_{w12} [μm]	T_{s12} [min]	C_{12} [€/pc]
0.2	0.2	1	1.2	0.86	5.64	17.02	0.031	0.69	5.64	18.60	0.035
1.4	0.2	1	1.2	1.03	9.94	28.03	0.027	0.87	9.94	27.94	0.029
0.2	0.8	1	1.2	1.01	6.06	23.60	0.028	0.56	6.06	9.80	0.050
1.4	0.8	1	1.2	1.22	10.52	29.20	0.025	0.70	10.52	16.90	0.041
0.2	0.2	9	1.2	0.67	4.14	13.97	0.037	0.58	4.14	11.30	0.052
1.4	0.2	9	1.2	0.81	7.28	22.25	0.033	0.73	7.28	20.10	0.036
0.2	0.8	9	1.2	0.79	3.54	19.30	0.036	0.47	3.54	8.20	0.056
1.4	0.8	9	1.2	0.95	6.15	23.84	0.032	0.59	6.15	12.90	0.051
0.2	0.2	1	2.56	0.41	8.42	38.80	0.022	0.34	8.42	42.20	0.022
1.4	0.2	1	2.56	0.47	11.39	56.20	0.019	0.41	11.39	68.00	0.019
0.2	0.8	1	2.56	0.45	9.72	46.30	0.019	0.25	9.72	22.60	0.036
1.4	0.8	1	2.56	0.58	12.2	65.00	0.017	0.30	12.2	35.70	0.023
0.2	0.2	9	2.56	0.29	6.17	28.80	0.034	0.26	6.17	26.70	0.039
1.4	0.2	9	2.56	0,32	8.34	43.70	0.029	0,31	8.34	39.10	0.028
0.2	0.8	9	2.56	0.34	5.68	36.10	0.030	0.20	5.68	20.90	0.047
1.4	0.8	9	2.56	0.41	7.13	46.00	0.026	0.23	7.13	30.40	0.034
0.5	0.4	3	1.85	0.62	7.33	33.5	0.026	0.41	7.33	26.9	0.035
0.5	0.4	3	1.85	0.6	7.4	33.4	0.024	0.4	7.4	26.8	0.033
0.5	0.4	3	1.85	0.58	6.8	32.5	0.025	0.45	6.8	25.6	0.0324
0.5	0.4	3	1.85	0.55	7.25	32.1	0.0248	0.47	7.25	24.7	0.0342

Table 5. *Design of the experiment and response variables of the grinding process (in dressing with diamond roller dressers of synthetic diamonds AC80)*

Control factors				Response variables of the grinding process							
				Uni-directional dressing				Counter-directional dressing			
f_{rd} [mm/min]	q_d	t_d [s]	q_g	Ra_{w21} [μm]	δ_{w21} [μm]	T_{s21} [min]	C_{21} [€/pc]	Ra_{w22} [μm]	δ_{w22} [μm]	T_{s22} [min]	C_{22} [€/pc]
0.2	0.2	1	1.2	1.21	5.64	24.06	0.031	1.08	5.64	23.70	0.035
1.4	0.2	1	1.2	1.44	9.94	25.70	0.027	1.28	9.94	25.10	0.029
0.2	0.8	1	1.2	1.31	6.06	26.80	0.029	0.95	6.06	11.80	0.050
1.4	0.8	1	1.2	1.54	10.52	31.50	0.026	1.13	10.52	16.20	0.041
0.2	0.2	9	1.2	0.88	4.14	16.50	0.039	0.73	4.14	10.80	0.052
1.4	0.2	9	1.2	1.05	7.28	20.00	0.033	0.86	7.28	17.80	0.037
0.2	0.8	9	1.2	0.97	3.54	20.30	0.037	0.64	3.54	8.30	0.055
1.4	0.8	9	1.2	1.12	6.15	22.90	0.033	0.76	6.15	12.80	0.051
0.2	0.2	1	2.56	0.64	8.42	58.00	0.022	0.62	8.42	52.50	0.022
1.4	0.2	1	2.56	0.72	11.39	67.00	0.019	0.68	11.39	75.00	0.019
0.2	0.8	1	2.56	0.68	9.72	63.00	0.019	0.56	9.72	36.40	0.035
1.4	0.8	1	2.56	0.77	12.2	78.00	0.017	0.61	12.2	50.00	0.022
0.2	0.2	9	2.56	0.36	6.17	29.10	0.034	0.35	6.17	26.90	0.039
1.4	0.2	9	2.56	0,48	8.34	39.30	0.029	0.46	8.34	35.90	0.028
0.2	0.8	9	2.56	0.46	5.68	34.70	0.030	0.30	5.68	29.10	0.046
1.4	0.8	9	2.56	0.55	7.13	57.00	0.027	0.37	7.13	33.30	0.034
0.5	0.4	3	1.85	0.89	7.33	41.7	0.026	0.7	7.33	26.4	0.035
0.5	0.4	3	1.85	0.8	7.4	40.1	0.024	0.68	7.4	29.3	0.033
0.5	0.4	3	1.85	0.81	6.8	38.8	0.025	0.65	6.8	29.5	0.032
0.5	0.4	3	1.85	0.85	7.25	38	0.0245	0.6	7.25	26.5	0.034

Table 6. *Values of constants and exponents in the theoretical-experimental models, Eq. (7)*

Response variables	Constants	Exponents				Fisher criterion	
Y_j	$E_{j,ih}$	$b_{1j,ih}$	$b_{2j,ih}$	$b_{3j,ih}$	$b_{4j,ih}$	$\widehat{F}_{j,ih}$	$F^t_{j,ih}$
Ra_{w11}	1.503	0.091	0.123	–0.133	–1.077	0.613	8.765
Ra_{w12}	0.787	0.103	–0.183	–0.099	–1.084	0.442	8.765
Ra_{w21}	1.909	0.088	0.074	–0.169	–0.959	1.292	8.765
Ra_{w22}	1.285	0.086	–0.098	–0.209	–0.853	0.650	8.765
δ_{w11} δ_{w12} δ_{w21} δ_{w22}	9.541	0.324–0.199A_4	0.082–0.199A_3	–0.261	0.255	0.535	8.785
T_{s11}	23.810	0.068–0.117A_2+0.083A_4	0.052+0.058A_4+0.091A_1A_4	–0.087–0.041A_4	1.029	2.695	8.845
T_{s12}	11.296	0.236	–0.435+0.095A_3	–0.057	1.091	2.827	8.875
T_{s21}	25.376	0.017+0.031A_3+0.104A_4	0.130	–0.095–0.136A_4	1.254	3.764	8.845
T_{s22}	10.833	0.155	–0.472+0.108A_3+0.229A_4	–0.114	1.524	2.530	8.812
C_{11}	0.029	–0.068	–0.055	0.080+0.130A_4	–0.509	1.343	8.785
C_{12}	0.049	–0.120+0.017A_2+ +0.047A_3–0.121A_4	0.264–0.017A_3–0.084A_4 +0.052A_1A_3–0.132A_1A_4	–0.071+0.104A_4	–0.675	1.506	8.887
C_{21}	0.027	–0.067	–0.066	0.076+0.130A_4	–0.484	1.028	8.785
C_{22}	0.048	–0.116+0.017A_2+ +0.048A_3–0.122A_4	0.248–0.014A_3–0.085A_4 +0.053A_1A_3–0.133A_1A_4	0.076+0.109A_4	–0.693	1.531	8.887

$A_1 = \ln f_{rd};\ A_2 = \ln q_d;\ A_3 = \ln t_d;\ A_4 = \ln q_g$

1.3 Analysis of the Experimental Results

The analysis of the theoretical-experimental models in Eq. (7) and the graphics plotted on the basis of them (Fig. 2) allows the following conclusions to be drawn:

(1) The studied response variables of the fine grinding process greatly depend on the diamond roller dresser grit size/the grinding wheel grit size ratio.

(1.1) When q_g increases within the studied range (2.1 times), the grinding wheel lifetime increases (by 1.8 to 3 times). The impact of q_g depends on the types of synthetic diamonds in the working layer of the diamond roller dressers, the conditions and direction of dressing, and it is most strongly marked in counter-directional dressing with diamond roller dressers with a working layer of synthetic diamonds AC80.

(1.2) The roughness of the ground surface decreases (by 1.9 to 2.3 times) when q_g increases. The impact of q_g is more strongly marked in counter-directional dressing with diamond roller dressers of synthetic diamonds AC32. The decrease in the ground surface roughness with an increase in q_g is related to an improvement of the grinding wheel cutting ability, as well as to a decrease in forces and temperature load in the cutting zone in grinding.

(1.3) The manufacturing net costs of the grinding operation decrease (by 1.1 to 1.7 times) with an increase in the grit ratio q_g. The impact of q_g is the greatest in counter-directional dressing with diamond roller dressers with a working layer of synthetic diamonds AC80 and it increases when dress-out time t_d decreases.

(1.4) When the grit ratio q_g increases, the ground surface accuracy decreases (deviation from cylindricity rises by 1.15 to 1.55 times), and the impact is identical in uni-directional and counter-directional dressing with diamond roller dressers of medium- and high-strength synthetic diamonds AC32 and AC80. The impact of q_g decreases with an increase in radial feed rate. The relatively small impact of q_g on the ground surface accuracy is determined by the impact of this factor, different in character and rate, on the grinding wheel macro-geometry and on the normal cutting force in grinding, and by their key role for the ground surface accuracy, established in [30].

(2) The direction of dressing has different influence on the response variables of the fine grinding process.

(2.1) The uni-directional dressing ensures longer lifetime of the grinding wheels (up to 2.5 times) compared to counter-directional dressing. The difference in the lifetimes of the grinding wheels dressed uni-directionally and counter-directionally grows with an increase in radial feed rate f_{rd} and in dressing speed ratio q_d, and with a decrease in the grit ratio q_g. This tendency is valid for dressing with diamond roller dressers with a working layer of synthetic diamonds AC32 and AC80 and it is related to the greater "roughness" of the cutting surface of the grinding wheels after their uni-directional dressing [30], [33] and [34] as well as with the destruction of the wheel structure as an additional consideration [35] and [36].

(2.2) The roughness of the machined surface after grinding with grinding wheels dressed counter-directionally is smaller (up to 1.9 times) compared to the roughness after grinding with grinding wheels dressed uni-directionally. This tendency can be explained by the lower "roughness" of the cutting surface of the grinding wheels dressed counter-directionally [30], [33] and [34] and it is more strongly marked in dressing with diamond roller dressers of synthetic diamonds AC32.

(2.3) The accuracy of the ground surface does not depend on the direction of dressing and the type of synthetic diamonds in the working layer of the diamond roller dressers. This is related to the fact that the grinding wheel macro-geometry affects directly the ground surface accuracy, as the experimentally measured values of radial run-out of grinding wheels of different specifications after uni-directional and counter-directional dressing with diamond roller dressers with a working layer of medium- and high-strength synthetic diamonds AC32 and AC80 differ by not more than 5 % [30].

(2.4) The manufacturing net costs of grinding with grinding wheels dressed uni-directionally are lower (up to 1.8 times) than the costs in grinding with tools dressed counter-directionally. The difference in manufacturing net costs values rises with an increase in speed ratio q_d and with a decrease in grit ratio q_g and it does not depend on the type of synthetic diamonds in the working layer of the diamond roller dressers.

(3) The dressing conditions have an effect different in character and rate on the response variables in the fine grinding process, which depends on the method of dressing and the type of synthetic diamonds in the working layer of the diamond roller dressers.

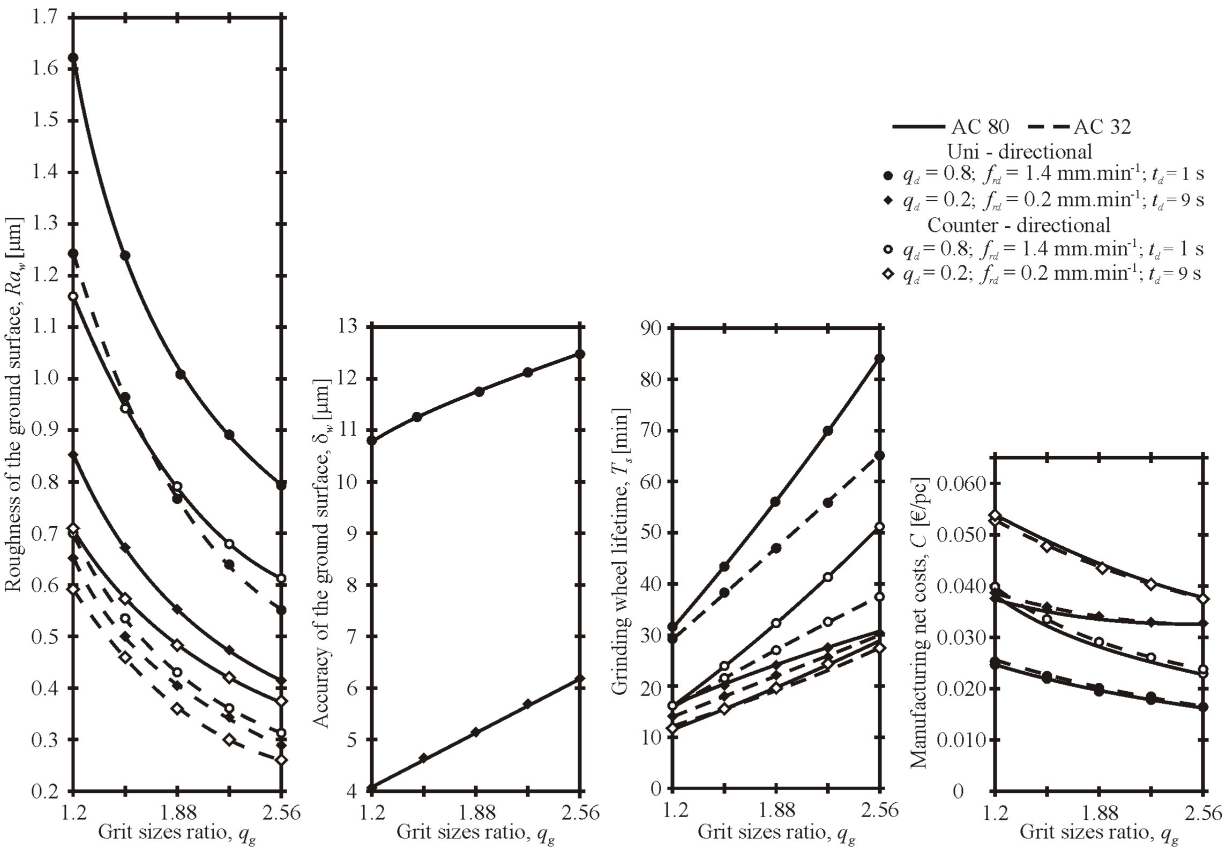

Fig. 2. *Impact of the dressing system parameters on: a) roughness of the ground surface, b) accuracy of the ground surface, c) grinding wheel lifetime, and d) manufacturing net costs of grinding operation*

(3.1.) The increase in radial feed rate in dressing leads to a respective increase in the grinding wheels lifetime (up to 1.6 times) and in the ground surface roughness (up to 1.3 times) and to a decrease in the manufacturing net costs (up to 1.5 times). The influence of f_{rd} is most strongly marked in counter-directional dressing with diamond roller dressers with a working layer of synthetic diamonds AC32.

With an increase in radial feed rate in dressing the ground surface accuracy decreases (by 30 % to 74 %) depending on the grit ratio q_g. The impact of f_{rd} rises with a decrease in q_g. This character of change is explained by an increase in the area of the removed abrasive layer, as well as an increase in the forces and heat which results in quality deterioration of the grinding wheel profiled surface and in a decrease in ground surface accuracy, respectively **[10]** and **[30]**.

(3.2) The speed ratio impact in dressing on the grinding wheel lifetime is most strongly pronounced in counter-directional dressing with diamond roller dressers with a working layer of synthetic diamonds AC32, as a decrease in q_d leads to a respective increase in the grinding wheel lifetime (up to 83 %). The tendency has an opposite character in uni-directional dressing of grinding wheels.

The speed ratio q_d has a different impact on the roughness of the ground surface and the manufacturing net costs of the grinding operation depending on the method of dressing. In uni-directional dressing, when q_d increases, the ground surface roughness increases, and the manufacturing net costs decrease. In counter-directional dressing, the increase in q_d leads to a respective decrease in roughness and an increase in manufacturing net costs. The speed ratio impact is most strongly marked in counter-directional dressing with diamond roller dressers of synthetic diamonds AC32, and in the studied variation range of q_d the decrease in roughness is up to 23 %, and the increase in manufacturing net costs is up to 67 %.

Of all dressing conditions the speed ratio q_d has the least influence on the ground surface accuracy. When q_d increases, the deviation from cylindricity increases or decreases (up to 12 %) depending on the dress-out time t_d.

(3.3) With a decrease in dress-out time t_d the grinding wheels lifetime rises (up to 88 %). The impact of t_d is most strongly marked in counter-directional dressing with diamond roller dressers of synthetic diamonds AC80.

Of all dressing conditions the dress-out time has the greatest effect on the roughness of the ground surface and the manufacturing net costs of the grinding operation, which is related to the mechanisms in the generation of grinding wheel topography by dressing and the occurrence of structure damage from dressing **[35]** and **[36]**. With an increase in t_d within the studied range roughness decreases (up to 37 %), and the manufacturing net costs increase (up to 57 %). The tendency is valid for uni-directional and counter-directional dressing of grinding wheels with diamond roller dressers of medium- and high-strength synthetic diamonds. The influence of t_d on the roughness of the ground surface is the strongest in counter-directional dressing with diamond roller dressers of synthetic diamonds AC80. The variation rate of manufacturing net costs depending on the dress-out time is most strongly pronounced in uni-directional dressing with diamond roller dressers of synthetic diamonds AC80 and rises with an increase in the grit ratio q_g.

With an increase in the dress-out time t_d the accuracy of the machined surface improves (the deviation from cylindricity decreases by 1.36 to 1.71 times). The impact of t_d rises with an increase in the speed ratio q_d.

2 OPTIMIZATION OF THE DRESSING SYSTEM PARAMETERS IN FINE CYLINDRICAL GRINDING

2.1 A Method for Optimization

Each of the studied response variables of the fine grinding process is of certain importance but it is not sufficient for the optimum process control. The optimum values of the various response variables will be obtained by different combinations of values of the control factors (dressing conditions, type, and specification of the dressing tool), provided the cutting conditions in grinding are constant and have been assumed in the capacity of constant factors. Therefore, optimization by one response variable is not advisable. The multi-objective optimization offers a larger amount of information in order to make a well-founded decision about choosing optimum dressing system parameters. Various algorithms for carrying out optimization exist which differ in type and number of response variables as well as in the method of finding the optimum solution **[37]** to **[39]**. The existing approaches to the multi-objective optimization can be classified into three main categories **[40]** to **[43]**. The first group comprises approaches which employ the most important response variable as an objective function, and the remaining response variables are considered constraints. The major disadvantage of these approaches is that they do not implement the principal idea of multi-objective optimization, namely: all response variables to be considered simultaneously. The proposed procedures of this category would generally result in unrealistic solutions, especially when conflicting objectives are presented. In addition, the selection of one of the response variables as an objective function may not be easy in many cases. When applying the methods of the second group a region of interest is formed in which the various response variables meet certain requirements. This approach works well when there is a small number of control factors (2 or 3) and response variables (up to three). The third group consists of approaches that combine the multiple response variables into a single generalized objective function, and the multi-objective optimization problem is solved as a single-objective one. The most popular of these approaches are defined as: utility function, desirability function, loss function, distance function, and proportion of conformance.

To determine the optimum dressing system parameters in fine cylindrical grinding, the method of generalized utility function has been chosen. It is one of the most frequently used in industry methods for multi-objective optimization **[42]** to **[44]**. It is based on the idea that the quality of a product or a process that has multiple response variables is completely unacceptable if one of the response variables lies beyond the utility limits. This method determines the result as a combination of response variables and selects a set of factors for which the result is the maximum. The utility function is a scale-invariant index that enables response variables of different units of measurement to be compared. With this method, the researcher can easily determine the optimum parameters in the group of solutions. The generalized utility function has a lot of advantages over other combining methods mainly due to its flexibility, since it allows some of the response variables to be maximized and, at the same time, others to be minimized.

The generalized utility function is a complex indicator characterizing the response variables of fine grinding (roughness $Ra_{w,ih}$ and accuracy $\delta_{w,ih}$ of the ground surface, grinding wheel lifetime $T_{s,ih}$ and manufacturing net costs of the grinding operation C_{ih}). It can be defined as geometric mean $\Phi_{G,ih}$ or arithmetic mean $\Phi_{A,ih}$ value of the utility coefficients $\eta_{j,ih}$, obtained by transforming the response variables of the fine grinding process into dimensionless quantities [32] and [40]. To solve the specific optimization problem the geometric-mean generalized utility function $\Phi_{G,ih}$ has been chosen in the capacity of optimizing parameter, since if one of the response variables of the fine grinding process does not meet the requirements for utility limits, $\Phi_{G,ih} = 0$. In this case, the arithmetic-mean generalized utility function $\Phi_{A,ih} \neq 0$, and it can have a maximum value, but the dressing conditions, under which this value of $\Phi_{A,ih}$ has been obtained, are not optimal.

The solution to the optimization problem is reduced to determining a combination between the type of dressing (uni-directional or counter-directional), the dressing conditions (radial feed rate f_{rd}, dressing speed ratio q_d, dress-out time t_d), and the specifications of the diamond roller dresser and the grinding wheel (type of synthetic diamonds and grit sizes ratio q_g), for which the geometric-mean generalized utility function has a maximum.

2.2 Modelling of the Generalized Utility Function

In order to solve the optimization problem, mathematical models have been built for defining the geometric-mean generalized utility function depending on the control factors of the dressing process. The general form of the models, based on the performed analysis of the impact of the dressing system parameters on the response variables of the fine grinding process, is:

$$\Phi_{G,ih} = D_{0,ih} + \sum_{p=1}^{4} D_{p,ih} X_p + \sum_{p=1}^{4} D_{pp,ih} X_p^2 + \sum_{\substack{p=1 \\ p<t}}^{4} D_{pt,ih} X_p X_t + \sum_{\substack{p=1 \\ p<t<l}}^{4} D_{ptl,ih} X_p X_t X_l + D_{1234,ih} X_1 X_2 X_3 X_4. \quad (8)$$

The models, Eq. (8), under the conditions of uni-directional and counter-directional dressing with diamond roller dressers of medium- and high-strength synthetic diamonds AC32 and AC80 have been created on the basis of the results from the conducted experiments following an optimum plan with the number of experiments $N = 2^p + 2p + 1 = 2^4 + 2\cdot 4 + 1 = 25$ ($p = 4$ is the number of control factors), Table 7.

In each experiment, the generalized utility function is determined as geometric-mean $\Phi_{G,ih}$ value of the particular utility functions $\eta_{j,ih}$ according to the relationship [32] and [40]:

$$\Phi_{G,ih} = \sqrt[4]{\prod_{j=1}^{4} \eta_{j,ih}} = \sqrt[4]{\prod_{j=1}^{4} \frac{k_j \left(Y_{j,ih} - Y_{ju}\right)}{\Delta Y_j}}, \quad (9)$$

where $j = 1$ to 4 is the number of response variables of the fine grinding process; k_j is the utility coefficient; $k_j = +1$, when the increase in the response variable Y_j is useful; $k_j = -1$, when the decrease in Y_j is useful; Y_{ju} is the most useless result of the response variable Y_j, obtained within the limits of the permissible space; $\Delta Y_j = Y_{j\max} - Y_{j\min}$; $Y_{j\max}$ and $Y_{j\min}$ are utility limits (maximum and minimum values of the response variable Y_j).

The values of the most useless result and of the utility limits of the response variables of fine grinding are determined according to the equalities:

$Ra_{w_u} = \left(Ra_{w,ih}\right)_{\max}$; $\delta_{w_u} = \left(\delta_{w,ih}\right)_{\max}$; $T_{s_u} = \left(T_{s,ih}\right)_{\min}$; $C_u = \left(C_{ih}\right)_{\max}$; $\Delta Ra_w = \left(Ra_{w,ih}\right)_{\max} - \left(Ra_{w,ih}\right)_{\min}$; $\Delta\delta_w = \left(\delta_{w,ih}\right)_{\max} - \left(\delta_{w,ih}\right)_{\min}$; $\Delta T_s = \left(T_{s,ih}\right)_{\max} - \left(T_{s,ih}\right)_{\min}$; $\Delta C_s = \left(C_{ih}\right)_{\max} - \left(C_{ih}\right)_{\min}$; where $\left(Ra_{w,ih}\right)_{\min}$, $\left(Ra_{w,ih}\right)_{\max}$, $\left(T_{s,ih}\right)_{\min}$, $\left(T_{s,ih}\right)_{\max}$, $\left(C_{ih}\right)_{\min}$, $\left(C_{ih}\right)_{\max}$ are respectively the minimum and maximum values of the studied response variables of the fine grinding process (roughness, accuracy, grinding wheel lifetime and manufacturing net costs of the grinding operation), determined by the regression models, Eq. (7).

On the basis of the determined values of the generalized utility function (Table 7), applying the regression analysis method and the software product QstatLab [45], the models in Eq. (8) of the generalized utility function have been built.

The coefficients $D_{0,ih}$, $D_{p,ih}$, $D_{pp,ih}$, $D_{pt,ih}$, $D_{ptl,ih}$, and $D_{1234,ih}$ in the regression equations, Eq. (8), for $\Phi_{G,ih}$, the calculated $\widehat{F}_{ih}$ and tabular $F_{ih}^t = F_{ih(\alpha, v1, v2)}$ values of the Fisher criterion ($\alpha = 0.05$ is the significance level; $v_1 = k - 1$ and $v_2 = N - k$ are degrees of freedom; k is the number of coefficients in the model), as well as the values of the determination coefficient $\widehat{R}_{ih}^2$ are presented in Table 8. The regression models are adequate since the condition $\widehat{F}_{ih} > F_{ih}^t$ has been met

Table 7. *Design of the experiment and generalized utility function during uni-directional and counter-directional dressing with diamond roller dressers with a working layer of synthetic diamonds AC32 and AC80*

Control factors				Generalized utility function			
				Uni-directional dressing		Counter-directional dressing	
				Diamond roller dressers AC32	Diamond roller dressers AC80	Diamond roller dressers AC32	Diamond roller dressers AC80
f_{rd} [mm/min]	q_d	t_d [s]	q_g	Φ_{G11}	Φ_{G21}	Φ_{G12}	Φ_{G22}
0.2	0.2	1	1.2	0.437	0.460	0.442	0.431
1.4	0.2	1	1.2	0.422	0.351	0.448	0.390
0.2	0.8	1	1.2	0.482	0.464	0.217	0.221
1.4	0.8	1	1.2	0.359	0.304	0.278	0.294
0.2	0.2	9	1.2	0.388	0.223	0.222	0.215
1.4	0.2	9	1.2	0.457	0.418	0.421	0.372
0.2	0.8	9	1.2	0.471	0.000	0.000	0.094
1.4	0.8	9	1.2	0.479	0.465	0.276	0.252
0.2	0.2	1	2.56	0.614	0.514	0.644	0.657
1.4	0.2	1	2.56	0.532	0.542	0.566	0.544
0.2	0.8	1	2.56	0.617	0.656	0.431	0.492
1.4	0.8	1	2.56	0.000	0.000	0.000	0.000
0.2	0.2	9	2.56	0.573	0.571	0.536	0.534
1.4	0.2	9	2.56	0.613	0.602	0.624	0.583
0.2	0.8	9	2.56	0.648	0.638	0.426	0.487
1.4	0.8	9	2.56	0.680	0.678	0.559	0.573
0.2	0.5	5	1.88	0.577	0.583	0.399	0.430
1.4	0.5	5	1.88	0.583	0.572	0.496	0.484
0.8	0.2	5	1.88	0.578	0.549	0.550	0.524
0.8	0.8	5	1.88	0.600	0.600	0.438	0.454
0.8	0.5	1	1.88	0.509	0.521	0.454	0.456
0.8	0.5	9	1.88	0.587	0.576	0.462	0.464
0.8	0.5	5	1.2	0.474	0.450	0.335	0.310
0.8	0.5	5	2.56	0.651	0.655	0.561	0.581
0.8	0.5	5	1.88	0.590	0.583	0.483	0.481

with a confidence level of 95 %. To determine the effect of the control factors on the generalized utility function, analysis of variance (ANOVA) has been conducted.

It has been found that of all studied factors the influence of the grit ratio is the strongest and with an increase in q_g the function $\Phi_{G,ih}$ increases. The impact of q_g depends upon the type of synthetic diamonds in the working layer of the diamond roller dressers, the direction and the conditions of dressing. It is most strongly pronounced in uni-directional dressing with diamond roller dressers with synthetic diamonds AC80 and grows with an increase in the speed ratio q_d and the dress-out time t_d and a decrease in the radial feed rate f_{rd} (Figs. 3 and 4).

The dressing conditions have an impact different in character and rate on the geometric-mean generalized utility function, which depends on the type of synthetic diamonds in the working layer of the diamond roller dressers and the dressing method (Figs. 3 and 4). The greatest impact is with the speed ratio in uni-directional dressing with diamond roller dressers of synthetic diamonds AC80; with an increase in q_d, the generalized utility function decreases.

2.3 Determination of Optimum Dressing System Parameters

The optimization task has been solved during uni-directional and counter-directional dressing of grinding wheels of aluminium oxide with diamond roller dressers with working layer of medium- and high-strength synthetic diamonds AC32 and AC80 by applying genetic algorithm [46] and using the software product QStatLab [45].

The determined optimum dressing system parameters (type of dressing, radial feed rate of diamond roller dresser f_{rd}, dressing speed ratio q_d,

Table 8. *Regression coefficients and statistical analysis of regression models, Eq. (8)*

Regression coefficients	Generalized utility function $\Phi_{G,ih}$			
	Φ_{G11}	Φ_{G21}	Φ_{G12}	Φ_{G22}
$D_{0,ih}$	–0.110	0.182	–0.582	–0.222
$D_{1,ih}$	+0.060	-	-	-
$D_{2,ih}$	+0.146	-	+0.287	-
$D_{3,ih}$	+0.029	-	-	-
$D_{4,ih}$	+0.514	+0.190	+1.142	+0.641
$D_{11,ih}$	-	-	-	-
$D_{22,ih}$	-	–0.297	-	–0.231
$D_{33,ih}$	–0.004	–0.004	-	–0.002
$D_{44,ih}$	–0.097	-	-0.271	–0.109
$D_{12,ih}$	+0.245	+0.501	-	+0.565
$D_{13,ih}$	-	+0.034	-	-
$D_{23,ih}$	-	-	–0.159	-
$D_{34,ih}$	-	+0.010	-	-
$D_{123,ih}$	–0.031	–0.062	+0.091	–0.046
$D_{124,ih}$	–0.398	–0.394	–0.286	–0.440
$D_{134,ih}$	-	–0.012	-	-
$D_{234,ih}$	-	-	–0.286	-
$D_{1234,ih}$	+0.044	+0.053	-	+0.049
Determination coefficient $\hat{R}^2_{ih}$	0.973	0.965	0.918	0.953
Fisher criterion $\hat{F}_{ih}$	50.740	38.981	27.367	40.344
Fisher criterion F'_{ih}	2.602	2.602	2.614	2.591

dress-out time t_d, diamond roller dresser grit size/grinding wheel grit size ratio q_g and type of synthetic diamonds), whereat the generalized utility function $\Phi_{G,ih}$ has a maximum, are presented in Table 9. Under the predicted optimum dressing system parameters, confirmation run experiments have been performed, in which the roughness and accuracy of the ground surface, the grinding wheel lifetime and the manufacturing net costs of the grinding operation have been determined. A comparison between the experimental and the predicted according to the models, Eq. (7), values of the grinding process response variables (see Table 10) has been made. The results show that the error percentage is within the permissible limits (≤5 %), and it is as follows: 0.65 % to 5 % for the roughness of the ground surface; 1.24 % to 4.65 % for the accuracy of the ground surface; 1.83 % to 3.91 % for the grinding wheel lifetime; 0.37 % to 5 % for the manufacturing net costs of the grinding operation. These results prove that the recommended dressing system parameters are optimum and correct.

The analysis of the obtained results shows that during uni-directional and counter-directional dressing with diamond roller dressers of synthetic diamonds AC32 and AC80 the maximum values of the generalized utility function are obtained for different combinations of speed ratio q_d, radial feed

Table 9. *Optimum dressing system parameters*

Synthetic diamonds	Dressing method	Dressing conditions: Radial feed rate f_{rd} [mm/min]	Dressing conditions: Dressing speed ratio q_d	Dressing conditions: Dress-out time t_d [s]	Grit sizes ratio q_g	Generalized utility function $\Phi_{G,ih}$
AC32	Uni-directional	0.2	0.8	5.7	2.53	0.6984
	Counter-directional	0.2	0.2	3.5	2.56	0.6873
AC80	Uni-directional	1.4	0.8	9	2.21	0.7534
	Counter-directional	0.2	0.2	1	2.56	0.6736

Table 10. *Comparison of experimental and predicted values of the grinding process response variables*

Optimum dressing system parameters						Roughness of the ground surface Ra_w [μm]		Accuracy of the ground surface δ_w [μm]		Grinding wheel lifetime T_s [min]		Net costs of grinding operation C [€/pc]	
Synthetic diamonds	Dressing method	f_{rd} [mm/min]	q_d	t_d [s]	q_g	EV	PV	EV	PV	EV	PV	EV	PV
AC32	Uni-directional	0.2	0.8	5.7	2.53	0.38	0.369	6.81	6.507	39.6	38.05	0.03	0.0289
	Counter-directional	0.2	0.2	3.5	2.56	0.3	0.285	9.35	9.182	34.7	33.36	0.024	0.0229
AC80	Counter-directional	1.4	0.8	9	2.21	0.62	0.624	7.2	7.535	44.0	45.15	0.027	0.0271
	Uni-directional	0.2	0.2	1	2.56	0.61	0.588	8.42	8.524	52.5	53.46	0.022	0.0209

EV – experimental value; PV – predicted value

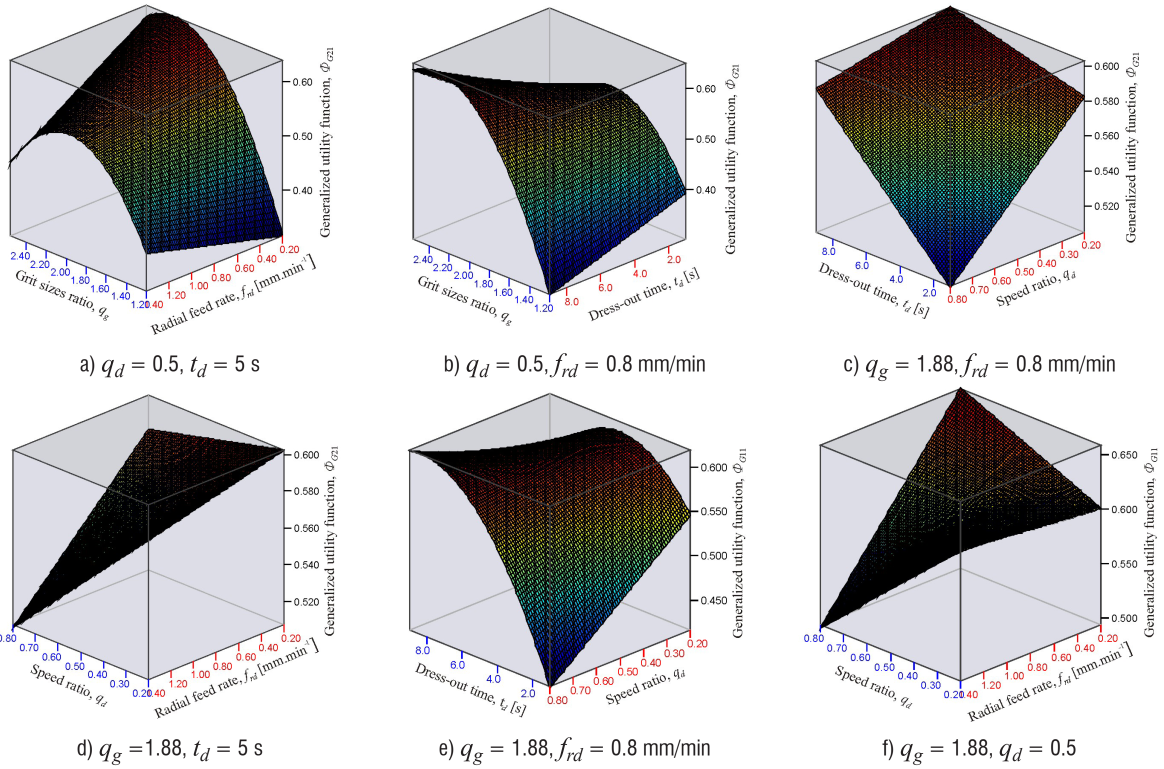

a) q_d = 0.5, t_d = 5 s b) q_d = 0.5, f_{rd} = 0.8 mm/min c) q_g = 1.88, f_{rd} = 0.8 mm/min

d) q_g =1.88, t_d = 5 s e) q_g = 1.88, f_{rd} = 0.8 mm/min f) q_g = 1.88, q_d = 0.5

Fig. 3. *Generalized utility function during uni-directional dressing with a, b, c, d) diamond roller dressers AC80, and e, f) AC32*

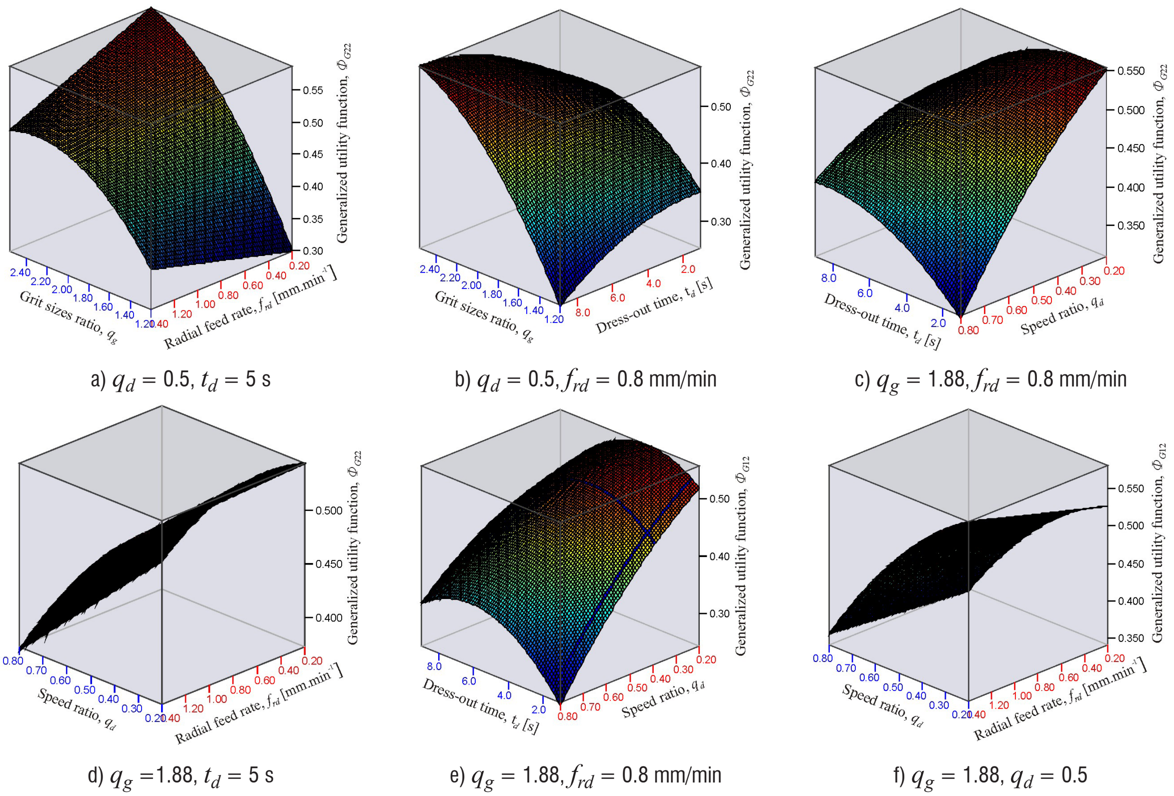

a) q_d = 0.5, t_d = 5 s b) q_d = 0.5, f_{rd} = 0.8 mm/min c) q_g = 1.88, f_{rd} = 0.8 mm/min

d) q_g =1.88, t_d = 5 s e) q_g = 1.88, f_{rd} = 0.8 mm/min f) q_g = 1.88, q_d = 0.5

Fig. 4. *Generalized utility function during counter-directional dressing with a, b, c, d) diamond roller dressers AC80, and e, f) AC32*

rate f_{rd}, dressing time t_d and grit sizes ratio q_g. With regard to this, by applying genetic algorithm and employing the software product QStatLab Pareto-optimum solutions to the four objective functions: Φ_{G11}, Φ_{G12}, Φ_{G21}, Φ_{G22}, are found, whose maximums are at different points of the studied factor space. From the found Pareto-front the following combination has been chosen as an optimum solution: $f_{rd} = 0.2$ mm/min, $q_d = 0.75$, $t_d = 4.65$ s, $q_g = 2.56$. It combines in an optimum way the largest values of the objective functions, as follows: $\Phi_{G11} = 0.6907$, $\Phi_{G12} = 0.5077$, $\Phi_{G21} = 6507$, $\Phi_{G22} = 0.5073$. The determined optimum dressing system parameters provide the best combination between the roughness and accuracy of the machined surface, the grinding wheel lifetime and the manufacturing net costs of the grinding operation, as follows:

- in uni-directional dressing with diamond roller dressers of synthetic diamonds AC32: $Ra_{w11} = 0.37$ μm, $\delta_{w11} = 4.3$ μm, $T_{s11} = 39.03$ min, $C_{11} = 0.028$ €/pc;
- in counter-directional dressing with diamond roller dressers of synthetic diamonds AC32: $Ra_{w12} = 0.22$ μm, $\delta_{w12} = 6.9$ μm, $T_{s12} = 21.45$ min, $C_{12} = 0.04$ €/pc;
- in uni-directional dressing with diamond roller dressers of synthetic diamonds AC80: $Ra_{w21} = 0.51$ μm, $\delta_{w21} = 6.9$ μm, $T_{s21} = 34.21$ min, $C_{21} = 0.027$ €/pc;
- in counter-directional dressing with diamond roller dressers of synthetic diamonds AC80: $Ra_{w22} = 0.37$ μm, $\delta_{w22} = 6.9$ μm, $T_{s22} = 30.47$ min, $C_{22} = 0.04$ €/pc.

3 CONCLUSIONS

As a result of the conducted experimental studies, modelling and multi-objective optimization of dressing grinding wheels of aluminium oxide with diamond roller dressers of medium- and high-strength synthetic diamonds AC32 and AC80 in fine cylindrical grinding, the following results have been achieved:

(1) Adequate regression models for the response variables of the fine grinding process (roughness and accuracy of the ground surface, grinding wheel lifetime, and manufacturing net costs) depending on the dressing system parameters (radial feed rate of diamond roller dresser, dressing speed ratio, dress-out time, diamond roller dresser grit size/grinding wheel grit size ratio, type of synthetic diamonds and direction of dressing).

(2) Theoretical-experimental models have been created for determining the generalized utility function as a complex indicator characterizing the response variables of the fine grinding process. The models have been constructed for uni-directional and counter-directional dressing with diamond roller dressers of synthetic diamonds AC32 and AC80, and they reflect the complex impact of the dressing system parameters.

(3) With the method of the generalized utility function, the optimum dressing system parameters of uni-directional and counter-directional dressing with diamond roller dressers of synthetic diamonds AC32 and AC80 have been determined (Table 9). On the basis of the obtained results, it can be recommended to perform dressing of grinding wheels in fine cylindrical grinding under the conditions at which the maximum value of the generalized utility function is obtained, namely: uni-directional dressing with diamond roller dressers with working layer of high-strength synthetic diamonds AC80; diamond roller dresser grit size/grinding wheel grit size ratio $q_g = 2.21$; radial feed rate of diamond roller dresser $f_{rd} = 1.4$ mm/min; dressing speed ratio $q_d = 0.8$; dress-out time $t_d = 9$ s. The grinding wheels dressing under these conditions ensures: roughness of the ground surface 0.62 μm, accuracy of the ground surface shape 7.2 μm, grinding wheel lifetime 44 min and manufacturing net costs of the grinding operation 0.027 €/pc (Table 10).

(4) With the Pareto method and by applying a genetic algorithm, the optimum dressing system parameters have been determined, valid for uni-directional and counter-directional dressing with diamond roller dressers of synthetic diamonds AC32 and AC80, as follows: radial feed rate of diamond roller dresser $f_{rd} = 0.2$ mm/min; dressing speed ratio $q_d = 0.75$; dress-out time $t_d = 4.65$ s and diamond roller dresser grit size/grinding wheel grit size ratio $q_g = 2.56$. The credibility of the determined optimum parameters has been proven by an experimental study of the response variables of the fine grinding process. It has been found that they guarantee the best combination between the roughness ($Ra_w \leq 0.51$ μm) and the accuracy ($\delta_w \leq 6.9$ μm) of the ground surface, the grinding wheel lifetime ($T_s \geq 21.45$ min) and the manufacturing net costs of the grinding operation ($C_{21} \leq 0.04$ €/pc). The results obtained provide possibilities for control and optimization of the fine grinding process by selecting optimum

dressing system parameters and they can be used in all machine-building companies.

4 ACKNOWLEDGEMENTS

This work was supported by the Bulgarian Ministry of Education and Science and the Technical University of Gabrovo under contract No 1713M.

5 REFERENCES

[1] Maksoud, T.M.A., Atia, M.R. (2004). Review of intelligent grinding and dressing operations. *Machining Science and Technology*, vol. 8, no. 2, p. 263-276, **DOI:10.1081/MST-200028748**.

[2] Malkin, S. (2008). *Grinding Technology: Theory and Application of Machining with Abrasives*. Industrial Press, New York.

[3] Puerto, P., Fernández, R., Madariaga, J., Arana, J., Gallego, I. (2013). Evolution of surface roughness in grinding and its relationship with the dressing parameters and the radial wear. *Procedia Engineering*, vol. 63, p. 174-182, **DOI:10.1016/j.proeng.2013.08.181**.

[4] Ostaševičius, V., Jūrėnas, V., Vilkauskas, A., Balevičius, G., Senkus, A., Jotautienė, E. (2017). A novel excitation approach to ultrasonically-assisted cylindrical grinding. *Strojniški vestnik – Journal of Mechanical Engineering*, vol. 63, no. 12, p. 696-704, **DOI:10.5545/sv-jme.2016.4196**.

[5] Cebalq, R. (1988). Optimization of the creep-feed grinding process. *International Journal of Production Research*, vol. 26, no. 10, p. 1665-1670, **DOI:10.1080/00207548808947980**.

[6] Baseri, H., Rezaei, S.M., Rahimi, A., Saadat, M. (2008). Analysis of the disc dressing effects on grinding performance - part 1: Simulation of the disc dressed wheel surface. *Machining Science and Technology*, vol. 12, no. 2, p. 183-196, **DOI:10.1080/10910340802067395**.

[7] Baseri, H., Rezaei, S.M., Rahimi, A., Saadat, M. (2008). Analysis of the disc dressing effects on grinding performance – part 2: Effects of the wheel topographical parameters on the specific energy and workpiece surface roughness. *Machining Science and Technology*, vol. 12, no. 2, p. 197-213, **DOI:10.1080/10910340802067429**.

[8] Baseri, H. (2012). Simulated annealing based optimization of dressing conditions for increasing the grinding performance. *International Journal of Advanced Manufacturing Technology*, vol. 59, no. 5-8, p. 531-538, **DOI:10.1007/s00170-011-3518-9**.

[9] Wegener, K, Hoffmeister, H.-W., Karpuschewski, B., Kuster, F., Hahmann, W.-C., Rabiey, M. (2011) Conditioning and monitoring of grinding wheels. *CIRP Annals*, vol. 60, no. 2, p. 757-777, **DOI:10.1016/j.cirp.2011.05.003**.

[10] Palmer, J., Ghadbeigi, H., Novovic, D., Curtis, D. (2018). An experimental study of the effects of dressing parameters on the topography of grinding wheels during roller dressing. *Journal of Manufacturing Processes*, vol. 31, p. 348-355, **DOI:10.1016/j.jmapro.2017.11.025**.

[11] Chen, Y., Chen, X., Xu, X., Yu, G. (2018). Effect of energy consumption in the contact zone on machining condition optimization in precision surface grinding. *Strojniški vestnik - Journal of Mechanical Engineering*, vol. 64, no. 4, p. 233-244, **DOI:10.5545/sv-jme.2017.4995**.

[12] Jiang, J.L., Ge, P.Q., Bi, W.B., Zhang, L., Wang, D.X., Zhang, Y. (2013). 2D/3D ground surface topography modeling considering dressing and wear effects in grinding process. *International Journal of Machine Tools and Manufacture*, vol. 74, p. 29-40, **DOI:10.1016/j.ijmachtools.2013.07.002**.

[13] Saad, A., Bauer, R., Warkentin, A. (2010). Investigation of single-point dressing overlap ratio and diamond-roll dressing interference angle on surface roughness in grinding. *Transactions of the Canadian Society for Mechanical Engineering*, vol. 34, no. 2, p. 295-308, **DOI:10.1139/tcsme-2010-0018**.

[14] Lefebvre, A., Sinot, O., Torrance, A. (2013). Optimization of dressing conditions for a resin-bonded diamond wheel by topography analysis. *Machining Science and Technology*, vol. 17, no. 2, p. 312–324, **DOI:10.1080/10910344.2013.781364**.

[15] Zylka, L., Burek, J., Mazur, D. (2017). Diagnostic of peripheral longitudinal grinding by using acoustic emission signal. *Advances in Production Engineering & Management*, vol. 12, no. 3, p. 221-232, **DOI:10.14743/apem2017.3.253**.

[16] Linke, B. (2008). Dressing process model for vitrified bonded grinding wheels. *CIRP Annals*, vol. 57, no. 1, p. 345-348, **DOI:10.1016/j.cirp.2008.03.083**.

[17] Lee, K.-M., Hsu, M.-R., Chou, J.-H., Guo, C.-Y. (2011). Improved differential evolution approach for optimization of surface grinding process. *Expert Systems with Applications*, vol. 38, no. 5, p. 5680-5686, **DOI:10.1016/j.eswa.2010.10.067**.

[18] Slowik, A., Slowik, J. (2008). Multi-objective optimization of surface grinding process with the use of evolutionary algorithm with remembered Pareto set. *International Journal of Advanced Manufacturing Technology*, vol. 37, no. 7-8, p. 657-669, **DOI:10.1007/s00170-007-1013-0**.

[19] Saravanan, R., Sachithanandam, M. (2001). Genetic algorithm (GA) for multivariable surface grinding process optimisation using a multi-objective function model. *International Journal of Advanced Manufacturing Technology*, vol. 17, no. 5, p. 330-338, **DOI:10.1007/s001700170167**.

[20] Zhang, G., Liu, M., Li, J., Ming, W.Y., Shao, X.Y., Huang, Y. (2014). Multi-objective optimization for surface grinding process using a hybrid particle swarm optimization algorithm. *International Journal of Advanced Manufacturing Technology*, vol. 71, no. 9-12, p. 1861-1872, **DOI:10.1007/s00170-013-5571-z**.

[21] Krishna, A., Rao, K. (2006). Multi-objective optimization of surface grinding operations using scatter search approach. *International Journal of Advanced Manufacturing Technology*, vol. 29, no. 5-6, p. 475-480, **DOI:10.1007/BF02729099**.

[22] Baskar, N., Saravanan, R., Asokan, P., Prabhaharan, G. (2004). Ants colony algorithm approach for multi-objective optimisation of surface grinding operations. *International Journal of Advanced Manufacturing Technology*, vol. 23, no. 5-6, p. 311-317, **DOI:10.1007/s00170-002-1533-6**.

[23] Amitay, G., Malkin, S., Koren, Y. (1981). Adaptive control optimization of grinding. *Journal of Engineering for Industry*, vol. 103, no. 1, p. 103-108, **DOI:10.1115/1.3184449**.

[24] Klancnik, S., Brezocnik, M., Balic, J. (2016). Intelligent CAD/CAM system for programming of CNC machine tools. *International Journal of Simulation Modelling*, vol. 15, no. 1, p. 109-120, **DOI:10.2507/IJSIMM15(1)9.330**.
[25] Aleksandrova, I. (2016). Optimization of the dressing parameters in cylindrical grinding based on a generalized utility function. *Chinese Journal of Mechanical Engineering*, vol. 29, no. 1, p. 63-73, **DOI:10.3901/CJME.2015.1103.130**.
[26] Catalogue of the Abrasive Tools Factory – Berkovitsa (2018). from *https://0501.nccdn.net/4_ 2/000/000/084/3b1/ZAI-2018.pdf*, accessed on 2018-10-30.
[27] GOST 9206-80 (1980). *Diamond powders. Technical Conditions.* USSR State Committee for Standard. Moscow. (in Russian)
[28] DSTU 3292-95 (1995). *Synthetic Diamond Powders. General Technical Conditions*. State Standard of Ucraine, Kiev. (in Russian)
[29] Industrial Diamond Association of America, Inc. A Review of Diamond Sizing and Standards, from *http://www.nationalresearchcompany.com/wp-content/uploads/2015/05/Diamond_Sizing_and_Standards.pdf*, accessed on 2018-12-07.
[30] Aleksandrova, I. (1995). *Optimization of Dressing Process of Abrasive Tools with Diamond Profiling Rollers*. PhD thesis, Technical University of Gabrovo, Gabrovo. (in Bulgarian)
[31] Aleksandrova, I. (2010). Methodology of modeling, identification and control of grinding process. *Inzhenerni nauki*, no. 1, p. 60-72. (in Bulgarian)
[32] Aleksandrov, A., Aleksandrova, I. (2012). *Theory of Experiment*. Express, Gabrovo. (in Bulgarian)
[33] Schmitt, R. (1968) *Abrichten von Schleifscheiben mit diamantbestückten Rollen.* PhD thesis, TU Braunschweig. (in German)
[34] Daneshi, A., Jandaghi, N., Tawakoli, T. (2014). Effect of dressing on internal cylindrical grinding. *Procedia CIRP*, vol. 14, p. 37-41, **DOI:10.1016/j.procir.2014.03.064**.
[35] Klocke, F., Linke, B. (2008). Mechanisms in the generation of grinding wheel topography by dressing. *Production Engineering*, vol. 2, no 2, p. 157-163, **DOI:10.1007/s11740-008-0101-9**.
[36] Klocke, F., Thiermann, J., Mattfeld, P. (2015). Influence of the dressing process on grinding wheel wear. *Production Engineering*, vol. 9, no 5-6, p. 563-568, **DOI:10.1007/s11740-015-0606-y**.
[37] Vishnupad, P., Shin, Y.C. (1998). Intelligent optimization of grinding processes using fuzzy logic. *Proceedings of the Institution of Mechanical Engineers, Part B: Journal of Engineering Manufacture*, vol. 212, no. 8, p. 647-660, **DOI:10.1243/0954405981515914**.
[38] Mukherjee, I., Ray, P.K. (2006). A review of optimization techniques in metal cutting processes. *Computers & Industrial Engineering*, vol. 50, no. 1-2, p. 15-34, **DOI:10.1016/j.cie.2005.10.001**.
[39] Yusup, N., Zain, A.M., Hashim, S.Z.M. (2012). Evolutionary techniques in optimizing machining parameters: Review and recent applications (2007–2011). *Expert Systems with Applications*, vol. 39, no. 10, p. 9909-9927, **DOI:10.1016/j.eswa.2012.02.109**.
[40] Stoyanov, S. (1993). *Optimization of Manufacturing Processes.* Tehnika, Sofia. (in Bulgarian)
[41] Mukherjee, I., Ray, P.K. (2008). Optimal process design of two-stage multiple responses grinding processes using desirability functions and metaheuristic technique. *Applied Soft Computing*, vol. 8, no. 1, p. 402-421, **DOI:10.1016/j.asoc.2007.02.005**.
[42] Dzebo, S., Morehouse, J.B., Melkote, S.N. (2012). A methodology for economic optimization of process parameters in centerless grinding. *Machining Science and Technology*, vol. 16, no. 3, p. 355-379, **DOI:10.1080/10910344.2012.698958**.
[43] Salmasnia, A., Kazemzadeh, R.B., Niaki, S.T.A. (2012). An approach to optimize correlated multiple responses using principal component analysis and desirability function. *International Journal of Advanced Manufacturing Technology*, vol. 62, no. 5-8, p. 835-846, **DOI:10.1007/s00170-011-3824-2**.
[44] Raissi, S., Farsani, R. (2009). Statistical process optimization through multi-response surface methodology. *International Scholarly and Scientific Research & Innovation*, vol. 3, no. 3, p. 247-251.
[45] Vuchkov, I.N., Vuchkov, I.I. (2009). *Statistical Methods of Quality Control, Robust Engineering, Planning, Modeling and Optimization*, QStatLab, v 5.3. (in Bulgarian)
[46] Goldberg, D. (1989). *Genetic Algorithms in Search, Optimization and Machine Learning*. Addison Wesley Longman, London.

Strojniški vestnik - Journal of Mechanical Engineering 65(2019)2, 103-112

DOI:10.5545/sv-jme.2018.5823
Original Scientific Paper
Received for review: 2018-10-29
Received revised form: 2019-01-14
Accepted for publication: 2019-01-21

Numerical and Experimental Study of a Novel Valve Using the Return Stream Energy to Adjust the Speed of a Hydraulic Actuator

Grzegorz Filo[1,*] – Edward Lisowski[1] – Dominik Kwiatkowski[1] – Janusz Rajda[2]
[1] Cracow University of Technology, Poland
[2] PONAR Wadowice, Poland

This article discusses the possibility of increasing the speed of movement of a single-sided hydraulic cylinder piston rod using a fluid stream from the return line. Directing the return stream back to the supply line instead of the fluid reservoir causes significant increase in the inflow rate to the actuator. This situation may arise when the piston rod of the cylinder is not fully loaded on part of the movement range. As part of this work, we proposed a solution in the form of a novel control valve, consisting of a throttle valve and a differential valve controlled by the pressure difference between the supply line and the return line. A geometric model was created using SolidWorks, then a simulation model was made in Matlab/Simulink. Next, simulations were carried out to prove that the use of the return fluid stream gives a possibility of a significant increase in the piston rod speed. The results of the numerical analyses were verified on a test bench where the valve prototype was tested. Speed characteristics of the piston rod against both payload force and throttle valve setting were determined. High convergence with the simulation results was obtained. It has also been confirmed that the proposed solution can be advantageous in practical applications.
Keywords: hydraulic system modelling, return stream energy usage, novel control valve design, hydraulic actuator speed adjustment

Highlights
- *Adjusting the speed of a hydraulic actuator piston rod movement depending on the payload.*
- *Using the energy of a return fluid stream to re-supply a hydraulic actuator.*
- *Modelling, carrying out simulations in Matlab/Simulink, and conducting experiments on a test bench.*
- *Obtaining a wide range of hydraulic actuator speed changes and achieving a high level of convergence of simulation results and experimental tests.*

0 INTRODUCTION

Hydraulic cylinders are commonly used as actuators in drive systems. Their main advantage is the ability to operate with large forces, while having small dimensions and relatively simple installation. Both fixed and variable capacity pumps can be used to supply hydraulic cylinders. In general, variable capacity pumps provide better power management and speed control, but they are more expensive and require dedicated electronic controllers. In the case of constant-capacity pumps, the actuator speed can be controlled hydraulically, using the system of control valves. Usually, flow regulators or throttle valves are used for this purpose.

The adjustment of a hydraulic actuator speed that depends on the payload value allows the working time to be shortened as well as the efficiency of the fluid stream energy conversion to mechanical energy to be improved. This subject has been undertaken in numerous scientific publications, and several different ways to solve it can be found. One group of solutions is based on the use of a variable displacement pump and proportional control valves with sensors, transducers, and a digital controller. A two-level idle speed control system with a hydraulic accumulator for an excavator was proposed by Lin et al. [1] to reduce energy consumption and improve the control performance of the actuator when the idle speed control is switched off. Experimental results showed high energy efficiency and excellent control performance of the automatic switching system between the first idle speed, the second idle speed, and the normal operating speed of a hydraulic cylinder. Pérez et al. [2] presented a robust controller for the hydraulic actuator force control, while Wang et al. [3] proposed a novel position-pressure master-slave controller for the hydraulic servo system. Moreover, Wang and Wang [4] developed an energy-saving control strategy with a load-sensing structure including a load-sensing pump, a proportional relief valve, a throttle valve, and an adaptive control algorithm.

The second group includes solutions based on the appropriate configuration of hydraulic control valves, without the use of advanced digital controllers. Liu et al. [5] showed a direct proportional flow control system with a load pressure compensation feature on a load control valve. The proposed solution provides

*Corr. Author's Address: Cracow University of Technology, Faculty of Mechanical Engineering, Jana Pawla II 37, 31-864 Cracow, Poland, filo@mech.pk.edu.pl

a flow through the control valve to be proportional to the pilot pressure in the control stroke and thus decides the overrunning load lowering speed control performance of the whole system. A novel method of design for hydraulic robotic lifting equipment was designed by Adeoye et al. [6]. The method involves the use of a flow control valve and a pressure relief valve for stroke speed adjustment of a lifting device with a hydraulic cylinder. Another design example of a pilot-assisted load control valve for proportional flow control based on dynamics modelling was presented by Xie et al. [7]. The flow through the designed valve is proportionally controlled by pilot pressure. The static and dynamic flow control performance of the valve has been validated by the tests made in a mobile crane lifting and lowering system. Similarly, Man et al. [8] proposed an energy regeneration system with the accumulator that can reduce the energy consumption of hydraulic impulse testing equipment by 15 %.

This article discusses the possibility of increasing the speed of movement of a single-sided hydraulic cylinder using a fluid stream from the return line. Usually, a fluid stream in the return line is not used, since it goes straight to the reservoir. On the other side, directing the return stream to the supply line instead of the fluid reservoir causes a significant increase in the inflow rate to the actuator. This situation may arise only when the piston rod of the cylinder is not fully loaded on the part of its movement range. However, it occurs quite often in practice, e.g., in the hydraulic system of a press for garbage compression, an extruder, a cutter, a squeezer, etc. The use of the return fluid stream gives a possibility of an increase in a piston rod speed of movement even by several times, depending on the hydraulic cylinder geometry (ratio of cylinder and rod diameters) as well as the range of the movement in which the cylinder is not fully loaded. According to the presented literature analysis, such a system requires the use of appropriate control, which may be electronic or hydraulic. In general, hydraulic control is less expensive and easier to apply, since it does not require transducers or microprocessor chips; however, it is less accurate. Hence, a solution in the form of a novel control valve has been proposed. The valve consists of a throttle valve and a differential valve controlled by the pressure difference between the supply line and the return line. Simulations were carried out to prove that the use of the return fluid stream gives the possibility of even a threefold increase in the piston rod speed of movement. The results of the numerical analyses were then verified on a test bench where the valve prototype was tested. Speed characteristics of the piston rod as a function of both payload and throttle valve setting were obtained, achieving a high level of convergence with the simulation results. It has also been confirmed that the proposed solution is accurate enough and can be an advantageous option in practical applications.

1 WORKING PRINCIPLE OF ANALYSED VALVE

A flow control valve UZFD6 shown in Fig. 1 is the subject of the analysis. The valve consists of a monolithic block inside of which flow paths have been hollowed out. Also, a differential valve (3) and two throttle check valves (1), (2) have been placed in the block.

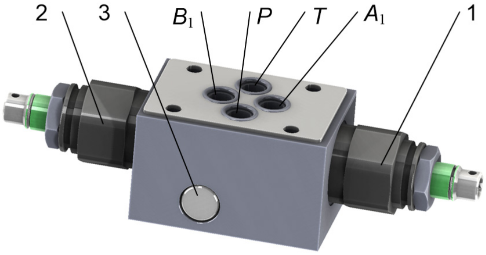

Fig. 1. *Flow control valve UZFD6: (1) throttle valve on the supply side s, (2) throttle valve on the load side t, (3) differential valve; A_1, B_1 connection channels; P supply port; T return port*

The valve is adapted for a direct connection to the electrically controlled *WE*6-type control valve. For this purpose, appropriate P, T, A_1, B_1 connection channels have been made on both sides of the valve body. A cross-section through the differential valve is presented in Fig. 2. As seen in the figure, a one-stage poppet valve has been applied. Flow through the valve occurs when the hydrostatic force coming from the p_t pressure exceeds the sum of the hydrostatic force coming from the p_s pressure and the initial F_{s3} spring tension.

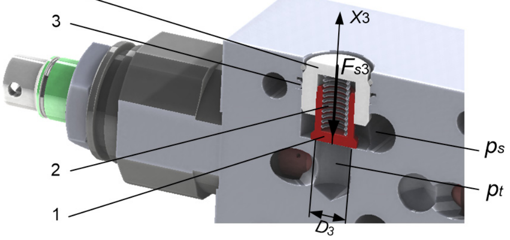

Fig. 2. Sectional view of the differential valve: (1) poppet, (2) spring, (3) sealing, (4) cover; x_3 axis of poppet movement

The throttle valve located on the supply side was not included in the model or the research. It was set in an open position during all laboratory tests. In contrast, the throttle valve located on the load side played an important role in obtaining the characteristics. A sectional view of this valve is shown in Fig. 3.

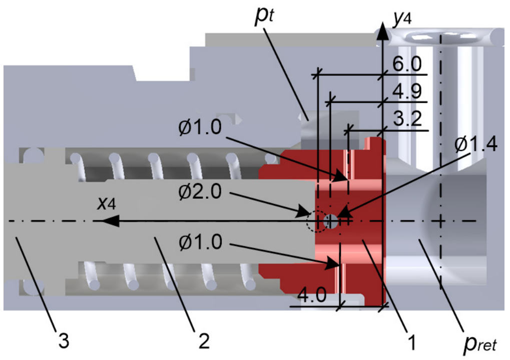

Fig. 3. *Sectional view of a throttle valve located on the load side: (1) sleeve, (2) pin, (3) knob; p_t, p_{ret} pressures; x_4 axis of pin movement*

A throttling gap is formed by four holes of various diameters drilled in the collar of the sleeve (1). A pin (2) can move inside the sleeve, gradually revealing the holes. The position of the pin, and thus the throttling gap area, can be set by the operator using a knob (3). The A_4 gap area has been calculated as a function of the x_4 pin position with regard to the diameters and positions of the holes. A graph of the obtained function is shown in Fig. 4.

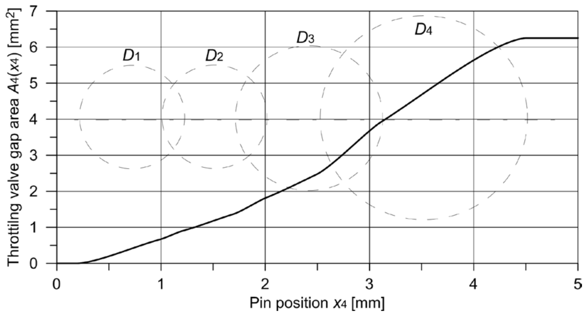

Fig. 4. *Throttling gap area against the pin position*

2 MODEL OF THE SYSTEM

In the first stage, a mathematical model of the system was formulated using equations of movable element motion, flow equations through gaps, balances in the separated volumes and geometric relationships. Next, a simulation model was built by introducing the obtained equations to the Matlab-Simulink system.

2.1 Formulating a Mathematical Model

A mathematical model of the system was built according to a numerical modelling methodology, which was first proposed by Watton and Nelson [9], and then used by Naseradinmousavi and Nataraj [10] and Casoli et al. [11] among others. It comprises equations of motion, flow balances of isolated volumes, flow equations through throttle gaps and orifices, and geometrical equations. A schematic of the modelled system is shown in Fig. 5. The model takes into account the case of supplying the hydraulic actuator on the side without the piston rod. Thus, the rod slides out from the cylinder. Without the flow through the differential valve ($Q_3 = 0$), theoretical speed can be easily calculated from Eq. (1). Moreover, in this case, the speed in the opposite direction is higher, since the active cylinder area is reduced by the rod area.

$$v_{cyl} = \frac{4 \cdot Q_1}{\pi \cdot D_{cyl1}^2}, \text{where } Q_1 = Q_p - Q_5. \qquad (1)$$

In a system with a differential valve, which directs the return stream from the actuator back to the supply line, it is possible to significantly vary the speed of the piston rod, using the same fixed-speed pump. The obtained speed of the rod may be lower, equal to or higher than the return movement speed. However, the calculation of the piston speed is now far more complex, since the flow rate $Q_1 = Q_p - Q_5 + Q_3$, where Q_3 depends on the payload and the throttle valve settings. The next paragraphs present the process of a mathematical model formulating.

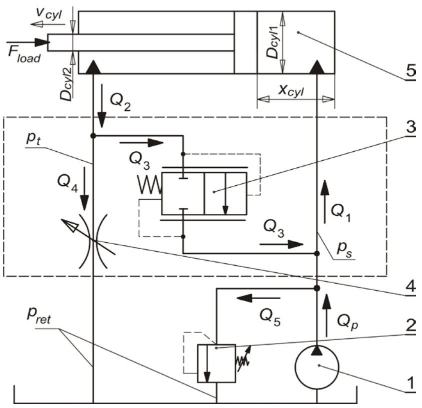

Fig. 5. Schematic of the modelled hydraulic system: (1) pump, (2) relief valve, (3) differential valve, (4) throttle valve, (5) hydraulic cylinder; p_s, p_t, p_{ret} pressures; Q_p, Q_1, ..., Q_5 flow rates, F_{load} payload of the actuator

The input function is a Q_p volumetric flow rate generated by the pump. The flow rate value is assumed to be constant except the t_{start} start-up time, when it increases linearly.

$$Q_p = \begin{cases} Q_{p\_nom} \cdot \dfrac{t}{t_{start}}, \ if\ t < t_{start} \\ Q_{p\_nom}, \qquad \text{otherwise.} \end{cases} \quad (2)$$

The flow balance of the supply line is used to calculate the supply pressure:

$$\frac{dp_s}{dt} = \frac{\beta}{V_s + A_{cyl1} \cdot x_{cyl}} \cdot \left(Q_p - Q_1 + Q_3 - Q_5\right). \quad (3)$$

Similarly, for the load line the following equation is valid:

$$\frac{dp_t}{dt} = \frac{\beta}{V_t - \left(A_{cyl1} - A_{cyl2}\right) \cdot x_{cyl}} \cdot \left(Q_2 - Q_3 - Q_4\right). \quad (4)$$

The Q_1 and Q_2 flow rates are determined using the piston rod equation of motion:

$$v_{cyl} = \frac{dx_{cyl}}{dt}, \quad (5)$$

$$\frac{dv_{cyl}}{dt} = \frac{p_s \cdot A_{cyl1} - p_t\left(A_{cyl1} - A_{cyl2}\right) - v_{cyl} \cdot \alpha_{cyl} - F_{load}}{m_{cyl}}, \quad (6)$$

Having determined $v_{cyl}(t)$, the unknown flow rates can be calculated:

$$Q_1 = v_{cyl} \cdot A_{cyl1}, \quad (7)$$

$$Q_2 = v_{cyl} \cdot \left(A_{cyl1} - A_{cyl2}\right). \quad (8)$$

The determination of Q_3 requires the equation of the differential valve poppet motion:

$$v_3 = \frac{dx_3}{dt}, \quad (9)$$

$$\frac{dv_3}{dt} = \frac{\left(p_t - p_s\right) \cdot \dfrac{\pi D_3^2}{4} - v_3 \cdot \alpha_3 - k_3 \cdot x_3 - F_{s3}}{m_3}. \quad (10)$$

The range of the x_3 poppet movement is 0 5 mm. The $Q_3(t)$ flow rate through the gap is calculated from Bernoulli's equation, assuming that $p_t(t) \geq p_s(t)$. Otherwise, $Q_3(t) = 0$.

$$Q_3 = c_3 \cdot A_3 \cdot \sqrt{\frac{2\left(p_t - p_s\right)}{\rho}}, \quad (11)$$

where the $A_3(t)$ gap for a standard poppet version with a flat head has a ring shape of D_3 diameter (Fig. 2). Therefore, the gap area is:

$$A_3 = \pi \cdot D_3 \cdot x_3. \quad (12)$$

The $Q_4(t)$ throttle valve flow is calculated similarly to $Q_3(t)$, except that in this case the throttling gap has a fixed area, depending on the x_4 pin position. The gap area can be adjusted by the operator using the valve knob (Fig. 4). The equation is valid when the return line pressure is lower than the load line pressure: $p_{ret} < p_t$.

$$Q_4 = c_4 \cdot A_4(x_4) \cdot \sqrt{\frac{2\left(p_t - p_{ret}\right)}{\rho}}. \quad (13)$$

The $Q_5(t)$ flow rate through the relief valve is also based on a poppet position, whose equation of motion has the following form:

$$v_5 = \frac{dx_5}{dt}, \quad (14)$$

$$\frac{dv_5}{dt} = \frac{\left(p_s - p_{ret}\right)\dfrac{\pi D_5^2}{4} - v_5 \cdot \alpha_5 - k_5 \cdot x_5 - F_{s5}}{m_5}. \quad (15)$$

The F_{s5} initial spring tension provides opening of the valve when the pressure in the supply line exceeds 20 MPa. In this case, a cylindrical gap of D_5 diameter and x_5 width is formed. Hence, the flow rate can be calculated as:

$$Q_5 = c_5 \cdot A_5(t) \cdot \sqrt{\frac{2\left(p_s - p_{ret}\right)}{\rho}}, \quad (16)$$

where:

$$A_5(t) = \pi \cdot D_5 \cdot x_5(t). \quad (17)$$

The presented system of 16 equations: Eqs. (2) to (17) fully describes the parameters of the analysed system. It allows the following time-dependent parameters to be calculated: p_s, p_t pressures, Q_p, Q_1, ..., Q_5 flow rates, x_{cyl}, x_3, x_5 positions, v_{cyl}, v_3, v_5 velocities, and A_3, A_5 gap areas. The presented equations were next used to build a simulation model in Matlab-Simulink.

2.2 Building a Simulation Model

A simulation model was created using a block diagram technique, which is default for research conducted in Simulink. Block diagram models of hydraulic systems were created and analysed, e.g. by Kuehnlein et al.

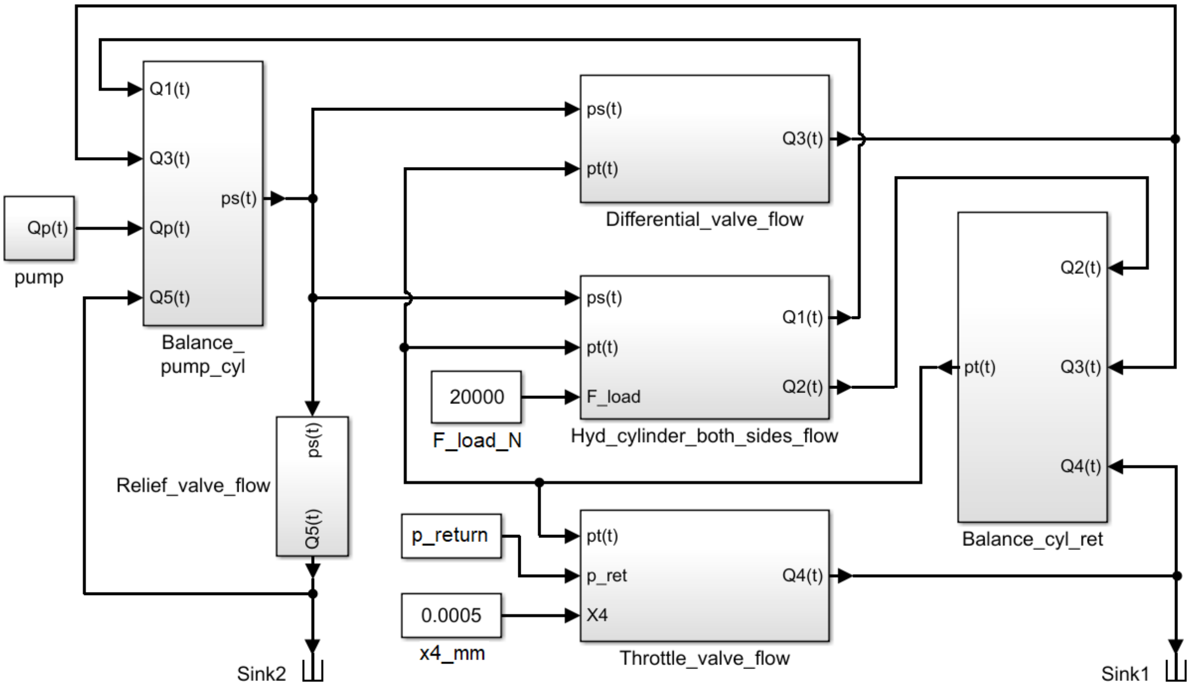

Fig. 6. *Block diagram of the hydraulic system model*

[12], Rybarczyk et al. [13], Milecki and Rybarczyk [14] and Muller and Fales [15]. The authors of this article also have experience in the analysis of hydraulic systems using block diagram models. This technique was used for modelling of a multi-section proportional directional control valve [16] and a proportional flow control valve [17]. A general view of the created simulation model is shown in Fig. 6.

Individual blocks represent the main hydraulic components, while the connectors indicate particular signals, such as pressures and flow rates. The $Q_p(t)$ input signal is a flow rate generated by the pump. First, the $p_s(t)$ supply line pressure is calculated in the Balance_pump_cyl subsystem. Then, the pressure signal is sent to the blocks representing hydraulic components, in order to determine flow rates: $Q_1(t)$, $Q_2(t)$ in Hyd_cylinder_both_sides_flow, and respectively $Q_3(t)$ in Differential_valve_flow and $Q_5(t)$ in Relief_valve_flow. Flow rate values are next used to calculate the $p_t(t)$ load line pressure in the Balance_cyl_ret block. The pressure signal is directed to valve blocks, closing the system and allowing the $Q_4(t)$ throttle valve flow to be determined in the Throttle_valve_flow subsystem. There are also three parameters that can be updated by the user before the simulation starts. Values of the F_load_N payload force and the x4_mm throttle valve position may be entered directly by editing the block properties, while the return line pressure, which is used in multiple blocks, can be changed using a p_return system variable. The fluid temperature has been assumed to be approximately constant (T = 293±2 K), which results in constant density and viscosity. Several significant geometric dimensions and parameters of the fluid adopted for the simulation model, which is hydraulic oil HL 46, are shown in Table 1.

Table 1. *Values of simulation model parameters*

Name	Symbol	Value	Unit
Cylinder diameter	D_{cyl1}	60.0	mm
Rod diameter	D_{cyl2}	32.0	mm
Rel. valve poppet diam.	D_5	12.0	mm
Diff. valve poppet diam.	D_3	9.0	mm
Fluid density	ρ	840	kg·m^{-3}
Fluid kinematic viscosity	ν	41	mm^2·s^{-1}
Fluid bulk modulus	β	103	MPa
Nominal pump flow rate	Q_p	15.0	dm^3·min^{-1}
Relief valve pressure	p_5	20.0	MPa
Return line pressure	p_{ret}	0.1	MPa

Simulations were carried out using a 4th order, built-in, variable-step solver of Simulink. The values of the main configuration parameters are presented in Table 2.

Table 2. *Solver configuration parameters*

Name	Value	Unit
Solver name	ode45	-
Stop time (simulation length)	10	s
Maximum step size	10^{-4}	s
Minimum step size	10^{-7}	s
Initial step size	10^{-4}	s
Relative tolerance	10^{-4}	-
Absolute tolerance	Auto	-

In general, the research was aimed at estimating the piston rod speed as a function of the throttle valve gap width and the payload force. Therefore, the simulations have been conducted for the Cartesian product of the following throttle gap widths: x_4 = (0.00, 0.25, 0.50, 0.75, 1.00, 1.50, 2.00, 3.00) mm and the payload force of: F_{load} = (1.0, 5.0, 10.0, 12.8, 20.0, 30.0) kN.

3 SIMULATION RESULTS

Example simulation results obtained with a fixed position of the throttle valve pin x_4 = 1.00 mm for different F_{load} = 1.0 kN and F_{load} = 20.0 kN payload force values are shown in Figs. 7 and 8, respectively. The results include $x_{cyl}(t)$ piston rod displacement against time and the following flow rate values: a $Q_1(t)$ hydraulic cylinder inflow rate, a Q_3(t) differential valve flow rate and a Q_4(t) throttle valve flow rate. It arises from the charts that in the case when the payload force is low (Fig. 7), additional stream Q_3 from the return line gives a considerable increase in the piston rod speed. In contrast, if the payload force is higher than a threshold value (Fig. 8), the flow through the differential valve is cut off (Q_3 = 0) and the rod speed is more than two times lower.

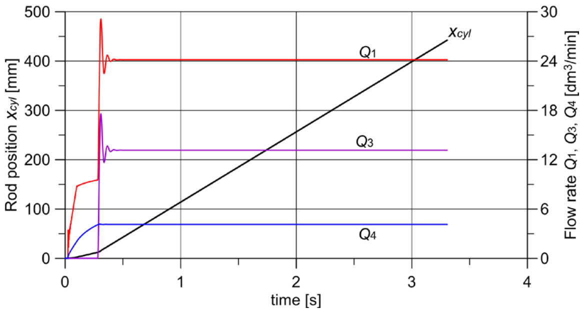

Fig. 7. Simulation results obtained for x_4 = 1.0 mm and F_{load} = 1.0 kN; x_{cyl} piston rod displacement; Q_1, Q_3, Q_4 flow rate

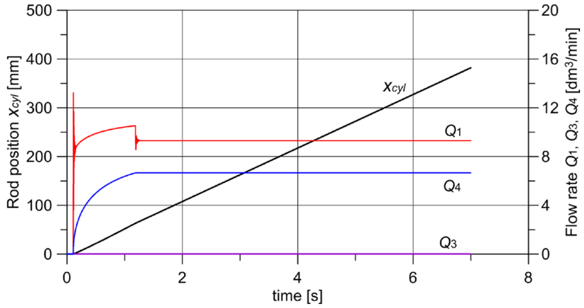

Fig. 8. *Simulation results obtained for x_4 = 1.0 mm and F_{load} = 20 kN; x_{cyl} piston rod displacement; Q_1, Q_3, Q_4 flow rate*

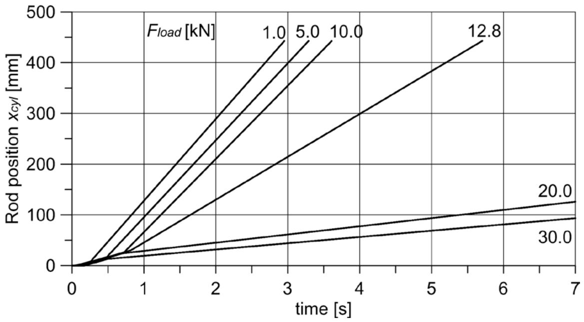

Fig. 9. *Piston rod displacement (simulation); x_4 = 0.5 mm; F_{load} payload force*

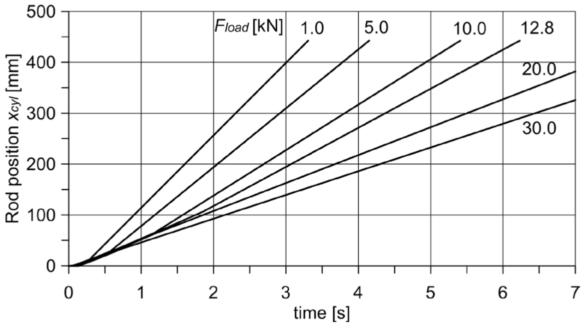

Fig. 10. *Piston rod displacement (simulation); x_4 = 1.0 mm; F_{load} payload force*

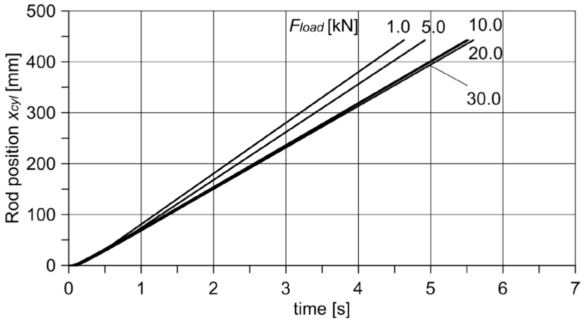

Fig. 11. *Piston rod displacement (simulation); x_4 = 1.5 mm; F_{load} payload force*

Figs. 9 to 11 show summary charts of the piston rod displacement obtained for the following values of the throttling gap width of x_4 = 0.5 mm, x_4 = 1.0 mm and x_4 = 1.5 mm, respectively, while the $v_{cyl} = f(x_4, F_{load})$ resultant surface created on the basis of the values is shown in Fig. 12. As seen in the figures, if the gap width is relatively small (x_4 = 0.5 mm), the speed of the cylinder rod which depends on the payload force, shows a clear division into two areas. The simulations allowed a threshold value to be determined, which was F_{load} = 12.8 kN. For $F_{load} \leq$ 10 kN, the hydraulic actuator rod reaches the speed of v_{cyl} = 120 mm s^{-1} to 150 mm s^{-1}. In contrast, when $F_{load} \geq$ 20 kN, the speed decreases dramatically to the value of v_{cyl} < 20 mm s^{-1}.

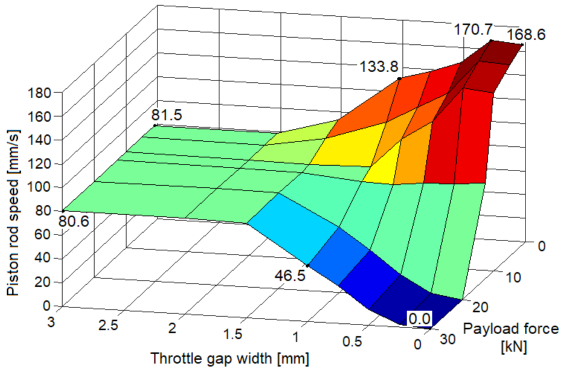

Fig. 12. *Piston rod speed against gap width x_4 and payload force F_{load} (simulation)*

The increase in the throttling gap width makes the range of hydraulic cylinder rod speed change to be significantly reduced. However, the speed obtained for the threshold value of the payload is similar, regardless of the gap width of v_{cyl} = 75.9 mm s^{-1} for x_4 = 1.0 mm and v_{cyl} = 80.4 mm s^{-1} for x_4 = 1.5 mm. The results also indicate that the difference in the piston rod speed for $x_4 \geq$ 2.0 mm is negligible. The average values of the piston rod speed are presented in Table 3.

Table 3. *Piston rod speed vcyl against x_4 and F_{load} (simulation)*

	x_4 [mm]							
F_{load} [kN]	0.00	0.25	0.50	0.75	1.00	1.50	2.00	3.00
1.0	168.6	170.7	150.0	141.1	133.8	95.6	81.3	81.5
5.0	161.3	162.8	134.6	121.1	106.7	90.0	81.2	81.5
10.0	149.9	152.6	122.6	106.2	81.8	80.5	81.0	81.3
12.8	81.1	78.5	77.6	75.1	75.9	80.4	80.9	81.2
20.0	0	3.7	18.0	36.9	54.6	80.2	80.7	81.0
30.0	0	2.0	13.3	31.4	46.5	79.2	80.3	80.6

4 TEST BENCH EXPERIMENTS

The results of simulations were verified on a test bench using a prototype of the valve. The test bench has been built according to the schematic shown in Fig. 13.

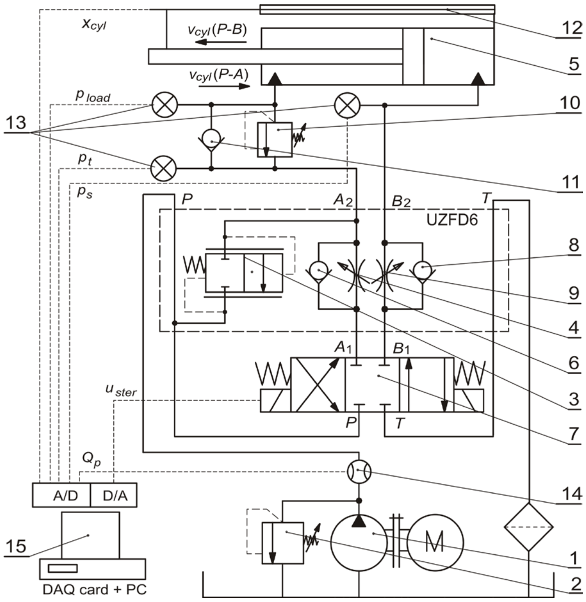

Fig. 13. *Test bench schematic: (1) pump, (2), (10) relief valve, (3) differential valve, (4), (9) throttle valve, (5) hydraulic actuator, (6), (8), (11) check valve, (7) control valve, (12) LVDT transducer, (13) pressure transducers, (14) flow meter, (15) DAQ card and PC*

The supply unit includes a pump (1) and a relief valve (2). The *UZFD6* prototype valve consists of a differential valve (3), two check valves (6), (8) and two adjustable throttle valves (4), (9). The *UZFD6* valve is rigidly connected to the control valve (7), which provides flow continuity through the P supply port, the T return port, and the $A_1 - A_2$, $B_1 - B_2$ operating ports. Depending on the u_{ster} control valve settings, the right or left side of a hydraulic cylinder (5) is supplied. When the piston rod is sliding out ($P - B_1$), the payload force is generated by a pressure relief valve (10). Otherwise ($P - A_1$), the fluid flows through the check valve (11). A manually operated *VS*350 *Parker* valve was used as a payload generator. Flow characteristics of the valve are shown in Fig. 14.

All input and output signals are managed by a *NI PCIe*-6321 card with a *SCB*-68*A* wiring terminal. The following parameters are measured and acquired during the experiments: $Q = Q_p - Q_5$ supply flow rate (14), x_{cyl} rod displacement (12), and pressures, respectively p_s in the supply line, p_{load} in the load line and p_t in the return line (13). The u_{ster} signal allows an operator to change the control valve (7) setting during the experiment. A general view of the test bench is shown in Fig. 15, and the valve prototype can be seen in Fig. 16.

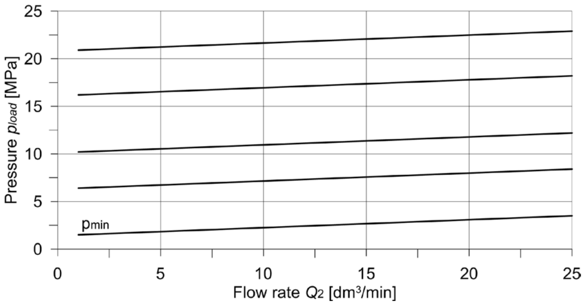

Fig. 14. *Relief valve flow characteristics*

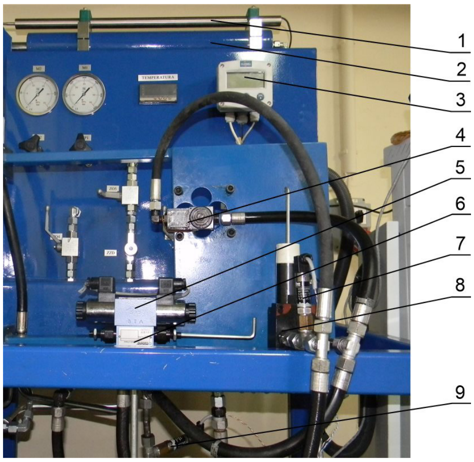

Fig. 15. *Test bench view: (1) LVDT transducer, (2) hydraulic actuator, (3) flow rate gauge, (4) check valve, (5) control valve, (6) UZFD6 valve, (7), (9) pressure transducer, (8) payload generating relief valve*

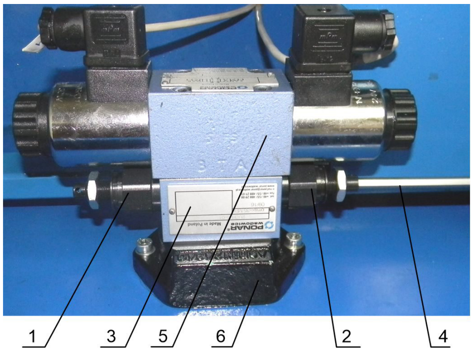

Fig. 16. *The studied valve at the test bench: (1), (2) throttle valve knob, (3) UZFD6 valve, (4) handle, (5) control valve, (6) mounting plate*

Before each laboratory test, the piston rod is set to x_{cyl} = 0.0 mm. Next, the p_{load} load line pressure and the x_4 throttle valve gap width are set by means of knobs of the relief valve and the throttle valve. The power supply is turned on, the control valve is set to the $P - B_1$ position, and the rod moves out. After reaching the maximum extension, an operator sets the control valve to the $P - A_1$ position, and the rod moves in the opposite direction, returning to the starting position.

The actual value of the payload force can be calculated basing on the difference between the load line pressure and the return line pressure:

$$F_{load} = \frac{\pi}{4}\left(D_{cyl1}{}^2 - D_{cyl2}{}^2\right)\cdot\left(p_{load} - p_t\right). \quad (18)$$

Example results of the laboratory tests obtained with a fixed position of the throttle valve pin x_4 = 1.0 mm for different values of the payload force of F_{load} = 1.53 kN and F_{load} = 19.11 kN are shown in Figs. 17 and 18, while the summary charts are presented in Figs. 19 to 21.

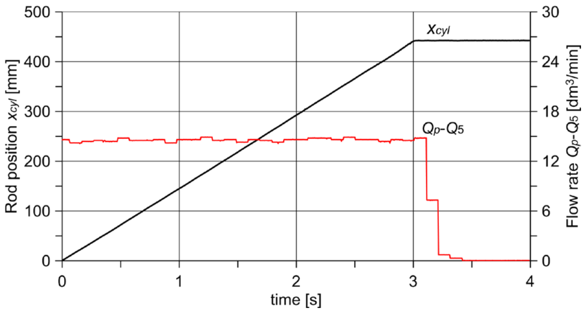

Fig. 17. *Laboratory results obtained for x_4 = 1.0 mm and F_{load} = 1.53 kN; x_{cyl} piston rod displacement; Q_p - Q_5 supply flow rate*

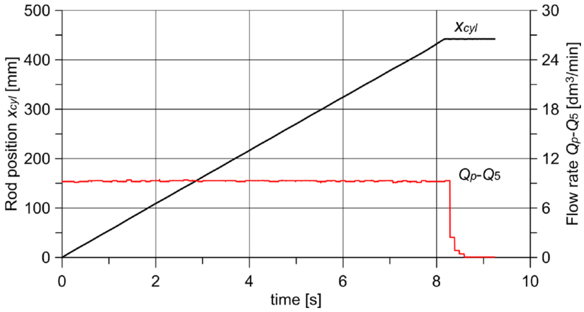

Fig. 18. *Laboratory results obtained for x_4 = 1.0 mm and F_{load} = 19.11 kN; x_{cyl} piston rod displacement; Q_p - Q_5 supply flow rate*

As seen in Figs. 17 and 18, the end position of the piston rod was achieved after 3.0 s in the case of the payload force of F_{load} = 1.53 kN, and after 8.1 s for F_{load} = 19.1 kN. Thus, the speed was decreased by 2.7 times.

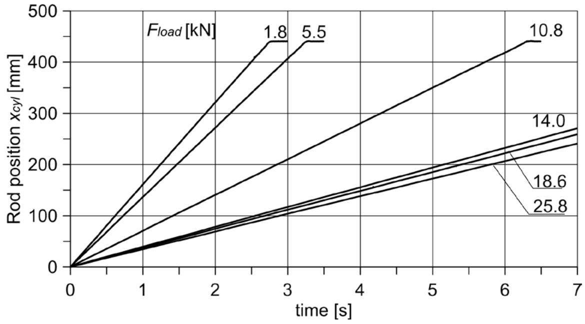

Fig. 19. *Piston rod displacement (experiment); x_4 = 0.5 mm; F_{load} payload force*

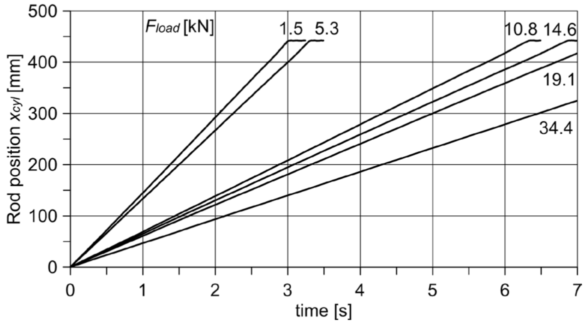

Fig. 20. *Piston rod displacement (experiment); x_4 = 1.0 mm; F_{load} payload force*

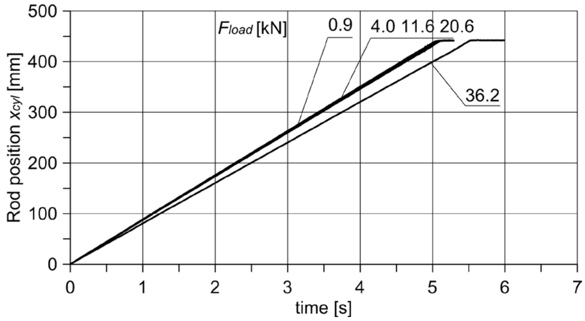

Fig. 21. *Piston rod displacement (experiment); x_4 = 1.5 mm; F_{load} payload force*

The average values of the piston rod speed obtained during the test bench experiments are presented in Table 4. It was taken into account that, unlike simulations, the actual payload force values for individual tests were not exactly the same. A resultant surface of $v_{cyl} = f(x_4, F_{load})$ based on the experimental piston rod speed values is shown in Fig. 22.

The comparison of simulation results (Figs. 7 to 12, Table 3) with the laboratory experiments (Figs. 17 to 22, Table 4) show a high degree of convergence. In both cases, the obtained values of piston rod speed are close. Furthermore, a clear difference in piston rod speed that depends on the payload force can be observed.

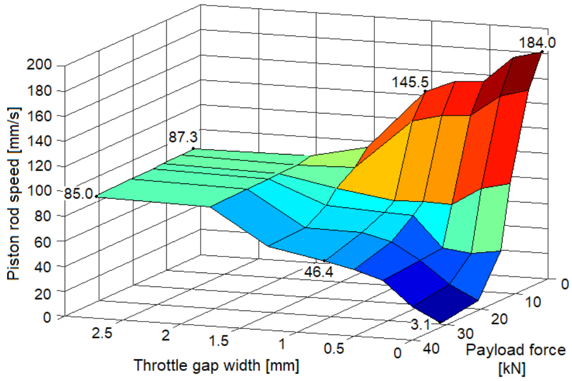

Fig. 22. *Piston rod speed against gap width x_4 and payload force F_{load} (experiment)*

5 SUMMARY

This article provides an analysis of an innovative valve that uses the energy of a return fluid stream from a hydraulic actuator to increase the piston rod speed of movement. At the beginning, a mathematical model was formulated. Next, piston rod speed was determined for various variants of the payload

Table 4. *Piston rod speed v_{cyl} against x_4 and F_{load} (experiment)*

	x_4 [mm]							
	0.00	0.25	0.50	0.75	1.00	1.50	2.00	3.00
F_{load} [kN]	3.6	3.4	2.8	2.7	5.4	1.0	0.9	1.0
v_{cyl} [mm·s^{-1}]	184.0	177.8	156.9	158.6	126.8	87.9	87.6	87.3
F_{load} [kN]	6.1	5.9	5.5	5.7	10.8	4.0	4.0	4.1
v_{cyl} [mm·s^{-1}]	157.8	151.7	134.7	143.0	69.7	86.5	85.2	86.6
F_{load} [kN]	11.3	11.1	10.8	11.0	14.6	11.6	11.2	11.7
v_{cyl} [mm·s^{-1}]	89.5	84.2	70.0	77.6	64.2	86.5	84.8	86.8
F_{load} [kN]	14.0	18.8	18.6	26.5	19.1	20.6	20.6	20.9
v_{cyl} [mm ·s^{-1}]	39.3	19.3	36.9	51.1	56.1	86.2	83.6	85.0

force and the flow rate through the throttling valve using Matlab-Simulink. To validate the results of the theoretical analysis, a test bench was built. The laboratory tests carried out at the bench were analogous to those conducted during simulations. The obtained experimental results confirmed that redirecting the return flow from the actuator to the supply line can more than double the movement speed of the piston rod operating at low load. In general, the proposed solution is advantageous, since it provides significant shortening of the operating time due to the speed increase without the need to install a more efficient pump and thus not only reduces energy demands but is also cost-effective. Compared to the commonly used direct connection between the supply line and the return line, the proposed solution is more adjustable. In addition to the speed increase, it also provides speed reduction under large load and, due to the sandwich type connection port arrangement, it can be easily installed in existing systems without the need to use additional equipment.

6 REFERENCES

[1] Lin, T., Wang, L., Huang, W., Ren, H., Fu, S., Chen, Q. (2017). Performance analysis of an automatic idle speed control system with a hydraulic accumulator for pure electric construction machinery. *Automation in Construction*, vol. 84, p. 184-194, **DOI:10.1016/j.autcon.2017.09.001**.

[2] Perez, J.A.L., De Pieri, E.R., De Negri, V.J. (2018). Force control of hydraulic actuators using additional hydraulic compliance. *Strojniški vestnik - Journal of Mechanical Engineering*, vol. 64, no. 10, p. 579-589, **DOI:10.5545/sv-jme.2018.5339**.

[3] Wang, J., Sun, Y., Huang, X., Li, Z., Han, Y. (2015). Research on the position-pressure master-slave control for a rolling shear hydraulic servo system. *Strojniški vestnik - Journal of Mechanical Engineering*, vol. 61, no. 4, p. 265-272, **DOI:10.5545/sv-jme.2014.2291**.

[4] Wang, W., Wang, B. (2016). An energy-saving control strategy with load sensing for electro-hydraulic servo systems. *Strojniški vestnik – Journal of Mechanical Engineering*, vol. 62, no. 12, p. 709-716, **DOI:10.5545/sv-jme.2016.3685**.

[5] Liu, J., Xie, H., Hu, L., Yang, H., Fu, X. (2017). Realization of direct flow control with load pressure compensation on a load control valve applied in overrunning load hydraulic systems. *Flow Measurement and Instrumentation*, vol. 53, p. 261-268, **DOI:10.1016/j.flowmeasinst.2016.07.004**.

[6] Adeoye, A.O.M., Aderoba, A.A., Oladapo, B.I. (2017). Simulated design of a flow control valve for stroke speed adjustment of hydraulic power of robotic lifting device. *Procedia Engineering*, vol. 173, p. 1499-1506, **DOI:10.1016/j.proeng.2016.12.230**.

[7] Xie, H., Liu, J., Hu, L., Yang, H., Fu, X. (2015). Design of pilot-assisted load control valve for proportional flow control and fast opening performance based on dynamics modeling. *Sensors and Actuators A: Physical*, vol. 235, p. 95-104, **DOI:10.1016/j.sna.2015.09.042**.

[8] Man, Z., Ding, F., Ding, C., Liu, S. (2015). Study of an energy regeneration system with accumulator for hydraulic impulse testing equipment. *Strojniški vestnik - Journal of Mechanical Engineering*, vol. 61, no. 3, p. 196-206, **DOI:10.5545/sv-jme.2014.2138**.

[9] Watton, J., Nelson, R.J. (1993). Evaluation of an electrohydraulic forge valve behavior using a CAD package. *Applied Mathematical Modelling*, vol. 17, no. 7, p. 355-368, **DOI:10.1016/0307-904X(93)90060-T**.

[10] Naseradinmousavi, P., Nataraj, C. (2011). Nonlinear mathematical modeling of butterfly valves driven by solenoid actuators. *Applied Mathematical Modelling*, vol. 35, no. 5, p. 2324-2335, **DOI:10.1016/j.apm.2010.11.036**.

[11] Casoli, P., Pompini, N., Riccò, L. (2015). Simulation of an excavator hydraulic system using nonlinear mathematical models. *Strojniški vestnik - Journal of Mechanical Engineering*, vol. 61, no. 10, p. 583-593, **DOI:10.5545/sv-jme.2015.2570**.

[12] Kuehnlein, M., Liermann, M., Ewald, J., Murrenhoff, H. (2012). Adjustable flow-control valve for the self-energising electro-hydraulic brake. *International Journal of Fluid Power*, vol. 13, no. 2, p. 5-14, **DOI:10.1080/14399776.2012.10781049**.

[13] Rybarczyk, D., Sędziak, D., Owczarek, P., Owczarkowski, A. (2015). Modelling of electrohydraulic drive with a valve controlled by synchronous motor. In: Szewczyk R., Zieliński C., Kaliczyńska M. (eds.) *Progress in Automation, Robotics and Measuring Techniques. Advances in Intelligent Systems and Computing*, vol. 350, p. 215-222, **DOI:10.1007/978-3-319-15796-2_22**.

[14] Milecki, A., Rybarczyk, D. (2015). Modelling of an electrohydraulic proportional valve with a synchronous motor. *Strojniški vestnik - Journal of Mechanical Engineering*, vol. 61, no. 9, p. 517-522, **DOI:10.5545/sv-jme.2015.2553**.

[15] Muller, M.T., Fales, R.C. (2008). Design and analysis of a two-stage poppet valve for flow control. *International Journal of Fluid Power*, vol. 9, no. 1, p.17-26, **DOI:10.1080/14399776.2008.10781293**.

[16] Lisowski, E., Filo, G., Rajda, J. (2015). Pressure compensation using flow forces in a multi-section proportional directional control valve. *Energy Conversion and Management*, vol. 103, p. 1052-1064, **DOI:10.1016/j.enconman.2015.07.038**.

[17] Lisowski, E., Filo, G. (2016). CFD analysis of the characteristics of a proportional flow control valve with an innovative opening shape. *Energy Conversion and Management*, vol. 123, p. 15-28, **DOI:10.1016/j.enconman.2016.06.025**.

Strojniški vestnik - Journal of Mechanical Engineering 65(2019)2, 113-122

DOI:10.5545/sv-jme.2018.5656 Original Scientific Paper
Received for review: 2018-07-18
Received revised form: 2018-12-17
Accepted for publication: 2019-01-14

A Novel Approach for Identifying Gas Cavitation in Oil Jet Pumps for Lubrication Systems

Jun Zhang[1] – Peiyong Ma[1] – Shuyi Gan[1] – Xianguo Hu[1,*] – Shunsen Wang[2]
[1] Hefei University of Technology, School of Mechanical Engineering, China
2 Xi'an Jiaotong University, Institute of Turbomachinery, China

Gas cavitation has significant influence on the performance of oil jet pumps for lubrication systems in turbo machinery. This study provides a novel approach for identifying gas cavitation in oil jet pumps. It accounts for the physical process of gas cavitation and its effect on the performance of oil jet pumps. The performance of oil jet pumps, such as their entrainment ability, efficiency, cavitation erosion, vibration, noise, vapour volume fraction, and pressure distribution under variable working conditions, are systematically measured and quantified from experimental and numerical simulation results. Based on the frequency characteristics of the cavitation process and its action mechanism on the performance of oil jet pumps, a novel approach for the identification of gas cavitation is provided. Results show that gas cavitation emerges in a fairly wide working range of oil jet pumps for lubrication systems. Here, the dissolved air content in lubrication oil is 6.3 times larger than that in water, and the oil jet pump is more prone to suffer from cavitation than a water jet pump by 16 %. This study promotes a deeper understanding of the mechanics of gas cavitation effects on the fluid machinery in lubrication systems.
Keywords: oil jet pump, lubrication system, identification of gas cavitation, frequency characteristics, gas-liquid two-phase flow

Highlights
- *Gas cavitation in oil jet pumps was measured and analysed with experiment and CFD methods.*
- *A novel approach for the identification of gas cavitation in oil jet pumps was provided.*
- *Gas cavitation in oil jet pumps emerges at σ = 1.68 and fades at σ = 1.31 with dissolved air content f_g = 110 ppm in lubrication oil.*

0 INTRODUCTION

The oil jet pump is the key component of lubrication systems for turbo machinery. It is used to supply lubrication oil for the bearing and sealing system. However, with the increasing power density of turbo machinery, the working parameters and load of lubrication system increase rapidly. The cavitation problem of oil jet pumps gradually threats the safe operation of turbo machinery [1] and [2].

Cavitation in fluid machinery powered by water has already been extensively studied, such as marine propeller [3], hydrofoils [4] and [5], nozzles [6], washing machines [7], bluff bodies [8], etc. Cavitation in the journal bearings of lubrication systems has also been studied for a long time [9] and [10]. However, cavitation in oil jet pumps for lubrication systems is different from that in hydraulic machinery powered by water or journal bearings.

Fig 1 shows the structure of an oil jet pump. As shown, the oil jet pump entrains with high working pressure, so the pressure in throat decreases and air separates from oil in the low pressure region. The separated air takes up flow passage and the local sound speed is reduced with multiphase flow [11]. Therefore, the particularities of the cavitation problem in oil jet pumps for the lubrication systems of turbo machinery are shown in two aspects. First, the working pressure in the lubrication system commonly is above 2 MPa, which brings about extremely high velocity, low pressure, and cavitation regions [6] and [12]. Second, the dissolved air content in lubrication oil is ten times higher than that in water [13] and [14], which promotes air cavitation and noticeably affects the lubrication system [15] and [16]. As a result, studying the cavitation characteristics of oil jet pumps in lubrication systems is of great significance for the safety of turbo machinery.

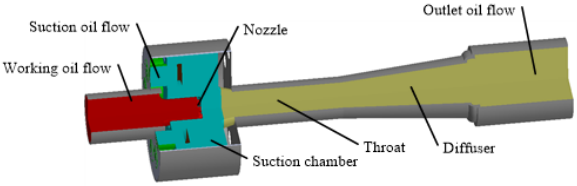

Fig. 1. *Structure of oil jet pump*

Among various kinds of cavitation in oil jet pumps, gas cavitation is a special kind of cavitation and significantly affects the performance of such pumps. According to Cunningham and Brown's effort in comparing the cavitating flow in oil jet pumps

*Corr. Author's Address: Hefei University of Technology, School of Mechanical Engineering, Tunxi Road 193#, Hefei, Anhui, China, xghu@hfut.edu.cn

with water jet pumps [17], it is found that the oil jet pump is more prone to suffer from cavitation than the water jet pump was. Additionally, Long et al. [18] showed that the choking flow of jet pumps result from the zone of Mach number equals 1 filling the cross section of throat. Therefore, we infer that gas cavitation is able to promote the choking flow of jet pumps; later experimental results had confirmed this. Zhang et al. [19] established an improved cavitation model suitable for the cavitating flow of lubrication oil in a lubrication system based on experimental data. According to this study, the maximum flow capacity of the throat pipe is three times reduced with the increase of non-condensable gas content in lubrication oil. Zou et al. [20] studied the cavitating flow in a non-circular opening spool valve in a hydraulic system. The results show that there is a critical point of non-choking transforming choking flow. However, irrespective of the dissolved air in hydraulic oil, the numerical simulation results are void of this point. The above results support that the large amount of dissolved air in lubrication oil promotes the gas cavitation and choking flow. Compared with that in a water jet pump, its effect on an oil jet pump is significant and cannot be ignored. Therefore, studying the identification of gas cavitation and its effect on the performance of oil jet pumps is especially important.

The difficulty of gas cavitation identification lies in that it is similar to vapour cavitation, such as leading to gas-liquid two-phase flow and occupying the flow passage. Thus, an unconventional method is required for identification. Duke et al. [21] measured the total displacement of the liquid and mass fractions of both dissolved and nucleated gas from Br and Kr fluorescence. Then, the volumetric displacement of liquid due to both cavitation and gas precipitation can be separated through the estimation of the local equilibrium-dissolved mass fraction. Zhou et al. [16] presented a novel lumped parameter model of cavitating orifice flow based on the control volume concept. They proposed a procedure of calibrating the unknown model coefficients in the presented mode, and the calibrated model is verified by experiments. Although their study provided an approach for the identification of gas cavitation, it lacks deep analysis of the physical process and mechanism. Therefore, their results are of limited significance for the identification of gas cavitation in fluid machinery powered by lubrication oil.

Some researchers study the influence of gas cavitation on the lubrication or hydraulic system. Kim and Murrenhoff [22] measured the effective bulk modulus of hydraulic oil to improve the simulation accuracy of cavitation, which accounts for the effect of dissolved air separated from oil. Zhou et al. [23] provided a novel approach for the prediction of thermal effects arising from gas cavitation in a hydraulic circuit.

In contrast, the cavitation model was also improved to predict the occurrence of gas cavitation. The cavitation models proposed by Kunz et al. [24] and Sauer [25] scarcely account for the effect of gas cavitation, which were improved in the full cavitation model proposed by Singhal et al. [26]. The full cavitation model accounts for the formation and transport of vapour bubbles, the turbulent fluctuations of pressure, and the magnitude of non-condensable gas. Li et al. [15] presented a new gas cavitation model based on air solubility in lubricant and the full cavitation model. The model is validated for fixed-geometry oil-film journal bearings at different eccentricity ratios. These results indicate the influence of gas cavitation on the elasticity modulus and the thermal effect of the gas-liquid mixture. However, it is still without the physical process and the exact identification of gas cavitation in fluid machinery.

As shown above, despite the gas and vapour cavitation both emerging in the low pressure region and take up the flow passage, their physical process are different [27]. The physical process of gas cavitation is the mass diffusion of dissolved air in oil and through interface. The physical process of vapour cavitation is the phase transition of vapour and liquid phase, and the process of phase transition is considerably quicker than mass diffusion process [28] and [29]. Furthermore, their effects on the performance of oil jet pumps are also different, which are used for the identification of gas cavitation in this study.

This study takes the gas cavitation in oil jet pumps for lubrication systems as its research subject. The gas cavitation was obtained with oil jet pumps operating under variable working conditions. The performance of oil jet pumps was systematically measured and quantified, and the performance curves of oil jet pumps under variable working conditions were obtained with experiments. Then, the frequency characteristics of cavitation and its action mechanism on the entrainment ability, efficiency, cavitation erosion ability, vibration, noise, vapour volume fraction of oil jet pumps were deeply and systematically analysed. Finally, a novel approach for the identification of gas cavitation and its effect on the performance of oil jet pumps were provided.

1 EXPERIMENTAL SETUP

An experimental rig was constructed to simulate the environment of an oil jet pump in a lubrication system. Its schematic is shown in Fig. 2. The parameters of the oil jet pump are from a lubrication system in a power plant, with $m = 7.47$, $t = 65$ ºC, $P_o = 2.6$ MPa, P_c in the range of 0.40 MPa to 0.20 MPa, h in the range of 0.08 to 0.2. Their expressions are shown in Eqs. (1) to (3). The volume fraction of dissolved air in lubrication oil is 7.2 % at 65 ºC, 1 atm based on the study of Ding and Fan **[13]**, equivalent to a mass fraction of 110 ppm.

The measured performance of the oil jet pump includes the entrainment ratio, efficiency, pressure distribution, cavitation erosion ability, vibration, and noise. Measurement points on the oil jet pump are shown in Fig. 3. Measurement ranges and accuracies of the experimental instruments are shown in Table 1. There are four PCB piezoelectric sensors arranged on the throat of the oil jet pump; their distances from the throat entrance are 0.5 D_t, 1 D_t, 1.5 D_t, 2.5 D_t respectively. Experimental results show that its maximum value emerges under variable working conditions. Thus, the maximum value among four points is taken as the representative parameter of oil jet pump. There are seven pressure transmitters arranged along flow direction, with distances of 0.5 D_t, 1 D_t, 1.5 D_t, 2.5 D_t, 4 D_t, 5 D_t from the throat entrance respectively. Two vibration sensors are arranged on the throat and outlet pipe. A noise sensor is arranged outside the oil jet pump in a field 1 m distant. The measured dynamic parameters include cavitation

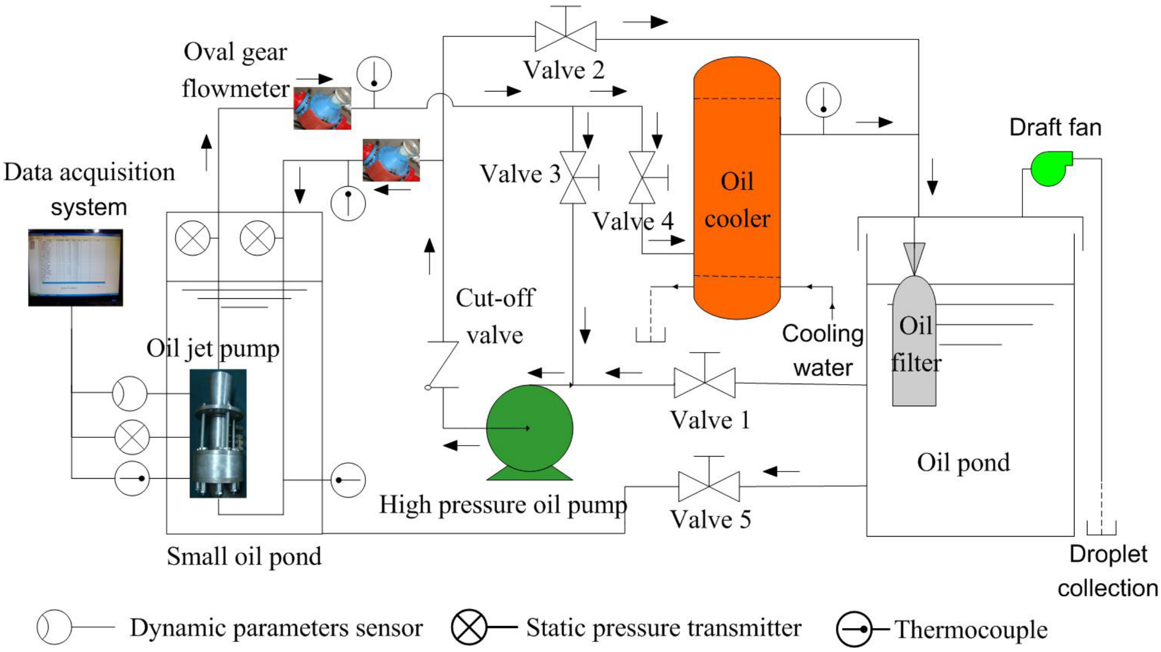

Fig. 2. *Schematic of experimental rig*

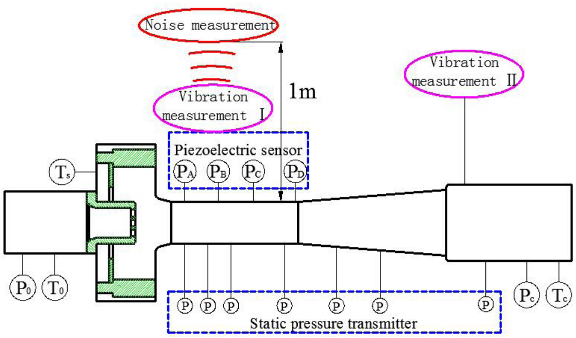

Fig. 3. *Arrangement of measuring points on the oil jet pump*

erosion ability, vibration, noise, and their pictures are shown in Fig. 4.

Position along flow direction $$L_o = \frac{L}{D_t}, \tag{1}$$

area ratio $$m = \frac{F_t}{F_o}, \tag{2}$$

pressure ratio $$h = \frac{P_c - P_s}{P_o - P_c}. \tag{3}$$

a)  b) 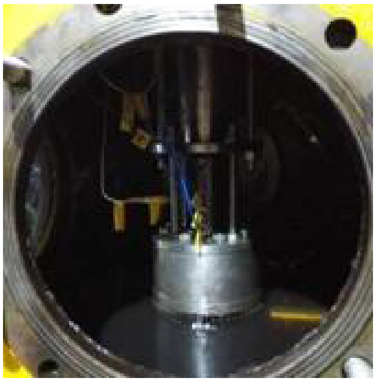 c) 

Fig. 4. *Arrangement of dynamic parameter measurement points on the oil jet pump; a) PCB piezoelectric sensor, b) vibration sensor, c) noise sensor*

Table 1. *Measurement ranges and accuracies of the experimental instruments*

Measurement parameter	Instrument	Range and accuracy
Volume flow rate	Oval gear flow meter	10 m³/h to 60 m³/h, ±0.5%
Pressure	Rosemount high precision pressure transmitter	0 MPa to 4 MPa, ±0.1 %
Temperature	T type thermocouple	–50 °C to 350 °C, ±0.4 %
Cavitation erosion ability	PCB piezoelectric sensor	0 MPa to 7 MPa, 500 kHz
Vibration	PCB acceleration sensor	200 kHz
Noise	PCB microphone	200 kHz

2 NUMERICAL SIMULATION METHOD

The three-dimensional oil jet pump is filled with unstructured grids, as shown in Fig. 5. The grid number was initially 9.2 million and later increased to 14.7 million to ensure the grid independence of simulation results.

The Fluent commercial computational fluid dynamics (CFD) code was employed in the simulation. The averaged Reynolds number in the nozzle and throat zone is 3×10^6. Thus, the turbulence flow was solved with realizable k-epsilon model together with the standard wall functions. The $y+$ value on the boundaries is about 23 in the key flow area. The mixture model and full cavitation model developed by Singhal et al. [26] were employed to account for the effect of dissolved air in the lubrication oil.

Fig. 6 shows the boundary conditions of oil jet pump. Pressure boundary conditions were applied to the inlets and outlet boundaries. Each boundary was extended by 3 times of its pipe diameter. The boundaries were supplied with turbulence intensity of 5 % and the hydraulic diameter of each pipe to eliminate the effect of backflow and ensure inflow condition. The SIMPLEC was employed to couple the pressure and velocity. The second order upwind was used for the discretization of convection terms. The solution was iterated until the residues for each equation were below 1×10^{-4}, and the net flux of inlets and outlet boundaries fluctuates in 1 %. Later, the simulation results were validated with experimental data; the relative error does not exceed 4 %.

Typically, about 24 h were needed to obtain a converged result for one case, which was calculated on a DELL Workstation (Intel(R) Xeon(R) Gold 5118 Processor @2.3 GHz (12 CPUs), DDR4 32G Running Memory).

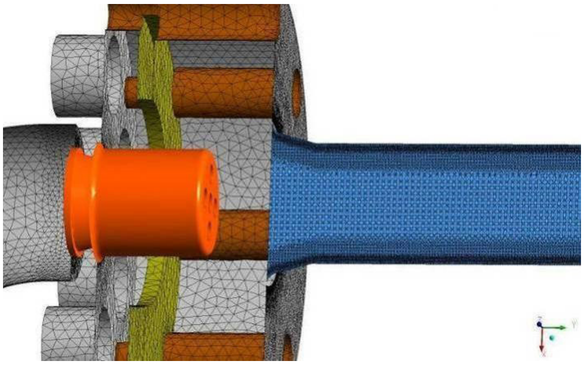

Fig. 5. *Calculation domain and grids of oil jet pump*

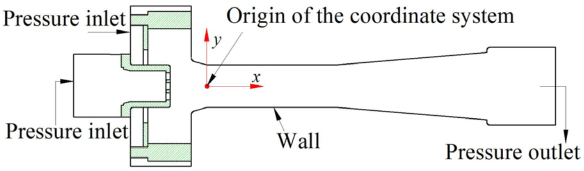

Fig. 6. *Boundary conditions of oil jet pump*

3 QUANTIFICATION OF THE DYNAMIC PARAMETERS

The measured performance of the oil jet pump includes entrainment, efficiency, cavitation erosion ability, vibration, and noise. In these parameters, the entrainment, efficiency and cavitation erosion ability are quantified with entrainment ratio q, efficiency η, cavitation intensity E [30]. Their expressions are shown in Eqs. (4) to (6). The quantification of vibration and noise are relatively complicated, because the effective experimental data are affected by the background such as motor of oil pump, pipe, valve, and elbow. In this study, the interfering signal was removed through the frequency characteristics of the cavitation process.

Entrainment ratio $$q = \frac{Q_s}{Q_o}, \tag{4}$$

efficiency $$\eta = \frac{Q_s\left(P_c - P_s\right)}{Q_o\left(P_o - P_c\right)} = q \cdot h, \tag{5}$$

cavitation intensity $$E = \frac{1}{T_{sample}} \cdot \frac{1}{\rho c}\sum_{i=1}^{n} P_i^2 \Delta T_i. \tag{6}$$

3.1 Wavelet Analysis of Signal from PCB Piezoelectric Sensor

The PCB piezoelectric sensor is arranged on the internal pipe wall close to flow, which is able to catch the original signal of cavitation process, as shown in Fig. 7. The frequency characteristics were obtained with the spectral analysis method. However, the conventional Fourier change is no longer suitable for the unilateral signal, which results from bubble collapse and its effect on the wall. Therefore, the wavelet analysis was adopted in this study. A single peak from Fig. 7 was chosen as the analysis object, which is typical and relatively independent of the other peaks. The Mexican Hat function was chosen as wavelet basis function based on its waveform in Fig. 7.

The time domain of single peak and its wavelet analysis results are shown in Fig. 8. The time period of peak emerges in wavelet analysis results corresponding to that in its time domain. Its dominant frequency distributes in the middle and high frequencies, which is concordant with the other pulses in Fig. 7. Fig. 9 shows the frequency distribution of the wavelet analysis result with different pressure ratios. The amplitude of the wavelet analysis goes up with increasing pressure ratio. Their frequency mainly distributes in the range of 5 kHz to 85 kHz, and its peak emerges at 30 kHz.

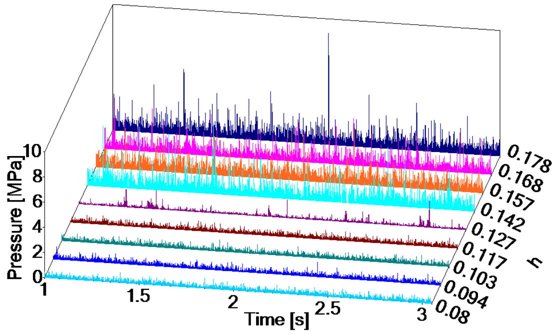

Fig. 7. *Signal from PCB piezoelectric sensors with different pressure ratios*

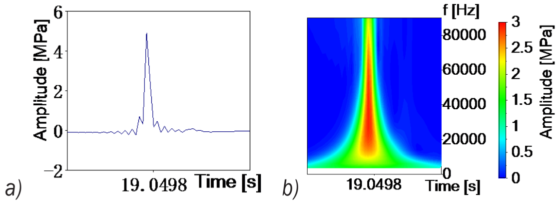

Fig. 8. *Time domain of single peak and its wavelet analysis results: a) time domain, b) wavelet analysis results*

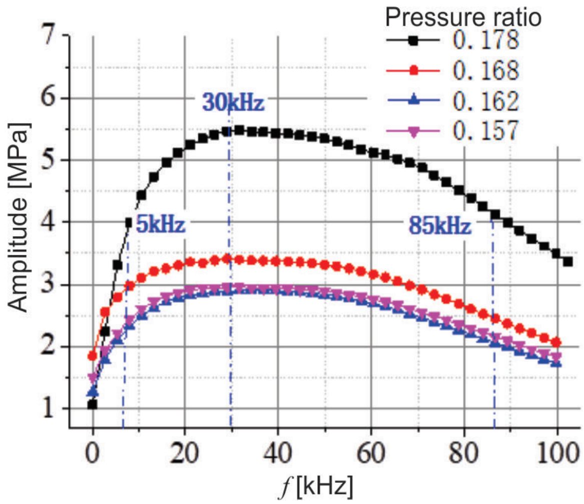

Fig. 9. *Frequency distribution of wavelet analysis result with different pressure ratios*

3.2 Quantification of Cavitation Noise

Fig. 10 shows the 1/12 octave band of sound signal under different working conditions. With the increase of the pressure ratio, the low frequency parts change a little, while their mainly difference appears in the middle and high frequency range with f > 5 kHz. It is obviously that these results are coincident with the wavelet analysis results. It is shown that the noise of cavitation process is based on the single pole sound source radiation noise with wide frequency characteristics, and is mainly distributed in the middle and high frequency ranges with $f > 5$ kHz. As a result, this study takes 5 kHz to 20 kHz as the cavitation noise frequency range, and its corresponding sound pressure level is taken as the quantitative parameter of cavitation noise.

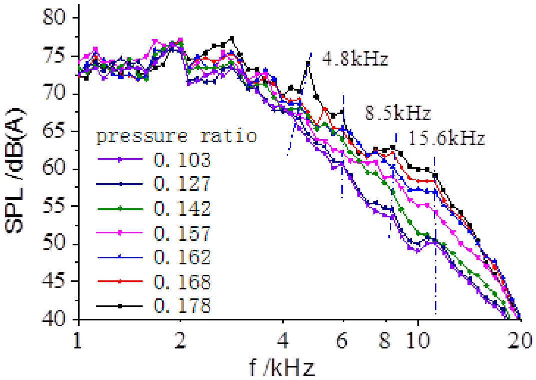

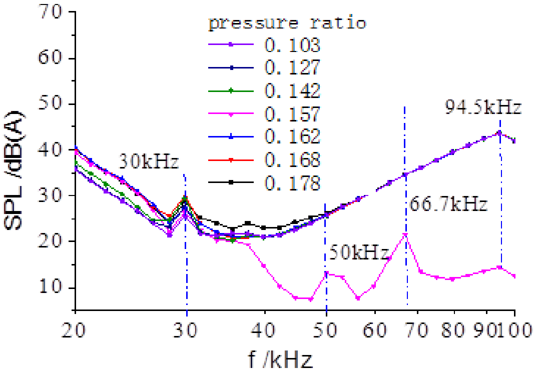

Fig. 10. *Octave of sound signal with different pressure ratios; a) f < 20 kHz, and b) f > 20 kHz*

3.3 Quantification of Cavitation Vibration

In our experiment, there are elastic connections arranged at the inlet and outlet pipes of oil jet pump to isolate the vibration of attachments. Thus, the quantification of cavitation vibration is relatively simple. Fig. 11 shows the acceleration of throat vibration under different working conditions. It is obvious that the peak-to-peak value of vibration acceleration increases rapidly with the increase of pressure ratio. As a result, the P-P value of vibration acceleration is taken as the quantitative parameter of cavitation vibration.

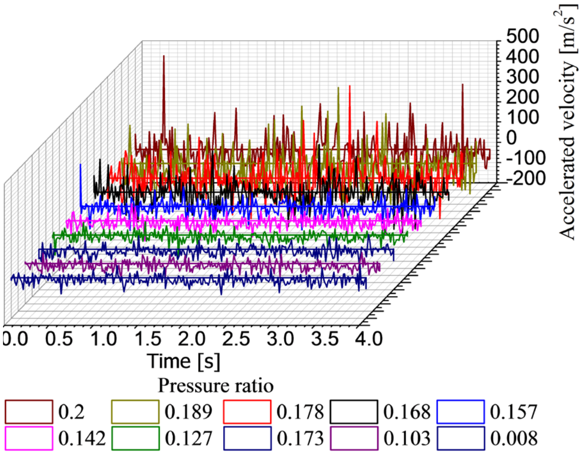

Fig. 11. *Acceleration of throat vibration with different pressure ratios*

4 RESULTS

4.1 Numerical Simulation Results

Figs. 12 and 13 show the distribution of vapour volume fraction in the oil jet pump from numerical simulation. In the pressure ratio range from 0.155 to 0.144, the oil jet pump mainly suffers from gas cavitation. In this range, the pressure in throat decreases with decreasing h and more air separates from lubrication oil. As shown in Fig. 12, the gas cavitation zone remains almost unchanged, and its volume fraction gradually increases with decreasing h.

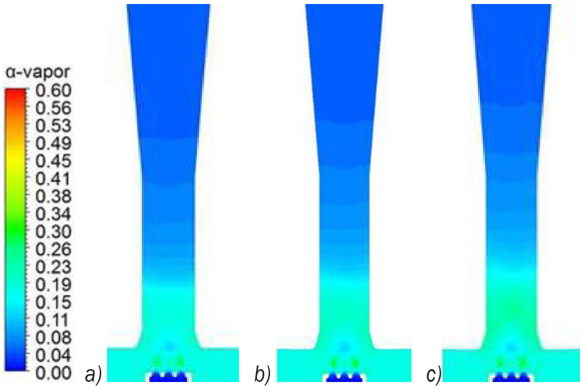

Fig. 12. Vapour volume fraction in oil jet pump with different pressure ratios (gas cavitation);
a) h = 0.155, b) h = 0.15, c) h = 0.144

In the pressure ratio range of 0.102 to 0.139, the oil jet pump mainly suffers from vapour cavitation. In this range, the decreasing low pressure inertia is blocked by the phase change of lubrication oil, and evolves to the increasing phase change region in

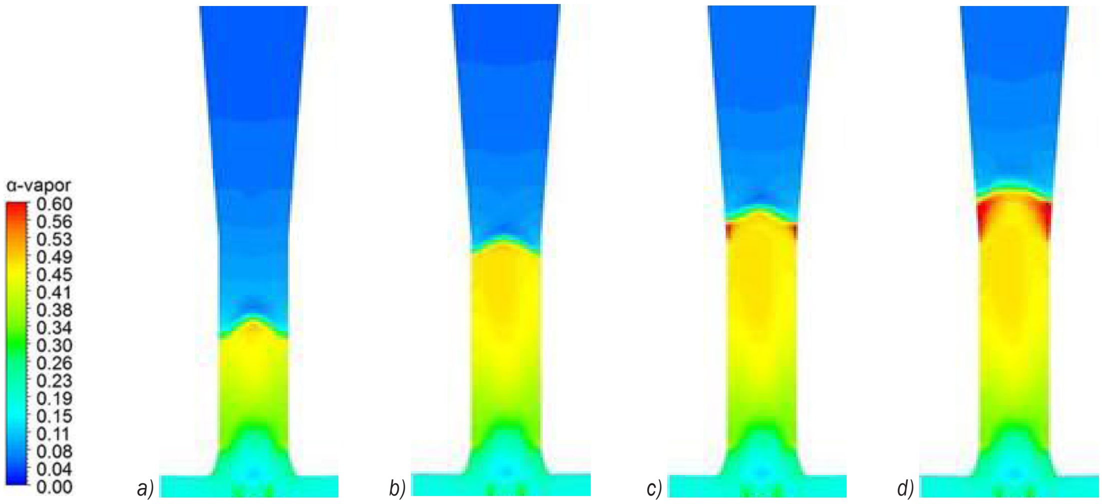

Fig. 13. *Vapour volume fraction in oil jet pump with different pressure ratios (vapour cavitation): a) h = 0.139, b) h = 0.128, c) h = 0.113, d) h = 0.102*

throat. Therefore, the vapour cavitation zone extends downstream until throat is full of cavitation bubbles; the vapour volume fraction also increases with decreasing h, as shown in Fig. 13.

4.2 Experimental Results

Fig. 14 shows the entrainment ratio q, efficiency η, cavitation intensity E, 5 kHz to 20 kHz sound pressure level *SPL*, throat vibration P-P *TPP*, outlet vibration P-P *OPP* change with pressure ratio h from experimental results. Combined with numerical simulation results in Figs. 12 and 13, more details and results were obtained.

(1) Entrainment ratio, q: Due to the emergence of gas cavitation in the throat pipe, the entrainment ratio gradually increases to its maximum with decreasing pressure ratio, and the oil jet pump enters choking flow.
(2) Efficiency, η: The efficiency curve shows a parabolic shape. Its maximum point corresponds to the critical point of non-choking transforming choking flow with h = 0.155, which is also affected by gas cavitation.
(3) Cavitation intensity, E: The cavitation intensity shows a rising trend with increasing pressure ratio, and there is a local minimum point with h = 0.155. These data suggest that moderate gas cavitation is able to decrease cavitation intensity in oil jet pump. More explanation can be found in a previous study **[30]**.
(4) Throat vibration P-P, *TPP*: Since the PCB piezoelectric sensor and vibration sensor were arranged on the inside and outside of throat wall, the throat vibration has a similar change rule with cavitation intensity. However, the pressure ratio of local maximum points varies because of their different formation mechanisms. The local maximum point of throat vibration emerges at the point of non-choking transforming choking flow. During the transformation, the air dissolves from the oil, and the gas-liquid flow leads to the compressibility of the mixture, which leads to the vibration of throat. The local maximum point of cavitation intensity results from the concentrated collapse of cavitation bubbles under choking flow **[30]**.
(5) 5 kHz to 20 kHz sound pressure level, *SPL*: Compared to the throat vibration, the high frequency noise is absent from the local maximum point. That is because, even though the gas cavitation leads to the compressibility of mixture, the dissolution and precipitation process of air are relatively slow compared to the phase change process of the lubrication oil. Therefore, gas cavitation has little effect on high frequency noise, and the *SPL* curve is void of the local maximum point.
(6) Outlet vibration P-P, *OPP*: The outlet vibration curve shows a bowl shape, which is symmetric with efficiency curve. These data shows that gas cavitation has little effect on outlet vibration because it emerges at the upstream part of the throat pipe.

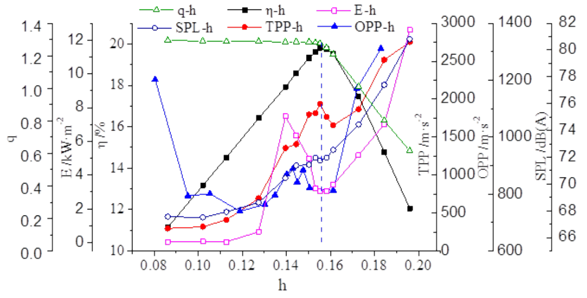

Fig. 14. *Cavitation characteristics of oil jet pump from experimental results*

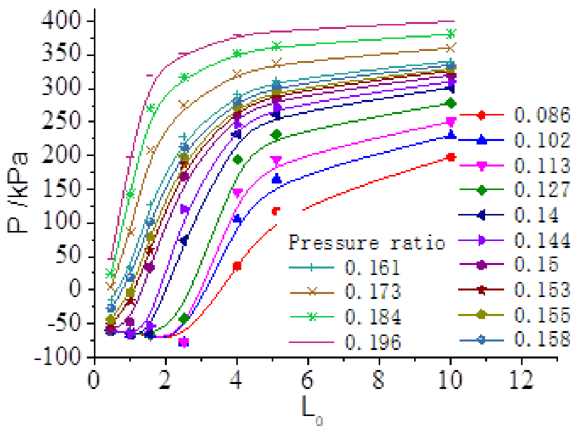

Fig. 15. *Pressure distribution in oil jet pump from experiment*

5 DISCUSSION

In this paper, it is shown that gas cavitation can be identified by its physical process and effect on the performance of oil jet pumps under variable working conditions. It is evident that gas cavitation emerges at the low pressure region of throat pipe, and its primary effect is the transformation from non-choking to choking flow in oil jet pump. This effect is important but is often neglected due to the small amount of dissolved air in water jet pump. However, gas cavitation cannot be neglected for lubrication oil in oil jet pumps. Our study serves for the identification of gas cavitation and analyses in depth its effect on the performance of oil jet pumps.

One important innovation of our study is providing an approach for identifying gas cavitation in oil jet pumps. Compared with vapour cavitation, gas cavitation cannot induce high frequency noise because the generation and collapse process of gas cavitation were limited by the dissolution and precipitation velocity of the dissolved air from lubrication oil. However, gas cavitation produces liquid-gas mixed flow and intensify the vibration. Thus, the gas cavitation is identified by comparison of vibration and high frequency noise under variable working conditions.

Furthermore, our study deeply analysed the effect of gas cavitation on the performance of oil jet pumps based on systematically experimental results. Fig. 15 shows the pressure distribution in oil jet pump from experiment. The cavitation number is obtained with Eq. (7). P_a is the pressure at the beginning of throat pipe, P_v is the vaporization pressure of lubrication oil. Then the critical points of gas cavitation in oil jet pump were obtained, as shown in Table 2.

Cavitation number: $$\sigma = \frac{P_s - P_v}{\rho v_s^2 / 2} = \frac{P_s - P_v}{P_s - P_a}. \quad (7)$$

Table 2. *Critical points of gas cavitation*

Critical point	h = 0.144	h = 0.155	h = 0.161
σ	1.31	1.54	1.68
Q	1.29	1.28	1.21
η [%]	18.58	19.8	19.5
E [W·kg⁻¹]	6.34	3.03	3.46
TPP [m·s⁻²]	1405.3	1937.37	1655.5
OPP [m·s⁻²]	796.4	841.65	821.8
SPL [dB(A)]	71.4	71.74	72.6

From the above, we have identified the dimensionless range of gas cavitation. Gas cavitation emerges in the range of $0.144<h<0.161$, with $1.31<\sigma<1.68$ in this study. These data mean the gas cavitation inception emerges at $h=0.161$ with $\sigma=1.68$ and fades away at $h=0.144$ with $\sigma=1.31$.

Our results confirm and provide quantitative data for the effect of dissolved air on cavitation in oil jet pumps. In this study, the dissolved air content in lubrication oil $f_g=110$ ppm, and the limited cavitation number of oil jet pump $\sigma_L=1.54$, compared to $\sigma_L=1.33$ in water jet pump with $f_g=15$ ppm from Cunningham and Brown [17], the dissolved air content is 6.3 times larger, and the oil jet pump is more prone to suffer from cavitation than water jet pump by 16 %.

Our results suggest a possibility of reducing cavitation erosion with moderate gas cavitation in oil jet pumps. The local minimum cavitation intensity point result from gas cavitation is also the high efficiency point with $h=0.155$ and $\sigma=1.54$. Its cavitation number is 10 % lower than gas cavitation inception, while its throat vibration P-P value is 17 % higher. Additionally, the maximum entrainment ability of oil jet pumps is 6.6 % higher than that of the gas cavitation inception point.

6 CONCLUSION

In this study, a novel approach for identifying gas cavitation in oil jet pumps is provided. Such an approach accounts for the physical process of gas cavitation and its effect on oil jet pumps, which is of great significance for engineering.

The gas cavitation and its effect on the performance of oil jet pumps under variable working conditions are systematically measured and quantified with the entrainment ratio, efficiency, cavitation intensity, 5 kHz to 20 kHz sound pressure level, and vibration P-P value. Additionally, the vapour volume fraction and pressure distribution were obtained to provide more details of gas cavitation in oil jet pumps. Finally, the results of gas cavitation affecting the performance of oil jet pumps are obtained. The main conclusions are as follows:

(1) A novel approach for identifying gas cavitation in oil jet pumps is provided with comparison of vibration and high frequency noise under variable working conditions.
(2) In this study, the dissolved air content in lubrication oil $f_g = 110$ ppm and gas cavitation emerges in the range of $0.144 < h < 0.161$, with gas cavitation emerging at $\sigma = 1.68$ and fading away at $\sigma = 1.31$.
(3) The dissolved air content in lubrication oil is 6.3 times larger than that in water. Furthermore, the oil jet pump is more prone to suffer from cavitation than a water jet pump by 16 %.

7 ACKNOWLEDGEMENTS

This work was financially supported by the Fundamental Research Funds for the Central Universities (JZ2017HGBZ0946) and Major Scientific and Technological Projects in Anhui Province (JZ2017AKKZ1176).

8 NOMENCLATURES

D diameter, [m]
L length, [m]
F area, [m^2]
P pressure (gauge pressure), [MPa]
T time, [s]
Q flow rate, [m^{3}h^{-1}]
f_g mass fraction of dissolved air, [ppm]
σ cavitation number, [-]

subscripts
t throat,
o working oil flow,
s suction oil flow,
c outlet oil flow,
i dynamic parameter,
v lubrication oil vapour,
a beginning of throat pipe.

9 REFERENCES

[1] Lin, Q., Bao, Q., Li, K., Khonsari, M.M, Zhao, H. (2018). An investigation into the transient behavior of journal bearing with surface texture based on fluid-structure interaction approach. *Tribology International*, vol. 118, p. 246-255, **DOI:10.1016/j.triboint.2017.09.026**.

[2] Meng, F.M., Zhang, L., Long, T. (2016). Effect of groove textures on the performances of gaseous bubble in the lubricant of journal bearing. *Journal of Tribology*, vol. 139, no. 3, p. 31701, **DOI:10.1115/1.4034247**.

[3] Morgut, M., Jošt, D., Škerlavaj, A., Nobile, E., Contento, G. (2018). Numerical predictions of cavitating flow around a marine propeller and Kaplan turbine runner with calibrated cavitation models. *Strojniški vestnik - Journal of Mechanical Engineering*, vol. 64, no. 9, p. 543-555, **DOI:10.5545/sv-jme.2017.4647**.

[4] Garg, N, Pearce, B.W, Brandner, P.A, Phillips, A.W., Martins, J.R.R.A., Young, Y.L. (2019). Experimental investigation of a hydrofoil designed via hydrostructural optimization. *Journal of Fluids and Structures*, vol. 84, p. 243-262, **DOI:10.1016/j.jfluidstructs.2018.10.010**.

[5] Wu, Q., Huang, B., Wang, G., Cao, S. (2018). The transient characteristics of cloud cavitating flow over a flexible hydrofoil. *International Journal of Multiphase Flow*, vol. 99, p. 162-173, **DOI:10.1016/j.ijmultiphaseflow.2017.10.006**.

[6] Li, D., Kang, Y., Ding, X., Wang, X., Fang, Z. (2017). Effects of nozzle inner surface roughness on the performance of self-resonating cavitating waterjets under different ambient pressures. *Strojniški vestnik - Journal of Mechanical Engineering*, vol. 63, no. 2, p. 92-102, **DOI:10.5545/sv-jme.2016.3563**.

[7] Stepišnik Perdih, T., Širok, B., Dular, M. (2017). Influence of hydrodynamic cavitation on intensification of laundry aqueous detergent solution preparation. *Strojniški vestnik - Journal of Mechanical Engineering*, vol. 63, no. 2, p. 83-91, **DOI:10.5545/sv-jme.2016.3970**.

[8] Biluš, I., Bombek, G., Hočevar, M., Širok, B., Cenčič, T., Petkovšek, M. (2014). The experimental analysis of cavitating structure fluctuations and pressure pulsations in the cavitation station. *Strojniški vestnik – Journal of Mechanical Engineering*, vol. 60, no. 3, p. 147-157, **DOI:10.5545/sv-jme.2013.1462**.

[9] Concli, F. (2016). Pressure distribution in small hydrodynamic journal bearings considering cavitation: A numerical approach based on the open-source CFD code OpenFOAM®. *Lubrication Science*, vol. 28, no. 6, p. 329-347, **DOI:10.1002/ls.1334**.

[10] Chauhan, A., Singla, A., Panwar, N., Jindal, P. (2014). CFD based thermo-hydrodynamic analysis of circular journal bearing. *International Journal of Advanced Mechanical Engineering*, vol. 4, no. 5, p. 475-482.

[11] Zhang, X., Wang, D., Liao, R., Zhao, H., Shi, B. (2018). Study of mechanical choked Venturi nozzles used for liquid flow controlling. *Flow Measurement and Instrumentation*, vol. 65, p. 158-165, **DOI:10.1016/j.flowmeasinst.2018.12.001**.

[12] Singh, S., Choi, J.-K., Chahine, G.L. (2013). Characterization of cavitation fields from measured pressure signals of cavitating jets and ultrasonic horns. *Journal of Fluids Engineering*, vol. 135, no. 9, p. 91302, **DOI:10.1115/1.4024263**.

[13] Ding, C., Fan, Y.R. (2011). Measurement of diffusion coefficients of air in silicone oil and in hydraulic oil. *Chinese Journal of Chemical Engineering*, vol. 19, no. 2, p. 205-211, **DOI:10.1016/s1004-9541(11)60155-9**.

[14] Nüllig, M., Peters, F. (2018). Experiments on the mass transfer of gas bubbles in mineral oil. *Colloids and Surfaces A: Physicochemical and Engineering Aspects*, vol. 540, p. 81-89, **DOI:10.1016/j.colsurfa.2017.12.057**.

[15] Li, X.-S, Song, Y, Hao, Z.-R., Gu, C.-W. (2012). Cavitation mechanism of oil-film bearing and development of a new gaseous cavitation model based on air solubility. *Journal of Tribology*, vol. 134, no. 0317013, p. 31701-31707, **DOI:10.1115/1.4006702**.

[16] Zhou, J., Hu, J., Jing, C. (2016). Lumped parameter modelling of cavitating orifice flow in hydraulic systems. *Strojniški vestnik - Journal of Mechanical Engineering*, vol. 62, no. 6, p. 373-380, **DOI:10.5545/sv-jme.2015.3082**.

[17] Cunningham, R.G, Brown, F.B. (1970). Oil jet pump cavitation. *ASME Cavitation Forum*, Detroit.

[18] Long, X., Yao, H., Zhao, J. (2009). Investigation on mechanism of critical cavitating flow in liquid jet pumps under operating limits. *International Journal of Heat and Mass Transfer*, vol. 52, no. 9-10, p. 2415-2420, **DOI:10.1016/j.ijheatmasstransfer.2008.11.018**.

[19] Zhang, J., Mao, J.R., Wang, S.S., Zhang, J.J, Sun, P. (2015). Influence of noncondensible gas on flowing characteristics of multiple nozzle oil jet pump for lubrication system in steam turbine. *Proceedings of the Institution of Mechanical Engineers, Part A: Journal of Power and Energy*, vol. 229, no. 8, p. 876-888, **DOI:10.1177/0957650915593025**.

[20] Zou, J., Fu, X., Du, X.W., Ruan, X.D,, Ji. H., Ryu, S., Ochiai, M. (2008). Cavitation in a non-circular opening spool valve with U-grooves. *Proceedings of the Institution of Mechanical Engineers, Part A: Journal of Power and Energy*, vol. 222, no. 4, p. 413-420, **DOI:10.1243/09576509JPE489**.

[21] Duke, D.J., Kastengren, A.L., Swantek, A.B., Matusik, K.E., Powell, C.F. (2016). X-ray fluorescence measurements of dissolved gas and cavitation. *Experiments in Fluids*, vol. 57, no. 10, p. 162, **DOI:10.1007/s00348-016-2250-5**.

[22] Kim, S., Murrenhoff, H. (2012). Measurement of effective bulk modulus for hydraulic oil at low pressure. *Journal of Fluids Engineering*, vol. 134, no. 2, p. 021201, **DOI:10.1115/1.4005672**.

[23] Zhou, J., Wei, C., Hu, J. (2015). A novel approach for predicting thermal effects of gas cavitation in hydraulic circuits. *Energy*, vol. 83, p. 576-582, **DOI:10.1016/j.energy.2015.02.065**.

[24] Kunz, R.F., Boger, D.A., Stinebring, D.R., Chyczewski, T.S., Lindau, J.W., Gibeling, H.J., Venkateswaran, S., Govindan, T.R. (2000). A preconditioned Navier-Stokes method for two-phase flows with application to cavitation prediction. *Computers and Fluids*, vol. 29, no. 8, p. 849-875, **DOI:10.1016/S0045-7930(99)00039-0**.

[25] Sauer, J. (2000). *Instationaren Kaviterende Stromung-Ein neues Modell, basierend auf Front Capturing (VoF) and Blasendynamik*. PhD Thesis, University of Karlsruhe, Karlsruhe.

[26] Singhal, A.K., Athavale, M.M., Li, H.Y., Jiang, Y. (2002). Mathematical basis and validation of the full cavitation model. *Journal of Fluids Engineering*, vol. 124, no. 3, p. 617-624, **DOI:10.1115/1.1486223**.

[27] Prosperetti, A. (2017). Vapor bubbles. *Annual Review of Fluid Mechanics*, vol. 49, no. 1, p. 221-248, **DOI:10.1146/annurev-fluid-010816-060221**.

[28] Kratschun, F., Mielke, T., Schmitz, K. (2018). Water vapour cavitation in hydraulic fluids. *2018 Symposium on Fluid Power and Motion Control*, Bath, p. V001T01A038, **DOI:10.1115/FPMC2018-8872**.

[29] Krahl, D., Weber, J., Fuchs, M. (2016). Visualization of cavitation and investigation of cavitation erosion in a valve. *10th International Fluid Power Conference*, Dresden, p. 333-347.

[30] Zhang, J., Mao, J., Wang, S., Wu, B., Yuan, H., Wang, K., Zhang, J., Sun, P. (2014). Experimental study on the cavitation characteristics of an oil jet pump with multiple nozzles for the lubrication system in a steam turbine. *Journal of Engineering for Gas Turbines and Power*, vol. 136, no. 12, p. 122605, **DOI:10.1115/1.4027832**.

Strojniški vestnik - Journal of Mechanical Engineering 65(2019)2, 123-135

DOI:10.5545/sv-jme.2018.5487
Original Scientific Paper
Received for review: 2018-05-08
Received revised form: 2018-11-15
Accepted for publication: 2019-01-09

Fault Diagnosis Method Based on Modified Multiscale Entropy and Global Distance Evaluation for the Valve Fault of a Reciprocating Compressor

Ying Li – Jindong Wang* – Haiyang Zhao – Meiping Song – Lingfei Ou
Northeast Petroleum University, Mechanical Science and Engineering Institute, China

According to the nonlinearity, non-stationarity and multi-component coupling characteristics of reciprocating compressor vibration signals, a fault diagnosis method of a reciprocating compressor valve based on modified multiscale entropy (MMSE) and global distance evaluation (GDE) is proposed. First, the variational mode decomposition (VMD) method with superior anti-interference performance was utilized to analyse the strong non-stationarity vibration signals for all fault states. The modified multiscale entropy (MMSE) method provided for moving-average procedures by replacing mean-average coarse-grained procedures was developed for the vibration signals after de-noising, and then the GDE method of overall parameter selection was introduced to evaluate the extracted MMSE and to select the optimal sensitivity scale feature. Finally, a binary tree of support vector machine (BTSVM) was selected as the classifier to identify the reciprocating compressor valve fault type. By analysing the experimental data, it can be shown that the method can effectively identify the fault type of the reciprocating compressor valve.

Keywords: fault diagnosis, reciprocating compressor valve, modified multiscale entropy, global distance evaluation, binary tree of support vector machine

Highlights

- *An integrated fault feature extraction method of a reciprocating compressor valve based on the VMD-MMSE and GDE is proposed.*
- *A consistent number K of band-limited intrinsic mode functions (BLIMFs) were selected based on a novel criterion for all fault states*
- *The MMSE method provided for the moving-average procedure by replacing mean-average coarse-grained procedure was developed for the vibration signals, GDE was introduced to refine the eigenvectors for higher recognition efficiency and accuracy.*
- *The effectiveness of this method is verified by the recognition results of BTSVM in comparison to other feature extraction methods.*

0 INTRODUCTION

A reciprocating compressor is frequently used in the petroleum and petrochemical industries, its structure is complex, and multiple reasons for failure exist, of which more than 60 % occur in the valve. The ability to quickly and accurately find and diagnose the fault type for reciprocating compressor fault diagnosis is of great significance [1]. Due to the nonlinearity, non-stationarity, and multi-component coupling characteristics of reciprocating compressor valve vibration signals, using the traditional linear theory of signal analysis methods for fault diagnosis has more limitations, and it is difficult to effectively extract fault features. Consequently, these feature extraction methods based on nonlinear dynamic parameters, such as fractal dimension, approximate entropy [2], and sample entropy [3], are gradually being introduced to the field of fault diagnosis. These methods can describe the nonlinear characteristics of vibration signals from different perspectives, but merely reflect the characteristics of vibration signals from a single scale of information.

Multiscale entropy (MSE) is used by Costa et al. [4] and [5] and others to propose a nonlinear characteristics analysis method; it is a measurement method of the complexity and the random degree of time series under different scale factors. In the literature [6] to [8], the MSE method is used to quantify and extract the characteristics of vibration signals in the fault diagnosis of rolling bearings and gearboxes. The results show that MSE can describe the complexity of time series and effectively distinguish the types of faults. However, when different time scales are derived by calculating the coarse-grained time series, the length of the time series will be shortened as the scale factor increases, resulting in an imprecise estimation of entropy or undefined entropy when the scale factor is larger, and the endpoint “Flying wing” phenomenon occurs. Therefore, this paper proposes replacing the commonly used mean-average coarse-grained procedure with a moving-

*Corr. Author’s Address: Mechanical Science and Engineering Institute, Northeast Petroleum University, Daqing, China, wjd327@126.com

average coarse-grained procedure, which not only avoids the phenomenon of losing data after a coarse-grained procedure, but also greatly improves the accuracy of the algorithm.

Aiming at the nonlinearity, non-stationarity, and multi-component coupling characteristics of reciprocating compressor valve vibration signals, it is feasible to calculate the modified multiscale entropy (MMSE) for the characteristic state description of reciprocating compressor valve vibration signal. The vibration signal of a reciprocating compressor valve contains a large number of random noise components; however, they are susceptible to the influence of the noise signal; when simply calculating multiscale entropy to process the vibration signal of a reciprocating compressor valve, it will directly influence the outcome of feature extraction. Therefore, it is necessary to pre-process the original signal for reducing or eliminating the noise disturbance before a further analysis [9] to [11]. Zhao et al. [12] and [13] applied the improved local mean decomposition (LMD) to process the different bearing clearance fault states of a reciprocating compressor. Multi-scale morphological filtering (MMF) was put forward by Li et al. [14] to pre-process the vibration signals of planetary gearboxes before the fault extraction. Zhang et al. [15] and Bi et al. [16] utilized the empirical mode decomposition (EMD) and frequency modulated empirical mode decomposition (FM-EMD) to pre-process the vibration signals of a gearbox with different faults in diagnosing and monitoring the conditions of the gearbox. In addition, ensemble empirical mode decomposition (EEMD) and other methods were used to pre-process the vibration signals [17] and [18].

The variational mode decomposition (VMD) method [19] and [20] is an adaptive signal processing method, successfully utilized for extracting the fault features for nonlinear and non-stationary rub-impact signals [21] to [23], the instantaneous detection of speech signals [24] and trends analysis of financial markets [25]. Therefore, a feature extraction algorithm in combination with VMD and MMSE can improve the accuracy of feature extraction.

For the MMSE eigenvalues, when the fault type and data are larger, the classification sensitivity and classification level of MMSE corresponding to the characteristics of different scales are different; if only to the MMSE eigenvalues are used to identify the fault type, the failure classification accuracy and precision are relatively low, it is necessary to optimize the MMSE eigenvalues. Therefore, a novel global distance evaluation (GDE) method is proposed to solve the problem of the optimal parameters.

This paper combines the VMD-MMSE with the GDE algorithm, and proposes a fault feature extraction method based on the VMD-MMSE and GDE. The method was applied to the fault feature extraction of reciprocating compressor valve vibration signals, used to analyse different forms of valve failure, and a binary tree of support vector machine (BTSVM) was applied to different fault classification of valve fault, which provided a new method of fault diagnosis for a reciprocating compressor valve.

1 MMSE AND GDE PRINCIPLES

1.1 Multiscale Entropy

Sample entropy is the complexity and lack of rules of time series on a single scale. When sample entropy is gradually reduced, the similarity of the time series increases. When sample entropy increases gradually, the complexity of the time series will be higher. For multiscale entropy, it is on the basis of sample entropy; therefore, multiscale entropy shows the sample entropy of time series under different scales, reflecting the degree of complexity of the time series in different scales with the sequence indicated in multiple scales containing more information [6]. Therefore, in the analysis of multiscale entropy, measuring the complexity of time series should be chosen by sample entropy for analysis. The calculation process of multiscale entropy is as follows:

(1) To obtain the coarse-grained original time series, and construct time series at different time scales. The coarse-grained time series is $\left\{q_j^{(\tau)}\right\}$, calculated according to the following formula:

$$q_j^{(\tau)}=\frac{1}{\tau}\sum_{i=(j-1)\tau+1}^{j\tau} q_i, \quad (1\leq j\leq N/\tau,\ \tau=1,2,...,N). \quad (1)$$

(2) The time series is $\{x(i),\ i=1,2,...,N\}$, calculated its SampEn and selected model dimension for m, similar tolerance for r, computing as follows [6]:

(a) Set time series to a set of m dimensional vector:

$$X(i)=\{x(i),\ x(i+1),\ ...,\ x(i+m-1),\\ (i=1,2,...,N-m+1). \quad (2)$$

(b) The definition of the distance between $X(i)$ and $X(j)$ is $d[X(i),X(j)]$, which is one of the biggest in the corresponding element, namely

$$d\left[X(i),X(j)\right]=\underset{k=0\rightarrow m-1}{Max}\left\{\left|X(i+k)-X(j+k)\right|\right\}. \quad (3)$$

(c) For i, statistics the number of $d[X(i),X(j)]<r$ is n_i^m, $i=1,2,...,N-m+1$, $j=1,2,...,N-m+1$, and $j\neq i$, then calculate the ratio of it and the total distance $N-m$ (template matching number), and namely:

$$C_i^m(r)=\frac{n_i^m}{N-m},\tag{4}$$

while the mean of $C_i^m(r)$ is:

$$C^m(r)=\frac{1}{N-m+1}\sum_{i=1}^{N-m+1}C_i^m(r).\tag{5}$$

(d) When $m=m+1$, repeat steps (a) to (c), statistics $C^{m+1}(r)$.

(e) Calculation formula of the final *SampEn* is

$$SampEn=-\ln\frac{C^{m+1}(r)}{C^m(r)}.\tag{6}$$

With the calculation formula of sample entropy, it can be seen that the size of the sample entropy depends on m, r, usually $m\in[2,10]$, $r\in[0.1,0.5]SD$.

(3) Multiscale entropy is the function of the scale factor τ as independent variables, *SampEn* as dependent variable.

$$MSE(\tau)=SampEn(X(\tau),m,r).\tag{7}$$

1.2 Modified Multiscale Entropy

The traditional coarse-grained method is to compress the original time series by the scale factor τ in turn. Since the original time series is a finite amount of data, as the scale factor τ gradually increases, the length of the coarse-grained time series decreases. While the original data length is not an integer multiple of the scale factor τ, it will result in the loss of partial data, and the emergence of the "flying wing" phenomenon, affecting the accuracy of subsequent algorithms. Therefore, a coarse-grained method based on the sliding average method is proposed for the coarse-grained original time series, which not only avoids the phenomenon of data loss after the coarse-grained series but also greatly improves the accuracy of the algorithm.

(1) The proposed MMSE method is as follows: Let $P_j^{(\tau)}$ represent the moving-averaged time series at a scale factor τ, calculated according to the following formula:

$$p_j^{(\tau)}=\frac{1}{\tau}\sum_{i=j}^{j+\tau-1}x_i,\ (1\leq j\leq N-\tau+1).\tag{8}$$

(2) The modified multiscale entropy of the time series after calculating the average coarse-grained time series is calculated:

$$MMSE(\tau)=SampEn(p^{(\tau)},m,r).\tag{9}$$

1.3 Comparison between MMSE and MSE Simulation

1.3.1 Simulation Signal Analysis

In order to compare the MMSE and the MSE, respectively for different lengths of $1/f$ noise and Gaussian white noise signals are analysed, both the time domain waveform are shown in Fig. 1.

Using MSE and MMSE to analyse length N = 2048, 4096, 6144, 8192 and 10240 of $1/f$ noise and Gaussian white noise signals, respectively, shown in Fig. 2, which m = 2, r = 0.15SD.

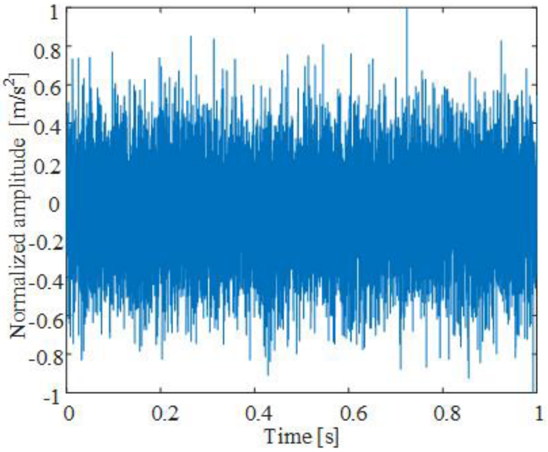

a)

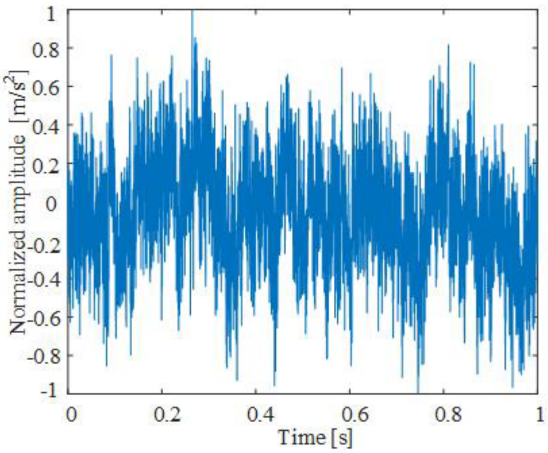

b)

Fig. 1. Gaussian white noise signal and $1/f$ noise signal waveform; *a) Gaussian white noise signal, b) $1/f$ noise signal*

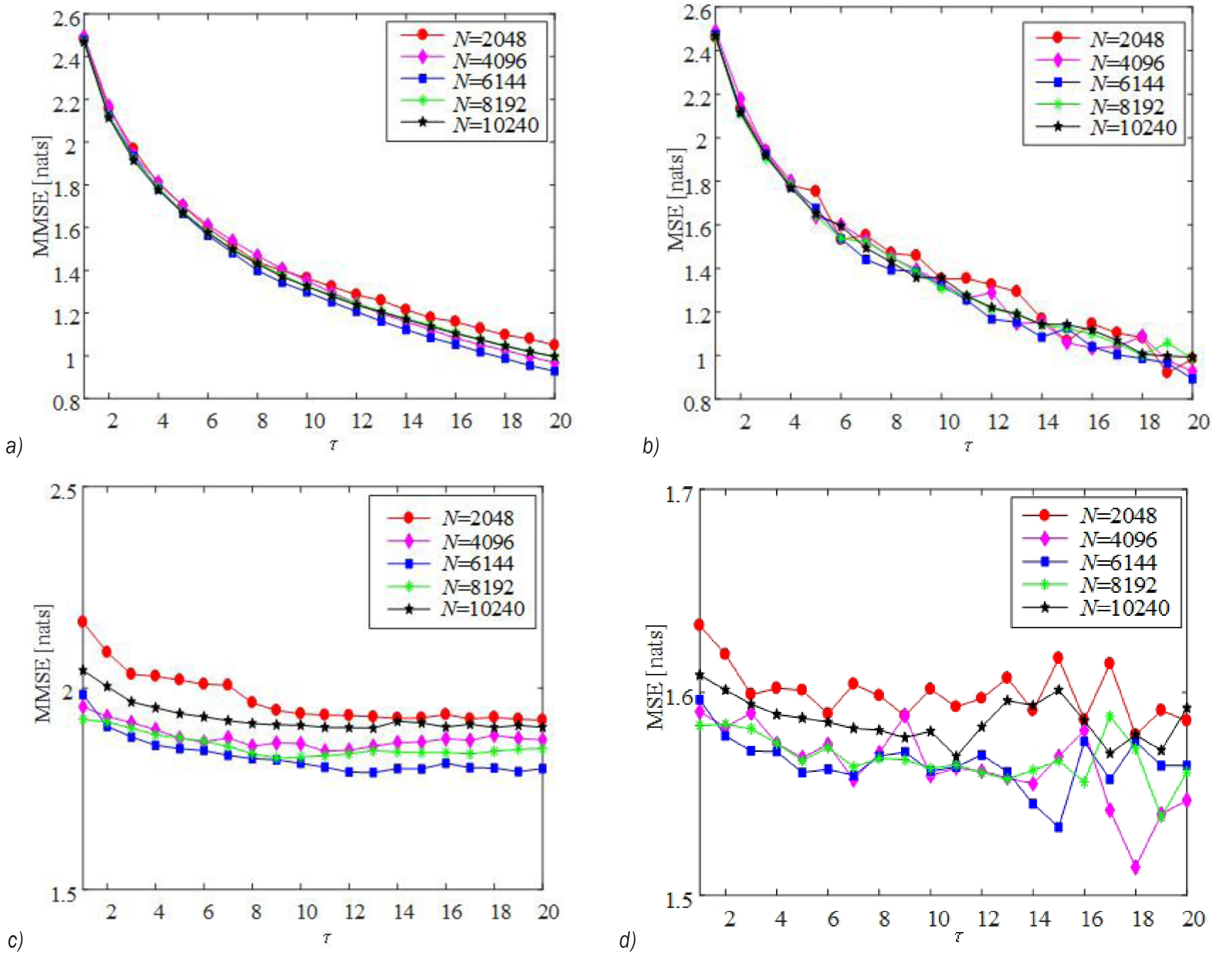

Fig. 2. *MMSE and MSE curves of different lengths of white noise and 1/f noise; a) MMSE with different lengths of white noise, b) MSE with different lengths of white noise, c) MMSE with different lengths of 1/f noise, d) MSE with different lengths of 1/f noise*

As can be seen from Fig. 2, firstly as the scale factor τ increases, the MSE and MMSE curves of white noise gradually decrease, the MSE and MMSE curves of $1/f$ noise tend to be constant, but the MSE curves of white noise and $1/f$ noise increase with the scale factor τ, specifically on a larger scale; the entropy fluctuation range is relatively large, while the MMSE curve changes more gradually with the increase of the scale factor. This shows that as the scale factor τ increases, the MMSE has a better consistency than the MSE to obtain a stable entropy value; secondly, when the data length N is greater than 2048, the MSE or the MMSE curves of different lengths of data have only a slight difference. Furthermore, the MMSE (or MSE) curve of the white noise decreases as the scale factor increases, indicating that the white noise signal contains important feature information only in the coarse-grained sequence with smaller scale; whereas the MMSE (or MSE) of the $1/f$ noise is small with a large change in the scale factor, and it tends to be almost stationary, and the entropy of the $1/f$ noise is greater than the entropy of the white noise in most scales. This shows that $1/f$ noise contains rich feature information and has more complex structural characteristics than white noise signals do.

To study the statistical stability effects of the MSE and the MMSE, the MSE and the MMSE analysis was performed on white noise and $1/f$ noise signals, and 200 groups of independent noise data were randomly generated. Each group of data contained 1000 data points. The simulation results are shown in Fig. 3.

For the white noise shown in Fig. 3a, the mean values of the entropy calculated using the MSE and the MMSE are almost equal, but the standard deviation of MMSE is much smaller than the standard deviation of MSE, which shows that the MSE and

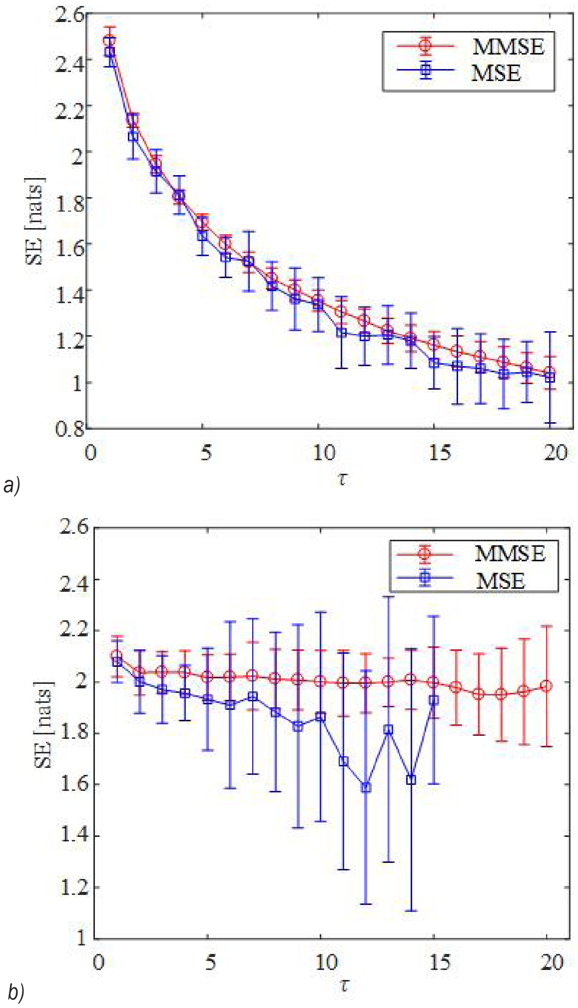

Fig. 3. *Comparative analysis of the MMSE and the MSE; a) white noise signal, b) 1/f noise signal*

the MMSE methods are almost statistically stable. However, the MMSE method provides more accurate entropy estimation than the MSE method does. For the 1/*f* noise shown in Fig. 3b, the MSE method causes undefined entropy when the coarse-grained scale is greater than 16, and the MMSE method calculates the entropy value for all coarse-grained scales. By comparing it with the MSE method, it can be seen that the proposed MMSE method is more effective in extracting different structural characteristics of white noise and 1/*f* noise and providing more accurate entropy estimation.

1.3.2 Valve Analog Signal Analysis

For the four states of the valve, 20 groups of two-whole-period data were selected, and the analysis methods in Section 1.3.1 were adopted to conduct MSE and MMSE analysis respectively, in which m = 2, r = 0.15SD. The results are shown in Figs. 4 and 5. As can be seen from Fig. 4, as the scale factor τ increases, most of the MSE and MMSE curves of the four reciprocating compressor valve states gradually decrease, but only $\tau \leq 3$, the MSE and MMSE curves increase. The larger the entropy values, the more stable the curves are. However, the MSE curves of the four reciprocating compressor valve states increase with the scale factor τ; specifically on a larger scale, the entropy fluctuation range is relatively large, while the MMSE curve changes more gradually with the increase of the scale factor. It also turns out that the MMSE has a better consistency than the MSE to obtain a stable entropy value as the scale factor τ increases.

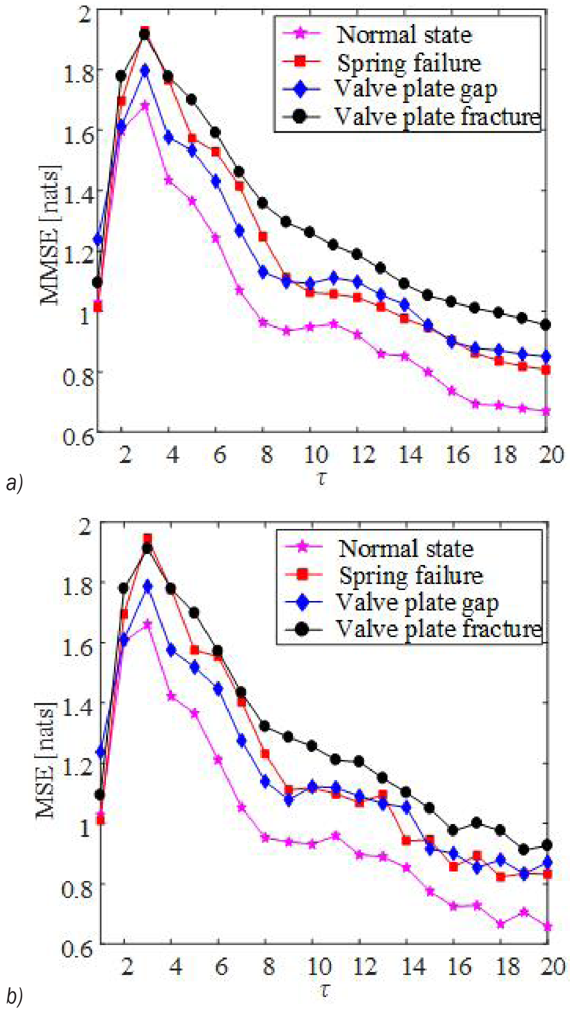

Fig. 4. *MMSE and MSE curves of different valve states; a) MMSE with different valve states, b) MSE with different valve states*

Similarly to studying the statistical stability effects of the MSE and the MMSE for the four reciprocating compressor valve states, the MSE and the MMSE analysis was performed on 20 groups of the four valve states data were randomly generated. Each group of data contained two whole-period data points. The calculation results are shown in Fig. 5.

For the four valve states shown in Fig. 5, the mean values of the entropy calculated using the MSE and the MMSE are almost equal, but the individual values of the MSE and the MMSE is discrepant; in particular, the larger the scale τ, the greater the discrepancy and obvious fluctuation. Furthermore, the standard deviation of MMSE is much smaller than the standard deviation of MSE, which shows that the MSE and the MMSE methods are almost statistically stable. However, the MMSE method provides more accurate entropy estimation than the MSE method does. It can be seen that the proposed MMSE method is more effective in extracting the different structural characteristics of the four valve states and providing more accurate entropy estimation.

1.4 Global Distance Evaluation Method

According to the vibration signals under different conditions, extracting their MMSE eigenvalues, of which the vibration signal under different conditions and different scales as a feature vector, yields original MMSE feature set T, namely:

$$\{T \mid MMSE(l,m,n)\},$$
$$l=1,2,...,L;\ m=1,2,...,M;\ n=1,2,...,N, \tag{10}$$

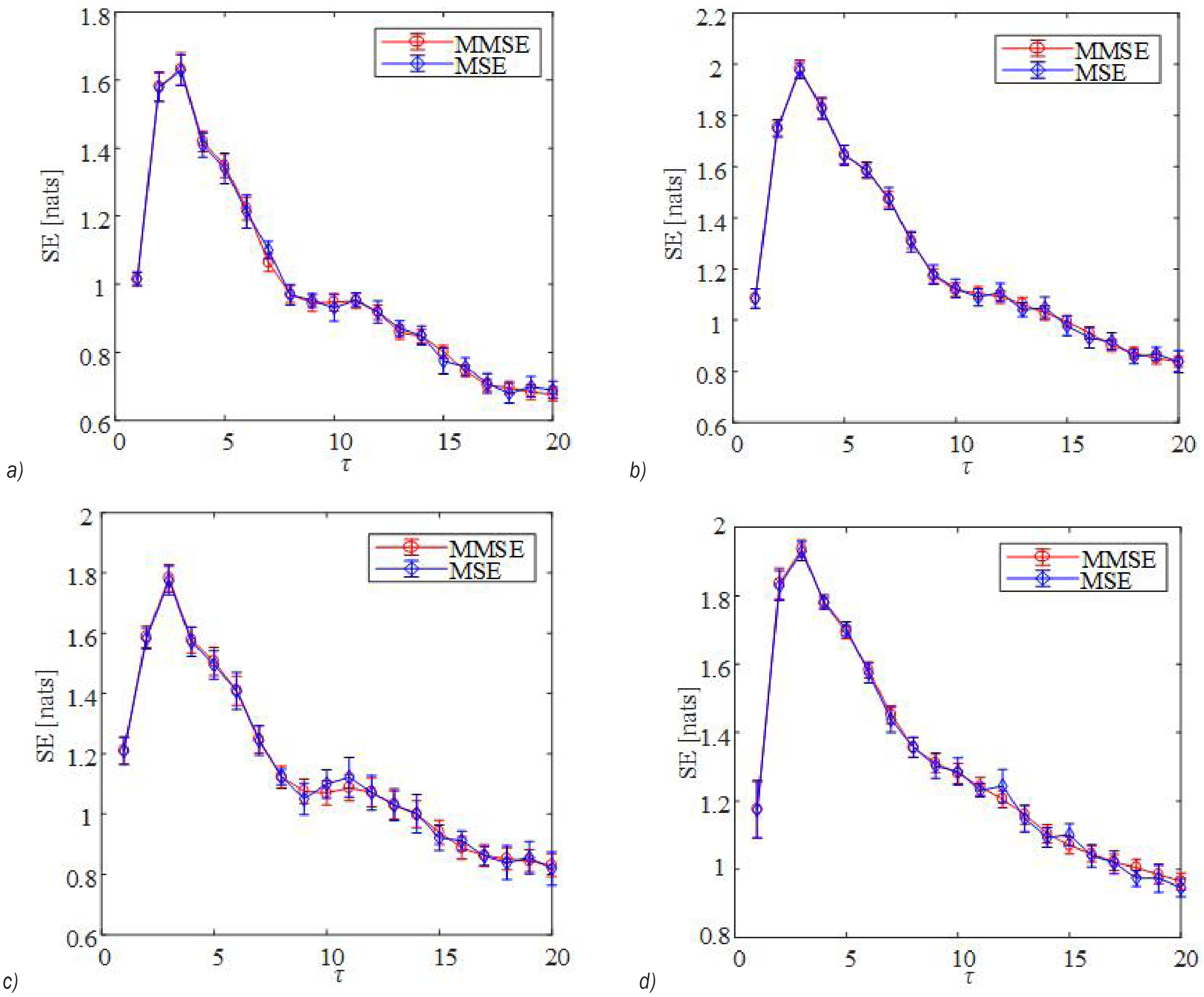

Fig. 5. *Comparative analysis of the MMSE and the MSE for the four reciprocating compressor valve states; a) normal state, b) spring failure, c) valve plate gap, d) valve plate fracture*

where $MMSE(l, m, n)$ denotes the sample entropy feature of l^{th} scale of m-category under n^{th} sample; l is number of scale; M is the state class number; N is a sample number.

The MMSE feature set T contains a larger amount scale of the feature vector, generally not less than 10. Under different conditions and different scales, fault feature vector set T reflects the sensitivity of different degree, and redundancy between them still exists. To improve the classification performance and efficiency of feature vector set T, this paper introduced the global distance evaluation technique to MMSE original feature set T of Eq. (10) for optimal selection feature, specific steps are as follows:

(1) The average distance within the class of similar state samples

$$d_{l,m} = \frac{1}{N(N-1)} \sum_{m,n=1}^{N} \left| MSE(l,m,n) - MSE(l,m,q) \right|,$$

$$n, q = 1, 2, ..., N;\ q \neq n,\ m = 1, 2, ..., M;\ l = 1, 2, ..., L. \quad (11)$$

Among, $MMSE(l,m,n)$, $MMSE(l,m,z)$ respectively denotes entropy value of n^{th} sample and z^{th} sample under I^{th} scale of m-category. Therefore, the average distance class under the same scale I of m classes is:

$$D_l = \frac{1}{M} \sum_{m=1}^{M} d_{l,m}. \quad (12)$$

(2) The average distance between different class states

$$D_l' = \frac{1}{M(M-1)} \sum_{u,v=1}^{M} \left| MSE'(l,u) - MSE'(l,v) \right|. \quad (13)$$

Among, $MMSE'(l,u)$, $MMSE'(l,v)$ denotes the average value of m samples entropy under l^{th} scale of u^{th} and v^{th} class.

Define sensitivity

$$\varphi_l = D_l' / D_l. \quad (14)$$

φ_l described the l^{th} scale feature of sensitivity of classifying M class, φ_l is larger, the more sensitive features, more easily classified.

(3) Determine the restrictive conditions, namely

$$|\varphi_{mean}/\varphi_{mean}| > th, \quad (15)$$

among, φ_{mean} for average sensitivity; th for the threshold.

The scale features above conditions are selected as the sensitive features. Constitute the sensitive feature subset $T1$, and send it to BTSVM for the classification comparison.

2 FAULT DIAGNOSIS METHOD BASED ON MMSE AND GDE

A novel feature extraction method based on the MMSE and GDE is proposed, and its application for reciprocating compressor valve fault diagnosis is described in Fig. 6. The method decomposes vibration signal by VMD, and then chooses a series of band-limited intrinsic mode functions (BLIMF) components including the main components of the fault information to reconstruct signal, quantitatively described by MMSE and GDE, and finally adopts BTSVM to identify fault type. The specific steps are as follows:

(1) For the vibration signals of different fault states, we employ the VMD method to decompose each signal into K number of BLIMFs, and select adaptively a uniform K number BLIMFs of VMD decomposition for all fault states.
Initialization modal number $K=2$, penalty factor and bandwidth values are $\sigma=0$, $\alpha=2000$, respectively. Observing the central frequency of each BLIMF component after decomposition, if the central frequencies are similar, the modal number $K=K-1$ is determined, whereas the modal number $K=K+1$, repeated the above process until the centre frequency is similar. Calculate the relationship between each BLIMF component and the vibration signal, and determine the BLIMF components with the main information, and reconstruct the signal.
(2) Calculate the MMSE of each type of the reconstruction signal, and form a feature set of MMSE.
(3) Using the GDE method to select the feature optimization of MMSE feature set, obtain the sensitive feature set of MMSE.
(4) With BTSVM as a pattern recognition classifier, send the sensitive feature set of MMSE to BTSVM for the classification comparison and identify fault type.

3 FAULT DIAGNOSIS FOR RECIPROCATING COMPRESSOR VALVE BASED ON MMSE AND GDE METHOD

In this study, the proposed MMSE and GDE method is utilized to extract the fault feature of the valve vibration data from a two-stage double-acting reciprocating compressor of type (2D12), as shown in Fig. 7. The shaft power of reciprocating compressor is 500 kW, the piston stroke is 240 mm, and the motor speed is 496 rpm. The valve is one of the core components of the reciprocating compressor; its safe and stable operation is of great significance.

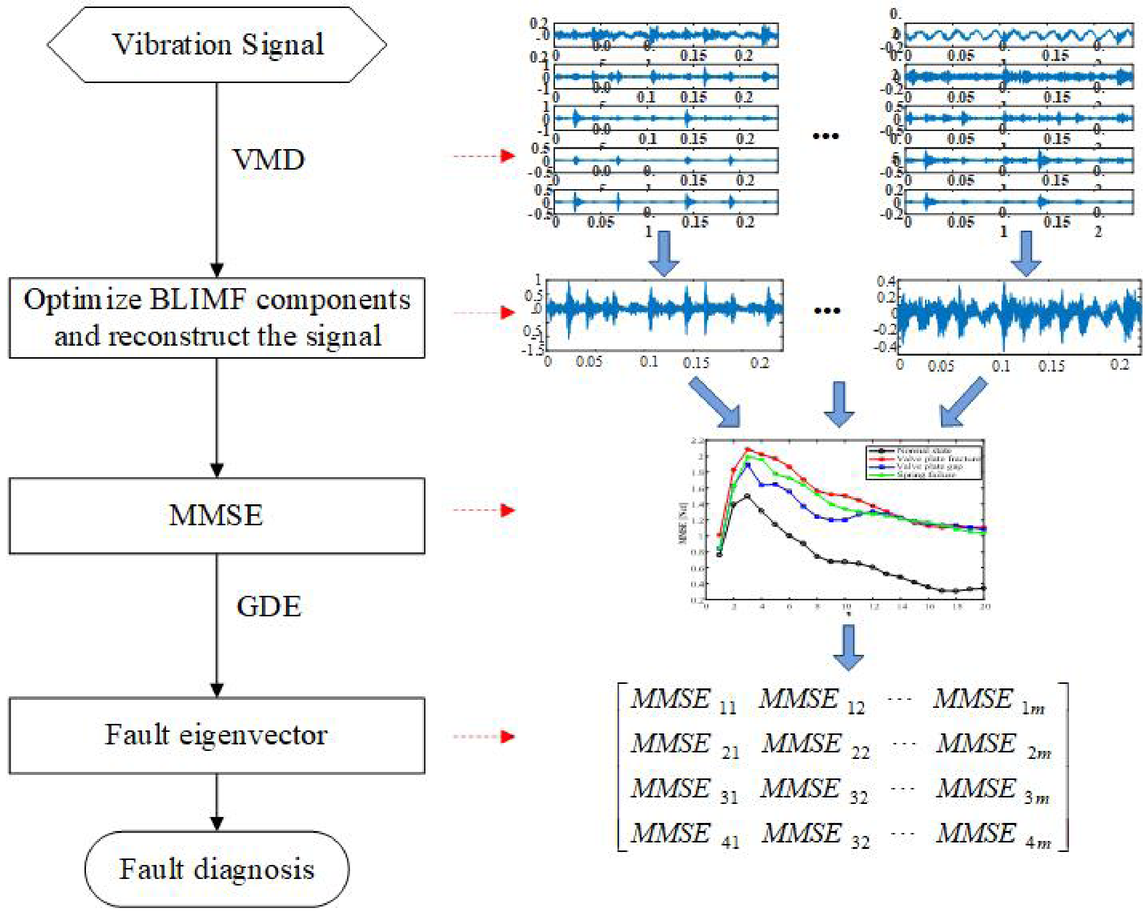

Fig. 6. *Flowchart of fault diagnosis algorithm based on MMSE and GDE*

The 2D12 reciprocating compressor valve is a ring valve that is composed of a valve seat, a valve plate, a valve lift limiter, a spring, a screw, and a nut. Due to the long-term effect of the alternating load, the valve with periodic reciprocating motion is more prone to a failure. This paper mainly investigates three kinds of reciprocating compressor valve failures: spring failure, valve plate fracture, and valve plate gap. When the reciprocating compressor valve is abnormal, the performance of the vibration signal in the valve cover side direction will undergo a substantial change. Therefore, this paper extracted valve cover vibration signals as the analysis data.

A vibration-based measurement and analysis technique is an effective measure to monitor and diagnose fault states of machinery due to the abundant operational state information embodied in vibration signals. An experiment on valve failures states for the secondary valve was conducted in real working conditions. Three valve failures states (spring failure, valve plate fracture, and valve plate gap) corresponding to one less spring, the middle valve piece breaks, and a gap on the second and third rings of the outer ring number states simulated with the secondary valve cover side, were tested respectively using a Hubei UT3416 data acquisition instrument and integrated circuit piezoelectric (ICP) acceleration sensors placed on the top of valve surface to collect vibration signals. The position of sensor was marked with a red square in Fig. 7a, and the sample frequency is 5 kHz. The vibration signal collected by MATLAB software written programs was analysed. The vibration signals of four primary valve states are shown in Fig. 8 for two periods.

In this paper, the VMD method was employed to decompose the vibration signal of the reciprocating compressor valve faults; the parameters of the VMD method need to be determined, so the default mode number $K=2$ and the bandwidth parameter $\alpha=2000$. In theory, the centre frequency of each

BLIMF component after the VMD decomposition is distributed from low frequency to high frequency; when the K value is optimized, the difference between the centre frequency of the K^{th} BLIMF component and the centre frequency of the $(K–1)^{th}$ BLIMF component is the biggest. Therefore, the best mode number K value is confirmed using the method of the centre frequency difference maximum. The vibration signals of reciprocating compressor valves are analysed to determine the modal number K value. The vibration signal of valve fracture failure as an example specifically, when K takes different values, the centre frequency of several BLIMF components obtained by the VMD decomposition is shown in Table 1.

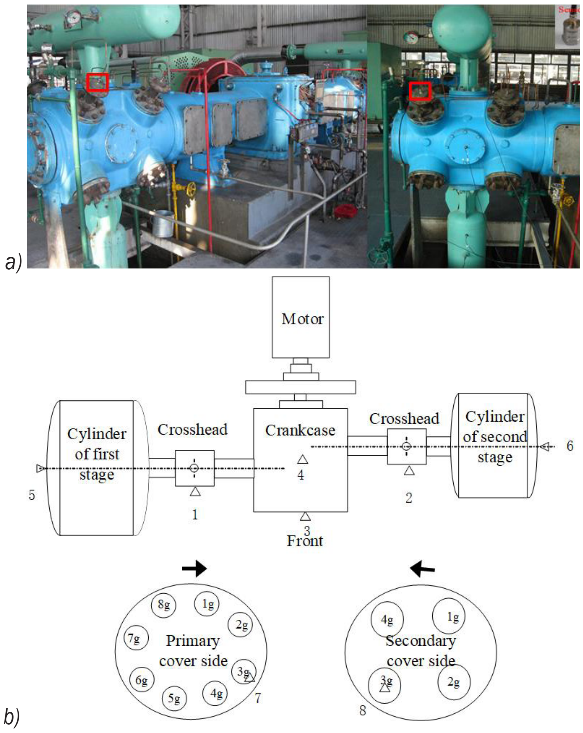

Fig. 7. *Two-stage double-acting reciprocating compressor of 2D12 type; a) test bench of reciprocating compressor, b) structural drawing of reciprocating compressor*

As can be seen from Table 1, when $K=4$, the difference between the centre frequency of the fourth BLIMF component and the centre frequency of the third BLIMF component is 15953.9 Hz; when $K \geq 5$, the difference between the centre frequency of the K^{th} BLIMF component and the centre frequency of the $(K–1)^{th}$ BLIMF component is less than 15953.9 Hz. Therefore, it is considered that when $K=4$, the best value can be obtained. This method is applied to the vibration signals of the four valve fault states, and the VMD parameters of the vibration signals of the four valve fault states can be obtained, as shown in Table 2.

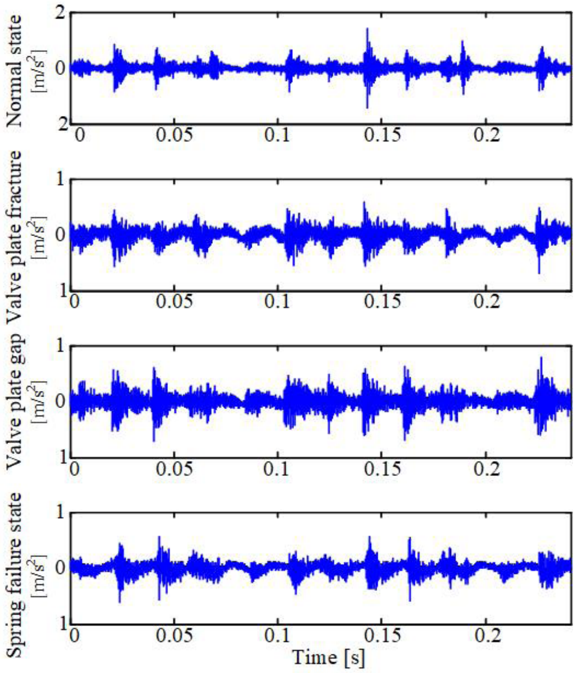

Fig. 8. *Vibration acceleration in four reciprocating compressor valve states*

Using the VMD parameters in Table 2, the vibration signals of four valve fault states were decomposed by the VMD, then cross correlation coefficient of each BLIMF component in different valve states is respectively calculated in Table 3. A reasonable threshold is given and the BLIMF component with the main state information is determined to reconstruct signal of each state. The cross-correlation coefficient of the first three BLIMF components of the normal state, valve plate fracture, and valve plate gap is greater than 0.3, and the cross correlation coefficient of the first four BLIMF components of spring failure is greater than 0.4. Therefore, in this paper, the first three BLIMF components of normal state, valve plate fracture, and valve plate gap, and the first four BLIMF components of spring failure were selected for signal reconstruction.

The MMSE values of the reconstruction vibration signals in different valve states were calculated, for which the mode dimension $m=2$, the similar tolerance $r=0.25$SD, the maximum scale factor $\tau_{max}=20$. As shown in Figs. 9 and 10, the MMSE values graphs are the same length of time within the scope of each fault vibration signal. In Figs. 9 and 10, the MMSE values

Table 1. *Center frequency of each BLIMF component of the vibration signal*

	BLIMF1	BLIMF2	BLIMF3	BLIMF4	BLIMF5	BLIMF6	BLIMF7
K = 2	6133.8	11668.3					
K = 3	453.9	5865.5	8561.9				
K = 4	388.5	5510.8	7830.2	23784.1			
K = 5	307.8	5080.2	6628.6	8766.1	19442.7		
K = 6	163.6	2979.6	5328.9	6658.4	8787.5	23046.0	
K = 7	163.1	2977.5	5327.6	6654.3	8762.9	20278.8	23073.1

of each fault vibration signal decrease progressively with the increasing of scale factor from τ=3, which indicates that the complexity of valve fault vibration signal is decreasing. The MMSE values of the normal state, valve plates fracture, valve plate gap and valve spring failure are represented by MMSE1, MMSE2, MMSE3 and MMSE4, respectively; in general, their size order is MMSE2>MMSE4>MMSE3>MMSE1. However, the MMSE values of the latter part of Fig. 9 and the front part of Fig. 10 appear as overlapping phenomenon. If the calculated MMSE values are directly input into the BTSVM, the accuracy of the fault classification is relatively low. Therefore, the MMSE values need to be further optimized before being input into the BTSVM. The GDE method proposed in this article was used to perform the feature optimization, the assessment curve as shown in Fig. 11.

The sensitivity on the different scales are different, and the larger the scale factor, the lower sensitivity in Fig. 11, so set the threshold condition of th>1.00. According to the definition of conditions, MMSE values of scale factor τ between 3 and 10 should be selected as a sensitive feature vector subset.

Table 2. *VMD parameters of the vibration signals of the four valve fault states*

Valve states	Modal number K	Bandwidth parameter α
Normal state	4	2000
Valve plate fracture	4	2000
Valve plate gap	4	2000
Spring failure	5	2000

Further evaluation is needed to assess the effectiveness of the proposed method based on the MMSE and GDE method, and this paper introduces the binary tree support vector machine (BTSVM) method **[26]** to **[28]** to evaluate four valve fault eigenvectors. To test this, 150 eigenvector samples were selected from each valve fault, and 100 were taken as training samples, other 50 as test samples. For the BTSVM, the radial basis kernel function was employed, and the kernel parameter γ=3.52 and error penalty parameter C=1.79 were optimized with the genetic algorithm; the results are shown in Table 4.

Table 3. *Cross correlation coefficient of each BLIMF component in different valve states*

Valve states	Cross correlation coefficient of each BLIMF component				
	BLIMF1	BLIMF2	BLIMF3	BLIMF4	BLIMF5
Normal state	0.3205	0.7559	0.6192	0.2048	
Valve plate fracture	0.5808	0.7328	0.5645	0.0790	
Valve plate gap	0.4484	0.8423	0.5185	0.1496	
Spring failure	0.4928	0.4939	0.7030	0.4935	0.0854

To compare the superiority of this fault recognition method, the same number of training and test samples was extracted by other three methods, including the VMD-MMSE and principal component analysis (PCA), the MMSE and GDE, and the VMD-MMSE, and then recognized using the BTSVM. The recognition results are also listed in Table 4.

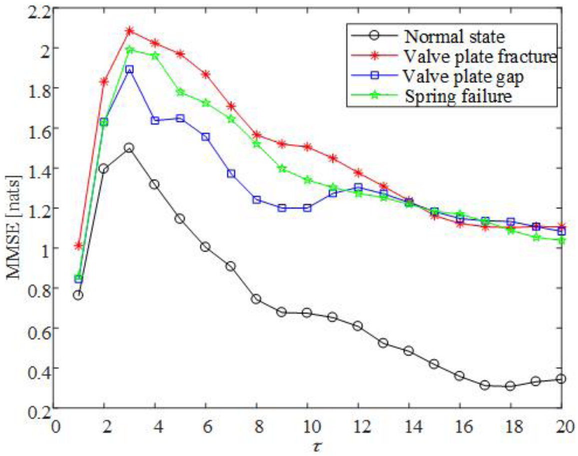

Fig. 9. *First MMSE values graphs of the reconstruction vibration signals in different valve states*

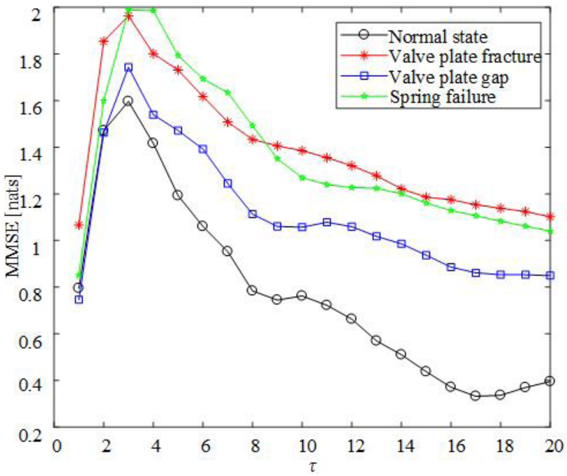

Fig. 10. *Second MMSE values graphs of the reconstruction vibration signals in different valve states*

Table 4. *Recognition accuracy of comparison between different methods*

Feature extraction method	Recognition accuracy [%] of valve states				Total accuracy [%]
	Normal state	Spring failure	Valve plate fracture	Valve plate gap	
VMD-MMSE and GDE method	100	98	100	100	99.5
VMD-MMSE and PCA	98	98	98	98	98
MMSE and GDE method	92	90	92	92	91.5
VMD-MMSE	90	86	86	88	87.5

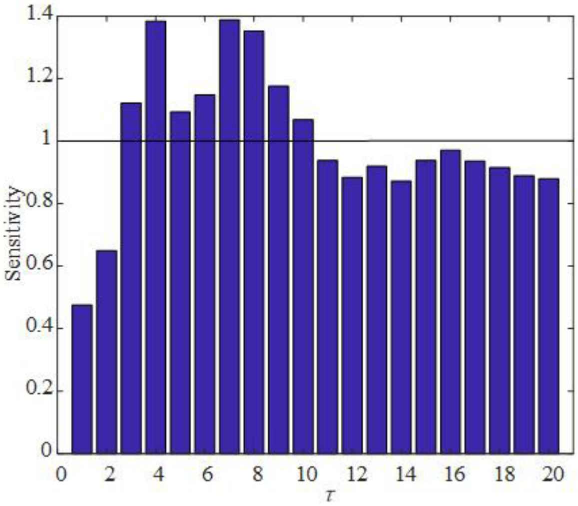

Fig. 11. *Assessment curve of reciprocating compressor valve fault*

The results show that the accuracy in each state and the total accuracy of the proposed method are better than those of three other feature extraction methods under the condition of the same finite number of samples. From Table 4, we can clearly see that, by comparing the identification results of three methods, the feature vectors extracted by the VMD-MMSE and GDE and the VMD-MMSE and PCA are better than those achieved by the MMSE and GDE from the result of recognition rate, so it is necessary to combine the self-decomposition method with the MMSE for resisting noise interference and highlighted information extraction. Furthermore, we also see that the fault recognition rates of the MMSE without the GDE are lower than those of the proposed method, so it validates the necessity of using the GDE in this method. Through the comparative research above, the proposed method is the superior fault recognition method to diagnosis faults of reciprocating compressor valve effectively and accurately.

4 CONCLUSION

To satisfy the needs of reciprocating compressor valve fault recognition, from the perspective of fault feature extraction and optimal selection, this paper presents a novel fault diagnosis method based on the modified multiscale entropy and global distance evaluation, and it is applied for fault diagnosis of reciprocating compressor valve faults.

(1) In the proposed method, the VMD method was employed to eliminate the noise interference, which outperforms the traditional time frequency analysis method such as the EMD and Wavelet packet for the reciprocating compressor vibration signals.
(2) After the vibration signal is reconstructed by the VMD method, a novel MMSE method provided with moving-average procedure by replacing mean-average coarse-grained procedure was developed for the vibration signals, which overcomes the obstacle of the conventional MSE yielding undefined entropy or an imprecise estimation of entropy by the large scale factor.
(3) For the appearance of the MMSE eigenvalues overlapping phenomenon, the GDE method was employed to refine the final eigenvector, and it indeed has a higher recognition efficiency and accuracy.
(4) This method was applied for the fault diagnosis of a reciprocating compressor at different valve states, and it demonstrates superior recognition results through the comparison with other feature extraction methods.

In this paper, the VMD method was used to denoise the vibration signal, the research on the pre-set decomposition scale has made some progress, and the modal-aliasing phenomenon is suppressed to some extent, but the method of selecting parameters is not adaptive. To understand how to suppress noise more effectively and adaptively suppress modal aliasing, further research is needed.

5 ACKNOWLEDGEMENTS

This work was partly supported by the General Financial Grant from the China Postdoctoral Science Foundation (2015M581423), Natural Science Foundation of Heilongjiang Province in China (E2015037, E2016009), and Supported by Northeast Petroleum University Innovation Foundation For Postgraduate (YJSCX2017-020NEPU).

6 NOMENCLATURES

K	initialization modal number, [-]
σ	penalty factor, [-]
α	bandwidth value, [Hz]
$\left\{q_j^{(\tau)}\right\}$	the coarse-grained time series, [-]
N	length of time series, [-]
τ	time scale factor, [-]
m	mode dimension, [-]
r	similar tolerance , [-]
C^m	template matching number, [-]
$SampEn$	sample entropy, [nats]
$P_j^{(\tau)}$	the moving-averaged time series at a scale factor τ, [-]
T	original MMSE feature set, [-]
$MMSE(l,m,n)$	sample entropy feature of l^{th} scale of m-category under n^{th} sample, [nats]
$MMSE(l,m,z)$	sample entropy feature of l^{th} scale of m-category under z^{th} sample, [nats]
L	number of scale, [-]
M	number of state class, [-]
N	number of sample, [-]
$d_{l,m}$	average distance within the class of similar state samples, [-]
D_l	average distance class under the same scale I of m classes, [-]
D'_l	average distance between different class states, [-]
$MMSE'(l,u)$	average value of m samples entropy under l^{th} scale of u^{th} class, [nats]
$MMSE'(l,v)$	average value of m samples entropy under l^{th} scale of vth class, [nats]
φ_l	the l^{th} scale feature of sensitivity of classifying M class, [-]
φ_{mean}	average sensitivity, [-]
th	the threshold, [-]
$\tau_{\max}$	the maximum scale factor, [-]
γ	kernel parameter, [-]
C	error penalty parameter, [-]

7 REFERENCES

[1] Jin, G., Yang, S. (1991). *Compressor Reliability*. Mechanical Industry Press, Beijing. (in Chinese)

[2] Pincus, S.M. (1991) Approximate entropy as a measure of system complexity. *Proceedings of the National Academy of Sciences*, vol. 88, no. 6, p. 2297-2301, **DOI:10.1073/pnas.88.6.2297**.

[3] Richman, J.S., Moorman, J.R. (2000). Physiological time-series analysis using approximate entropy and sample entropy. *American Journal of Physiology Heart Circulatory Physiology*, vol. 278, no. 6, p. 2039-2049, **DOI:10.1152/ajpheart.2000.278.6.H2039**.

[4] Costa, M., Goldberger, A.L., Peng, C.-K. (2005). Multiscale entropy analysis of biological signals. *Physical Review E*, vol. 71, no. 2, p. 1-18, **DOI:10.1103/PhysRevE.71.021906**.

[5] Costa, M., Goldberger, A.L., Peng, C.-K. (2002) Multiscale entropy analysis of complex physiologic time series. *Physical Review Letters*, vol. 89, no. 6, p. 1-18, **DOI:10.1103/PhysRevLett.89.068102**.

[6] Qi, Z., Xu, Z., Lu, Z. (2008). Application of approximate entropy in engine fault diagnosis. *Journal of Ordnance Engineering College*, vol. 20, no. 2, p. 39-42. (in Chinese)

[7] Zhao, H., Wang, J., Xing, J., Gao, Y. (2015). A feature extraction method based on LMD and MSE and its application for fault diagnosis of reciprocating compressor. *Journal of Vibroengineering*, vol. 17, no. 7, p. 3515-3526.

[8] Wang, Z., Yao, D., Duan, L. (2007). Study on the method of oil field reciprocating compressor valve fault diagnosis based on fuzzy clustering. *Mechanical Strength*, vol. 29, no. 3, p. 521-524. (in Chinese)

[9] Figlus, T., Gnap, J. Skrúcany,T. Šarkan, B., Stoklosa, J. (2016). The use of denoising and analysis of the acoustic signal entropy in diagnosing engine valve clearance. *Entropy*, vol. 18, no. 7, p. 1-11, **DOI:10.3390/e18070253**.

[10] Geng, Z., Chen, J. (2005). Investigation into piston-slap-induced vibration for engine condition simulation and monitoring. *Journal of Sound and Vibration*, vol. 282, no. 3-5, p. 735-775, **DOI:10.1016/j.jsv.2004.03.057**.

[11] Jedlinski, L., Caban, J., Krzywonos, L., Wierzbicki, S., Brumercik, F. (2015). Application of vibration signal in the diagnosis of IC engine valve clearance. *Journal of Vibroengineering*, vol. 17, no. 1, p. 175-187.

[12] Zhao, H., Wang, J., Han, H., Gao, Y. (2016). A feature extraction method based on HLMD and MFE for bearing clearance fault of reciprocating compressor. *Measurement*, vol. 89, p. 34-43, **DOI:10.1016/j.measurement.2016.03.076**.

[13] Zhao, H., Wang, J., Jay, L., Li, Y. (2018). A compound interpolation envelope local mean decomposition and its application for fault diagnosis of reciprocating compressors. *Mechanical Systems and Signal Processing*, vol. 110, p. 273-295, **DOI:10.1016/j.ymssp.2018.03.035**.

[14] Li, Y., Li, G., Yang, Y., Liang, X., Xu, M. (2018). A fault diagnosis scheme for planetary gearboxes using adaptive multi-scale morphology filter and modified hierarchical permutation entropy. *Mechanical Systems and Signal Processing*, vol. 105, p. 319-337, **DOI:10.1016/j.ymssp.2017.12.008**.

[15] Li, Z., Jiang, Y., Hu, C., Peng, Z. (2016). Recent progress on decoupling diagnosis of hybrid failures in gear transmission systems using vibration sensor signal: A review. *Measurement*, vol. 90, p. 4-19, **DOI:10.1016/j.measurement.2016.04.036**.

[16] Zhang, C., Peng, Z., Chen, S., Li, Z., Wang, J. (2018). A gearbox fault diagnosis method based on frequency-modulated empirical mode decomposition and support vector machine. *Proceedings of the Institution of Mechanical Engineers, Part C: Journal of Mechanical Engineering Science*, vol. 232, no. 2, p. 369-380, **DOI:10.1177/0954406216677102**.

[17] Bi, F., Li, L., Zhang, J., Ma, T. (2015). Source identification of gasoline engine noise based on continuous wavelet transform and EEMD-RobustICA. *Applied Acoustic*, vol. 100, p. 34-42, **DOI:10.1016/j.apacoust.2015.07.007**.

[18] Li, N., Yang, J., Zhou, R., Liang, C. (2016). Determination of knock characteristics in spark ignition engines: an approach based on ensemble empirical mode decomposition. *Measurement Science and Technology*, vol. 27, no. 4, p. 045109, **DOI:10.1088/0957-0233/27/4/045109**.

[19] Dragomiretskiy, K., Zosso, D. (2014). Variational mode decomposition. *IEEE Transaction on Signal Process*, vol. 62, no. 3, p. 531-544, **DOI:10.1109/TSP.2013.2288675**.

[20] Wang, Y., Markert. R, Xiang, J., Zheng, W. (2015). Research on variational mode decomposition and its application in detecting rub-impact fault of rotor system. *Mechanical Systems and Signal Processing*, vol. 60-61, p. 243-251, **DOI:10.1016/j.ymssp.2015.02.020**.

[21] Liu, Y., Wang, J., Li, Y., Zhao, H., Chen, S. (2017). Feature extraction method based on VMD and MFDFA for fault diagnosis of reciprocating compressor Valve. *Journal of Vibroengineering*, vol. 19, no. 8, p. 6007-6020, **DOI:10.21595/jve.2017.18726**.

[22] An, X., Yang, J. (2016). Denoising of hydropower unit vibration signal based on variational mode decomposition and approximate entropy. *Transaction of the Institute of Measurement abd Control*, vol. 38, no. 3, p. 282-292, **DOI:10.1177/0142331215592064**.

[23] Li, Y., Li, G., Wei, Y., Liu, B., Liang, X. (2018). Health condition identification of planetary gearboxes based on variational mode decomposition and generalized composite muliscale symbolic dynamic entropy. *ISA Transactions*, vol. 81, p. 329-341, **DOI:10.1016/j.isatra.2018.06.001**.

[24] Upadhyay, A., Pachori, R.B. (2015). Instantaneous voiced/non-voiced detection in speech signals based on variational mode decomposition. *Journal of the Franklin Institute*, vol. 352, no. 7, p. 2679-2707, **DOI:10.1016/j.jfranklin.2015.04.001**.

[25] Lahmiri, S. (2015). Long memory in international financial markets trends and short movements during 2008 financial crisis based on variational mode decomposition and detrended fluctuation analysis. *Physica A: Statistical Mechanics and it Applications*, vol. 437, p. 130-138, **DOI:10.1016/j.physa.2015.05.067**.

[26] Wilk-Kolodziejczyk, D., Regulski, K., Gumienny, G. (2016). Comparative analysis of the properties of the nodular cast iron with carbides and the austempered ductile iron with use of the machine learning and the support vector machine. *International Journal of Advanced Manufacturing Technology*, vol. 87, no. 1-4, p. 1077-1093, **DOI:10.1007/s00170-016-8510-y**.

[27] Wilk-Kolodziejczyk, D., Regulski, K., Gumienny, G., Kacprzyk, B., Kluska-Nawarecka, S., Jaskowiec, K. (2018). Data mining tools in identifying the components of the microstructure of compacted graphite iron based on the content of alloying elements. *International Journal of Advanced Manufacturing Technology*, vol. 95, no. 9-12, p. 3127-3139, **DOI:10.1007/s00170-017-1430-7**.

[28] Li, Y., Yang, Y., Wang, X., Liu, B., Liang, X. (2018). Early fault diagnosis of rolling bearings based on hierarchical symbol dynamic entropy and binary tree support vector machine. *Journal of Sound and Vibration*, vol. 428, p. 72-86, **DOI:10.1016/j.jsv.2018.04.036**.

Vsebina

Strojniški vestnik - Journal of Mechanical Engineering
letnik 65, (2019), številka 2
Ljubljana, februar 2019
ISSN 0039-2480

Izhaja mesečno

Razširjeni povzetki (extended abstracts)

Strojniški vestnik - Journal of Mechanical Engineering 65(2019)2, SI 11

Prejeto v recenzijo: 2018-10-13
Prejeto popravljeno: 2018-12-06
Odobreno za objavo: 2019-01-14

Kibernetsko-fizični sistem za nadzor hrapavosti obdelane površine pri oblikovnem frezanju

Uroš Župerl* – Franci Čuš
Univerza v Mariboru, Fakulteta za strojništvo, Slovenija

Namen raziskave je bil zasnovati, izdelati in testirati edinstven, kibernetsko-fizični obdelovani sistem za izvajanje spletnega nadzora hrapavosti obdelane površine pri oblikovnem frezanju. Inovativen nadzor hrapavosti površine se izvaja preko vizualnega nadzora velikosti odrezkov in predstavlja nov način spremljanja procesa obdelave, ki ga v obstoječi literaturi ni bilo moč zaslediti.

Cilj članka je predstaviti strukturo nadzornega sistema, ki je realiziran s povezovanjem računskih resursov v oblačni obdelovalni platformi z obdelovanim strojem in pripadajočim merilnim sistemom. Izdelan je pametni vizualni merilni sistem za zajemanje in prenos vrednosti velikosti odrezkov na obdelovalno platformo.

Obdelovalna platforma z integriranimi internetnimi aplikacijami neposredno spremlja hrapavost obdelane površine in izvaja nadzor oblike odrezka na osnovi naslednjih IoT uslug: napredna obdelava senzorskih signalov, identificiranja procesnih značilnosti, strojno učenje, analiza podatkov in kognitivne korekcije vodenja procesa. V članku je predstavljena internetna aplikacija z adaptivnim mehkim inferenčnim sistemom (ANFIS), ki je uporabljena za modeliranje in napovedovanje hrapavosti obdelane površine v realne času. Na osnovi napovedanih vrednosti hrapavosti, aplikacija za kognitivno korekcijo vodenja procesa z adaptiranjem obdelovalnih parametrov nadzoruje želeno velikost odrezka in posledično vzdržuje konstantno hrapavost obdelane površine.

Izveden je obdelovalni eksperiment z aksialno variabilno globino frezanja za testiranje učinkovitosti kibernetsko-fizičnega nadzornega sistema.

Eksperimentalni rezultati potrdijo, da je predlagani sistem, kjer so analitični resursi in storitve v oblaku povezani z obdelovalnim strojem in vizualnim sistemom učinkovit pri nadzoru hrapavosti obdelane površine. Sistem je stabilen, kar se kaže v izboljšani kakovosti površine. Nadzorovana hrapavost obdelane površine ne presega želene vrednosti za več kot 10 %. Aplikacija za kognitivne korekcije procesa uspe v 0,48 s vrniti velikost odrezka na referenčno vrednost. Korekcije vodenja se izvedejo v 10 ms po identifikaciji signifikantne spremembe velikosti odrezka.

Izvedena je validacija aplikacije za napovedovanje hrapavosti površine s primerjavo napovedi in eksperimentalnih podatkov. S primerjavo je ugotovljeno, da lahko aplikacija v realnem času napove hrapavost obdelane površine z napako manjšo od 3,7 % Večina napovedanih vrednosti hrapavosti je ekvivalentna s pripadajočimi eksperimentalnimi vrednostmi. Analiza negotovosti napovedi je pokazala, da se 98,2 % napovedanih vrednosti nahaja znotraj 95 % intervala zaupanja. Aplikacija pri majhni podajalni hitrosti in majhnih odrezkih v 1,8 % primerih podceni vrednost hrapavosti površine.

Cilj nadaljnjih raziskav je izvesti več obdelovalnih eksperimentov z različnimi rezalnimi parametri za testiranje predlaganega koncepta in odpravo omejitev raziskave. V nadaljevanju so povzete omejitve raziskave: kibernetska varnost in zasebnost, omejena hitrost prenosa podatkov na relaciji stroj-obdelovalna platforma, optimalna osvetlitev v vizualnem sistemu, neučinkovitost zaznavanja velikosti odrezka pri uporabi hladilno mazalnih sredstev in procesiranje ogromne količine podatkov. Možna rešitev zadnje omejitve je v pred obdelavi podatkov na lokalnem terminalu, ki se nato v kompaktni obliki prenesejo na oblačno platformo za nadaljnje analize.

Nadaljnje aktivnosti bodo usmerjene k nadgrajevanju obdelovalne platforme z novima aplikacijama za spremljanje rabe energije in spremljanje obrabe orodja.
Ključne besede: vodenje, nadzor, oblika odrezka, hrapavost površine, oblikovno frezanje, kibernetsko-fizični sistem

*Naslov avtorja za dopisovanje: Univerza v Mariboru, Fakulteta za strojništvo, Smetanova ulica 17, 2000 Maribor, Slovenija, uros.zuperl@um.si

Strojniški vestnik - Journal of Mechanical Engineering 65(2019)2, SI 12

Prejeto v recenzijo: 2018-06-28
Prejeto popravljeno: 2018-10-25
Odobreno za objavo: 2018-11-28

Analiza geometrijske površinske strukture in geometrijske točnosti zob cilindričnih zobnikov, izdelanih po postopku neposrednega laserskega sintranja kovin (DMLS)

Jadwiga Małgorzata Pisula – Grzegorz Budzik – Łukasz Przeszłowski
Tehniška fakulteta v Rzeszowu, Fakulteta za strojništvo in aeronavtiko, Poljska

Cilj predstavljene raziskave je ovrednotenje točnosti geometrije zob cilindričnih čelnih zobnikov, izdelanih po postopku neposrednega laserskega sintranja kovin (DMLS) z naknadno strojno obdelavo.

Zobniški prenosniki morajo izpolnjevati določene zahteve glede geometrijske in kinematične točnosti ter trajnosti za dane naloge. Za potrebe študije je bila izdelana serija cilindričnih čelnih zobnikov po postopku DMLS. Zobniki so bili nato dokončno obdelani z odrezavanjem.

Testni zobniki z izbrano geometrijo so bili narejeni iz nerjavnega jekla z visoko vsebnostjo kroma GP1 na stroju EOS M270. Zobniki so bili modelirani z različnimi dodatki za obdelavo glede na izbrani tehnološki proces in ob upoštevanju krčenja materiala. Meritve zobnikov v posameznih fazah izdelovalnega procesa so bile opravljene na koordinatnem merilnem stroju Klingelnberg P40. Poleg tega je bila opravljena tudi dvo- in trodimenzionalna karakterizacija površinske strukture z napravo za 3D-skeniranje Talyscan 150.

Analiza geometrijske točnosti cilindričnih čelnih zobnikov, narejenih z dodajalno izdelovalno tehnologijo DMLS, omogoča ustrezno pripravo procesa končne obdelave z odrezavanjem. Peskanje izboljša geometrijsko strukturo površine zobnika in rezultati se ujemajo s proizvajalčevimi podatki. Geometrijska struktura površine zobnika po rezkanju z univerzalnim orodjem je bila boljša od proizvajalčevih specifikacij. Točnost cilindričnega čelnega zobnika, izdelanega iz materiala GP1 po postopku DMLS, je bila zunaj razreda 12. Z uporabo univerzalnega orodja za obdelavo zobnikov je bil dosežen razred točnosti 8 po standardu DIN 3962-1, 2. Izdelava cilindričnih čelnih zobnikov po postopku DMLS in z naknadno strojno obdelavo je primerna za posamične izdelke ali za manjše serije.

Določiti bo treba še točnost zobnikov, izdelanih po postopku DMLS in naknadno obdelanih s posebnimi orodji za zobnike. Opraviti bo treba tudi meritve trdnosti zobnikov na preizkuševališču. Za popolno ovrednotenje obdelovalnosti materiala GP1 bi bilo treba zobnike preizkusiti po ustrezni toplotni obdelavi, ki ji sledi brušenje.

Prispevek, novosti, vrednost:

- Meritve geometrije testnih modelov čelnih zobnikov (surovcev in zob), izdelanih po postopku DMLS.
- Določitev razreda točnosti zobnikov po nataljevanju in po konturnem rezkanju zob z univerzalnim orodjem.
- Določitev geometrijske strukture površine z izbranimi dvo- in tridimenzionalnimi hrapavostnimi parametri po nataljevanju, peskanju zobnikov in rezkanju zob.

Ključne besede: postopek neposrednega laserskega sintranja kovin (DMLS), geometrijska struktura površine, cilindrični čelni zobniki, geometrijska točnost

*Naslov avtorja za dopisovanje: Tehniška fakulteta v Rzeszowu, Fakulteta za strojništvo in aeronavtiko, Poljska, jpisula@prz.edu.pl

Strojniški vestnik - Journal of Mechanical Engineering 65(2019)2, SI 13

Prejeto v recenzijo: 2018-07-25
Prejeto popravljeno: 2018-12-12
Odobreno za objavo: 2019-01-14

Večciljna optimizacija parametrov poravnavanja pri natančnem okroglem brušenju

Irina Stefanova Aleksandrova
Tehniška univerza v Gabrovem, Oddelek za strojništvo in tehnologije, Bolgarija

Optimalni pogoji za poravnavanje brusnih plošč, ki so navedeni v literaturi, vedno veljajo samo za konkretno vrsto orodij za brušenje in poravnavanje. V predhodni študiji so bili predstavljeni rezultati večciljne optimizacije poravnavanja brusnih plošč iz aluminijevega oksida med grobim okroglim brušenjem s koluti s sintetičnimi diamantnimi zrni različnih velikosti ter srednje in visoke trdnosti (kvaliteti AC32 in AC80). Brušenje se pogosto uporablja kot končna obdelava in zato obstaja potreba po opredelitvi parametrov sistema poravnavanja, ki bodo zagotavljali najmanjšo hrapavost in največjo točnost brušenih površin, kakor tudi najdaljšo obstojnost brusnih plošč in najnižje proizvodne stroške.

Cilj članka je določitev optimalnih parametrov sistema za poravnavanje brusnih plošč iz aluminijevega oksida med natančnim okroglim brušenjem z eksperimentalnimi koluti s sintetičnimi diamantnimi zrni različnih velikosti ter srednje in visoke trdnosti (kvaliteti AC32 in AC80).

Za proces brušenja je značilno veliko število spremenljivk (ekonomske, dinamične in proizvodne narave), ki so odvisne od pogojev med brušenjem ter od mikro- in makrogeometrije površine brusne plošče, ki se oblikuje med poravnavanjem. Vsaka od preučevanih odvisnih spremenljivk procesa natančnega brušenja je sicer pomembna, vendar ne zadostuje za optimalen nadzor procesa. Optimalne vrednosti raznih odvisnih spremenljivk je mogoče doseči z različnimi kombinacijami vrednosti nadzorovanih dejavnikov (pogoji pri poravnavanju, vrsta in lastnosti orodja za poravnavanje), vendar le pod pogojem, da so pogoji med obdelavo konstantni. Optimizacija procesa le po eni odvisni spremenljivki zato ni priporočljiva. Večciljna optimizacija zagotavlja večjo količino informacij za pravilno odločanje pri izbiri optimalnih parametrov sistema za poravnavanje.

Zato je bila uporabljena večciljna optimizacija na osnovi genetskega algoritma za pridobivanje optimalnih vrednosti spremenljivk procesa poravnavanja (radialno podajanje diamantnega koluta f_{rd}, razmerje hitrosti pri poravnavanju q_d, čas poravnavanja t_d, razmerje med velikostjo zrn diamantnega koluta in brusne plošče q_g, vrsta sintetičnega diamanta in smer poravnavanja). Za optimizacijski parameter je bila uporabljena posplošena kriterijska funkcija v obliki geometrijske sredine. Gre za kompleksen indikator, ki karakterizira hrapavost in natančnost obdelane površine, obstojnost brusne plošče in proizvodne stroške operacije brušenja.

Optimizacijski problem je bil razrešen v naslednjem zaporedju: 1) postavljeni so bili regresijski modeli spremenljivk procesa natančnega brušenja v odvisnosti od parametrov sistema za poravnavanje; 2) ustvarjen je bil model posplošene kriterijske funkcije, ki odraža kompleksen vpliv parametrov sistema za poravnavanje; 3) določeni so bili optimalni pogoji za istosmerno in protismerno poravnavanje brusnih plošč iz aluminijevega oksida z eksperimentalnimi koluti iz sintetičnega diamanta različnih velikosti zrn kakovosti AC32 in AC80, pri katerih je dosežen maksimum posplošene kriterijske funkcije; 4) določena je bila Pareto optimalna rešitev (f_{rd}=0,2 mm/min; q_d=0,8; t_d=4,65 s; q_g= 2,56), ki zagotavlja najboljšo kombinacijo hrapavosti ($Ra_w \leq 0.51$ μm), odstopanja obdelane površine od cilindričnosti ($\delta_w \leq 6{,}9$ μm) , obstojnosti brusne plošče ($T_s \geq 21{,}45$ min) in stroškov brusne operacije ($C_{21} \leq 0{,}04$ Eur/kos).

V članku je opisan nov pristop k večciljni optimizaciji procesa brušenja. Rezultati omogočajo nadzor in optimizacijo procesa natančnega brušenja z izbiro optimalnih parametrov sistema za poravnavanje, zato bodo koristni za vse proizvajalce strojev.

Ključne besede: natančno okroglo brušenje, parametri poravnavanja, diamantni koluti za poravnavanje, večciljna optimizacija, posplošena kriterijska funkcija, hrapavost in točnost brušene površine, obstojnost brusne plošče, stroški brusne operacije

*Naslov avtorja za dopisovanje: Tehniška univerza v Gabrovem, Oddelek za strojništvo in tehnologije, Bolgarija, irina@tugab.bg

Strojniški vestnik - Journal of Mechanical Engineering 65(2019)2, SI 14

Prejeto v recenzijo: 2018-10-29
Prejeto popravljeno: 2019-01-14
Odobreno za objavo: 2019-01-21

Numerična in eksperimentalna študija novega ventila za uravnavanje hitrosti hidravličnega aktuatorja s pomočjo energije povratnega toka

Grzegorz Filo[1,*] – Edward Lisowski[1] – Dominik Kwiatkowski[1] – Janusz Rajda[2]
[1] Politehnika v Krakovu, Krakov, Poljska
[2] PONAR Wadowice, Poljska

Članek obravnava možnosti povečanja hitrosti gibanja hidravličnega cilindra z enostranskim delovanjem s pomočjo toka tekočine iz povratnega voda. Tok fluida v povratnem vodu običajno ni v uporabi, saj se vrača neposredno v rezervoar. Preusmeritev povratnega toka iz rezervoarja za hidravlično tekočino v dovod pa povzroči znatno povečanje pritoka v aktuator. Do tega lahko pride le če batnica cilindra ni polno obremenjena v delu območja gibanja. V praksi pa je to razmeroma pogosto, npr. pri hidravličnih sistemih stiskalnic za odpadke, ekstrudorjev, rezalnih strojev itd. Uporaba povratnega toka tekočine omogoča večkratno povečanje hitrosti gibanja batnice, odvisno od geometrije hidravličnega cilindra (razmerja med premerom cilindra in batnice) in od območja gibanja, v katerem cilinder ni popolnoma obremenjen.

Pregled literature je pokazal, da tovrstni sistemi zahtevajo ustrezno regulacijo, ki je lahko elektronska ali hidravlična. Hidravlična regulacija je cenejša in preprostejša, saj ne zahteva merilnih pretvornikov ali mikroprocesorjev, je pa tudi manj natančna. Zato je predlagana rešitev v obliki novega regulacijskega ventila. Regulacijski ventil je sestavljen iz dušilnega ventila in diferencialnega ventila, ki se odziva na tlačno razliko med dovodom in povratnim vodom. Predlagana rešitev je bolj nastavljiva v primerjavi z običajno povezavo med dovodom in povratnim vodom. Poleg povečanja hitrosti zagotavlja tudi zmanjšanje hitrosti pod večjimi obremenitvami, razpored priključkov pa omogoča preprosto vgradnjo v obstoječe sisteme brez dodatne opreme.

Uporabljena metodologija vključuje 3D-modeliranje v paketu Creo Parametric, postavitev simulacijskega modela in izvedbo simulacij v paketu Matlab/Simulink, kakor tudi izvedbo laboratorijskih preizkusov na preizkuševališču. Simulacije so pokazale, da je mogoče z uporabo povratnega toka tekočine povečati hitrost gibanja batnice do trikrat. Rezultati numeričnih simulacij so bili preverjeni na preizkuševališču s prototipnim ventilom. Pridobljena je bila hitrostna karakteristika batnice kot funkcija obremenitve in nastavitve dušilnega ventila, ki se dobro ujema z rezultati simulacije. Potrjeno je bilo tudi, da je predlagana rešitev primerna in dovolj natančna za praktično uporabo. Izkazalo pa se je tudi to, da je nastavitveno območje bata ventila razmeroma kratko zaradi uporabe standardnega bata z ravnim čelom. Nadaljnje raziskave po metodi CFD bodo zato usmerjene v prilagoditev geometrije čela bata za bolj obvladljivo rešitev z različnimi odpiralnimi karakteristikami.

Ključne besede: modeliranje hidravličnih sistemov, raba energije povratnega toka, nova konstrukcija regulacijskega ventila, uravnavanje hitrosti hidravličnega aktuatorja

*Naslov avtorja za dopisovanje: Politehnika v Krakovu, Jana Pawla II 37, 31-864 Krakov, Poljska, filo@mech.pk.edu.pl

Strojniški vestnik - Journal of Mechanical Engineering 65(2019)2, SI 15

Prejeto v recenzijo: 2018-07-18
Prejeto popravljeno: 2018-12-17
Odobreno za objavo: 2019-01-14

Nov pristop k identifikaciji plinske kavitacije v curkovnih črpalkah za olje mazalnih sistemov

Jun Zhang[1] – Peiyong Ma[1] – Shuyi Gan[1] – Xianguo Hu[1,*] – Shunsen Wang[2]
[1] Tehniška univerza Hefei, Fakulteta za strojništvo, Kitajska
[2] Univerza Xi'an Jiaotong, Inštitut za turbostroje, Kitajska

Curkovne črpalke za olje so ključna komponenta mazalnih sistemov turbostrojev. S povečevanjem gostote moči pri turbostrojih se pojavlja problem kavitacije v omenjenih črpalkah, ki lahko ogroža varnost obratovanja. Med različnimi vrstami kavitacije v curkovnih črpalkah za olje ima posebno vlogo plinska kavitacija, ki znatno vpliva na učinkovitost delovanja črpalke. Težava pri identifikaciji plinske kavitacije je v tem, da je podobna parni kavitaciji, saj povzroča dvofazni tok plina in kapljevine v pretočnih kanalih. Identifikacija zato zahteva nekonvencionalne metode. Kljub temu, da se tako plinska kot parna kavitacija pojavljata v nizkotlačnem območju, gre za različna fizikalna pojava. Do plinske kavitacije prihaja zaradi difuzije in raztapljanja zraka v olju, fizikalni pojav v ozadju parne kavitacije pa je fazna premena parne in kapljevinske faze, ki poteka znatno hitreje kot proces masne difuzije. Razlikujejo se tudi njuni vplivi na delovanje curkovne črpalke za olje, ki jih je mogoče izkoristiti za identifikacijo plinske kavitacije.

Predmet pričujoče raziskave je kavitacijski tok mazalnega olja v curkovni črpalki. Zasnovano je bilo preizkuševališče za simulacijo obravnavane črpalke. Kavitacijski tok v oljni črpalki je bil simuliran s komercialnim programskim paketom za CFD Fluent. Analizirana je bila plinska kavitacija med obratovanjem črpalke v različnih delovnih pogojih. Uporabljenih je bilo več tehnologij za preskušanje tokov in več raziskovalnih metod na osnovi razlik med vplivi kavitacije na delovanje črpalke. Frekvenčni odziv je bil določen po metodi spektralne analize. Običajna Fourierjeva analiza ni primerna zaradi enostranskih signalov pri kavitacijskem toku in v fazi kolapsa mehurčka, v študiji je bila uporabljena analiza po metodi valčne transformacije. Učinkovitost oljne črpalke, ki se kaže v sesalni sposobnosti, izkoristku, kavitacijski eroziji, vibracijah, hrupu, volumskem deležu pare in porazdelitvi tlaka v različnih delovnih pogojih, je bila sistematično izmerjena in kvantificirana na osnovi rezultatov eksperimenta in numerične simulacije. Predstavljen je nov pristop k identifikaciji plinske kavitacije na osnovi frekvenčne karakteristike kavitacijskega procesa in njegovega mehanizma vplivanja na obratovanje curkovne črpalke za olje. Iz rezultatov je razvidno, da se plinska kavitacija pojavlja v razmeroma širokem razponu delovnih pogojev črpalke. Masni delež raztopljenega zraka v mazalnem olju je znašal 110 ppm in plinska kavitacija je nastopila v razponu tlačnega razmerja od 0,144 do 0,161. Ugotovljena je bila pri vrednosti kavitacijskega števila 1,68, izginila pa je pri vrednosti 1,31. Količina raztopljenega zraka v mazalnem olju je 6,3-krat večja kot v vodi, curkovna črpalka za olje pa je za 16 % bolj nagnjena h kavitaciji kot curkovna črpalka za vodo. Rezultat študije je nov pristop k identifikaciji plinske kavitacije, osvetljuje pa tudi mehanizme tega procesa in zagotavlja zanesljive eksperimentalne podatke o vplivu plinske kavitacije na mazalne sisteme turbostrojev. Študija daje tudi zanesljivo tehnično osnovo in mehanizme za identifikacijo, vrednotenje, napovedovanje vplivov in preprečevanje kavitacije v mazalnih sistemih.

Potrebne bodo še dodatne raziskave na področju razločevanja med plinsko in parno kavitacijo, denimo raziskave mehanizmov učinkovanja na mikrocurke in ustvarjanje udarnih valov, frekvenčne karakteristike hrupa, kavitacijske erozije itd. Za preprečevanje plinske kavitacije bodo potrebne tudi bolj dovršene visokohitrostne kamere in dinamične merilne naprave.

Ključne besede: curkovna črpalka za olje, mazalni sistem, različne vrste kavitacije, identifikacija plinske kavitacije, frekvenčna karakteristika, dvofazni tok plina in kapljevine

*Naslov avtorja za dopisovanje: Tehniška univerza Hefei, Fakulteta za strojništvo, Tunxi Road 193#, Hefei, Anhui, Kitajska, xghu@hfut.edu.cn

Strojniški vestnik - Journal of Mechanical Engineering 65(2019)2, SI 16

Prejeto v recenzijo: 2018-05-08
Prejeto popravljeno: 2018-11-15
Odobreno za objavo: 2019-01-09

Diagnosticiranje napak na ventilih batnih kompresorjev s pomočjo modificirane večskalne entropije in vrednotenja globalne razdalje

Ying Li – Jindong Wang* – Haiyang Zhao – Meiping Song – Lingfei Ou
Inštitut za strojništvo, Severovzhodna univerza za nafto, Kitajska

Za signale vibracij batnih kompresorjev je značilna nelinearnost, nestacionarnost in večkomponentna sklopitev. Metoda MSE omogoča opis kompleksnosti časovnih vrst in učinkovito razlikovanje med vrstami napak batnih kompresorjev. Pri izpeljavi različnih časovnih skal z grobim zrnjenjem se dolžina časovne vrste skrajšuje s povečanjem faktorja skaliranja, posledica tega pa je nenatančna ocena entropije ali nedefinirana entropija pri večjih faktorjih skaliranja ter pojav »letečega krila«. V članku je predstavljena metoda, s katero se je mogoče izogniti izgubi podatkov med postopkom grobega zrnjenja in znatno izboljšati natančnost algoritma.

Predlagana metoda za pridobivanje značilk napak je kombinacija metode VMD-MMSE in algoritma GDE.

Tradicionalna metoda grobega zrnjenja pri MSE vključuje zgoščevanje originalne časovne vrste s faktorjem skaliranja τ. Originalna časovna vrsta vsebuje le končno množino podatkov in s postopnim povečevanjem faktorja skaliranja τ se zmanjšuje dolžina grobo zrnjene časovne vrste. Izvirna dolžina podatkov ni večkratnik faktorja skaliranja τ, zato nastopita delna izguba podatkov in pojav »letečega krila«, ki vplivata na natančnost algoritmov v nadaljevanju. Zato je podan predlog metode grobega zrnjenja na osnovi drsečega povprečja (MMSE) za izvirno časovno vrsto, s katero se je mogoče izogniti izgubi podatkov. Nato je mogoče z metodo GDE optimizirati nabor značilk MMSE in izbrati občutljive značilke za izboljšanje natančnosti algoritma.

Predstavljena je nova metoda za diagnosticiranje napak na osnovi modificirane večskalne entropije in vrednotenja globalne razdalje za izpolnitev potrebe po prepoznavanju napak na ventilih batnih kompresorjev oz. za pridobivanje in optimalno izbiro značilk teh napak.

(1) V predlaganem postopku je uporabljena metoda VMD za odpravo šuma, ki daje pri signalih vibracij batnega kompresorja boljše rezultate kot tradicionalne metode časovne in frekvenčne analize, npr. EMD in paketna valčna transformacija.
(2) Po rekonstrukciji signala vibracij po metodi VMD je bila uporabljena nova metoda MMSE z drsečim povprečjem kot zamenjava za postopek grobega zrnjenja z aritmetično sredino, ki odpravlja težave konvencionalne večskalne entropije (MSE) z nedefinirano entropijo ali nenatančno oceno entropije pri večjih faktorjih skaliranja.
(3) Pri lastnih vrednostih MMSE se pojavlja prekrivanje. Za prečiščevanje končnega lastnega vektorja je bila uporabljena metoda GDE in s tem je bila dosežena večja učinkovitost in točnost odkrivanja napak.
(4) Metoda je bila uporabljena za diagnosticiranje napak na ventilih batnih kompresorjev v različnih stanjih. Rezultati v primerjavi z drugimi metodami pridobivanja značilk so odlični.

Za odstranitev šuma iz signala vibracij je bila uporabljena metoda VMD. Raziskave prednastavljene skale dekompozicije kažejo določen napredek in pojav mešanja oblik je do določene mere že odpravljen, toda izbira parametrov ni adaptivna. Potrebne so še dodatne raziskave za učinkovitejše odpravljanje šuma in mešanja oblik.

Metoda je uporabna za sprotni nadzor in zgodnje odkrivanje napak pri batnih kompresorjih, s tem pa je praktičnega pomena za varnost in zanesljivost obratovanja batnih kompresorjev.

Ključne besede: diagnosticiranje napak, ventil batnega kompresorja, modificirana večskalna entropija (MMSE), vrednotenje globalne razdalje (GDE), binarno drevo pri metodi podpornih vektorjev (BTVSM)

*Naslov avtorja za dopisovanje: Inštitut za strojništvo, Severovzhodna univerza za nafto, Daqing, Kitajska, wjd327@126.com

Information for Authors

All manuscripts must be in English. Pages should be numbered sequentially. The manuscript should be composed in accordance with the Article Template given above. The maximum length of contributions is 10 pages. Longer contributions will only be accepted if authors provide juastification in a cover letter. For full instructions see the Information for Authors section on the journal's website: http://en.sv-jme.eu .

SUBMISSION:

Submission to SV-JME is made with the implicit understanding that neither the manuscript nor the essence of its content has been published previously either in whole or in part and that it is not being considered for publication elsewhere. All the listed authors should have agreed on the content and the corresponding (submitting) author is responsible for having ensured that this agreement has been reached. The acceptance of an article is based entirely on its scientific merit, as judged by peer review. Scientific articles comprising simulations only will not be accepted for publication; simulations must be accompanied by experimental results carried out to confirm or deny the accuracy of the simulation. Every manuscript submitted to the SV-JME undergoes a peer-review process.

The authors are kindly invited to submit the paper through our web site: http://ojs.sv-jme.eu. The Author is able to track the submission through the editorial process - as well as participate in the copyediting and proofreading of submissions accepted for publication - by logging in, and using the username and password provided.

SUBMISSION CONTENT:

The typical submission material consists of:

- A **manuscript** (A PDF file, with title, all authors with affiliations, abstract, keywords, highlights, inserted figures and tables and references),
- Supplementary files:
  - a **manuscript** in a WORD file format
  - a **cover letter** (please see instructions for composing the cover letter)
  - a ZIP file containing **figures** in high resolution in one of the graphical formats (please see instructions for preparing the figure files)
  - possible **appendicies** (optional), cover materials, video materials, etc.

Incomplete or improperly prepared submissions will be rejected with explanatory comments provided. In this case we will kindly ask the authors to carefully read the Information for Authors and to resubmit their manuscripts taking into consideration our comments.

COVER LETTER INSTRUCTIONS:

Please add a **cover letter** stating the following information about the submitted paper:

1. Paper **title**, list of **authors** and their **affiliations**.
2. **Type of paper**: original scientific paper (1.01), review scientific paper (1.02) or short scientific paper (1.03).
3. A **declaration** that neither the manuscript nor the essence of its content has been published in whole or in part previously and that it is not being considered for publication elsewhere.
4. State the **value of the paper** or its practical, theoretical and scientific implications. What is new in the paper with respect to the state-of-the-art in the published papers? Do not repeat the content of your abstract for this purpose.
5. We kindly ask you to suggest at least two **reviewers** for your paper and give us their names, their full affiliation and contact information, and their scientific research interest. The suggested reviewers should have at least two relevant references (with an impact factor) to the scientific field concerned; they should not be from the same country as the authors and should have no close connection with the authors.

FORMAT OF THE MANUSCRIPT:

The manuscript should be composed in accordance with the Article Template. The manuscript should be written in the following format:

- A **Title** that adequately describes the content of the manuscript.
- A list of **Authors** and their **affiliations**.
- An **Abstract** that should not exceed 250 words. The Abstract should state the principal objectives and the scope of the investigation, as well as the methodology employed. It should summarize the results and state the principal conclusions.
- 4 to 6 significant **key words** should follow the abstract to aid indexing.
- 4 to 6 **highlights;** a short collection of bullet points that convey the core findings and provide readers with a quick textual overview of the article. These four to six bullet points should describe the essence of the research (e.g. results or conclusions) and highlight what is distinctive about it.
- An **Introduction** that should provide a review of recent literature and sufficient background information to allow the results of the article to be understood and evaluated.
- A **Methods** section detailing the theoretical or experimental methods used.
- An **Experimental section** that should provide details of the experimental set-up and the methods used to obtain the results.
- A **Results** section that should clearly and concisely present the data, using figures and tables where appropriate.
- A **Discussion** section that should describe the relationships and generalizations shown by the results and discuss the significance of the results, making comparisons with previously published work. (It may be appropriate to combine the Results and Discussion sections into a single section to improve clarity.)
- A **Conclusions** section that should present one or more conclusions drawn from the results and subsequent discussion and should not duplicate the Abstract.
- **Acknowledgement** (optional) of collaboration or preparation assistance may be included. Please note the source of funding for the research.
- **Nomenclature** (optional). Papers with many symbols should have a nomenclature that defines all symbols with units, inserted above the references. If one is used, it must contain all the symbols used in the manuscript and the definitions should not be repeated in the text. In all cases, identify the symbols used if they are not widely recognized in the profession. Define acronyms in the text, not in the nomenclature.
- **References** must be cited consecutively in the text using square brackets [1] and collected together in a reference list at the end of the manuscript.
- **Appendix(-icies)** if any.

SPECIAL NOTES

Units: The SI system of units for nomenclature, symbols and abbreviations should be followed closely. Symbols for physical quantities in the text should be written in italics (e.g. v, T, n, etc.). Symbols for units that consist of letters should be in plain text (e.g. $\mathrm{ms^{-1}}$, K, min, mm, etc.). Please also see: http://physics.nist.gov/cuu/pdf/sp811.pdf .

Abbreviations should be spelt out in full on first appearance followed by the abbreviation in parentheses, e.g. variable time geometry (VTG). The meaning of symbols and units belonging to symbols should be explained in each case or cited in a **nomenclature** section at the end of the manuscript before the References.

Figures (figures, graphs, illustrations digital images, photographs) must be cited in consecutive numerical order in the text and referred to in both the text and the captions as Fig. 1, Fig. 2, etc. Figures should be prepared without borders and on white grounding and should be sent separately in their original formats. If a figure is composed of several parts, please mark each part with a), b), c), etc. and provide an explanation for each part in Figure caption. The caption should be self-explanatory. Letters and numbers should be readable (Arial or Times New Roman, min 6 pt with equal sizes and fonts in all figures). Graphics (submitted as supplementary files) may be exported in resolution good enough for printing (min. 300 dpi) in any common format, e.g. TIFF, BMP or JPG, PDF and should be named Fig1.jpg, Fig2.tif, etc. However, graphs and line drawings should be prepared as vector images, e.g. CDR, AI. Multi-curve graphs should have individual curves marked with a symbol or otherwise provide distinguishing differences using, for example, different thicknesses or dashing.

Tables should carry separate titles and must be numbered in consecutive numerical order in the text and referred to in both the text and the captions as Table 1, Table 2, etc. In addition to the physical quantities, such as t (in italics), the units [s] (normal text) should be added in square brackets. Tables should not duplicate data found elsewhere in the manuscript. Tables should be prepared using a table editor and not inserted as a graphic.

REFERENCES:

A reference list must be included using the following information as a guide. Only cited text references are to be included. Each reference is to be referred to in the text by a number enclosed in a square bracket (i.e. [3] or [2] to [4] for more references; do not combine more than 3 references, explain each). No reference to the author is necessary.

References must be numbered and ordered according to where they are first mentioned in the paper, not alphabetically. All references must be complete and accurate. Please add DOI code when available. Examples follow.

Journal Papers:

Surname 1, Initials, Surname 2, Initials (year). Title. Journal, volume, number, pages, DOI code.

[1] Hackenschmidt, R., Alber-Laukant, B., Rieg, F. (2010). Simulating nonlinear materials under centrifugal forces by using intelligent cross-linked simulations. *Strojniški vestnik - Journal of Mechanical Engineering,* vol. 57, no. 7-8, p. 531-538, DOI:10.5545/sv-jme.2011.013.

Journal titles should not be abbreviated. Note that journal title is set in italics.

Books:

Surname 1, Initials, Surname 2, Initials (year). Title. Publisher, place of publication.

[2] Groover, M.P. (2007). *Fundamentals of Modern Manufacturing*. John Wiley & Sons, Hoboken.

Note that the title of the book is italicized.

Chapters in Books:

Surname 1, Initials, Surname 2, Initials (year). Chapter title. Editor(s) of book, book title. Publisher, place of publication, pages.

[3] Carbone, G., Ceccarelli, M. (2005). Legged robotic systems. Kordić, V., Lazinica, A., Merdan, M. (Eds.), Cutting Edge Robotics. Pro literatur Verlag, Mammendorf, p. 553-576.

Proceedings Papers:

Surname 1, Initials, Surname 2, Initials (year). Paper title. Proceedings title, pages.

[4] Štefanić, N., Martinčević-Mikić, S., Tošanović, N. (2009). Applied lean system in process industry. *MOTSP Conference Proceedings*, p. 422-427.

Standards:

Standard-Code (year). Title. Organisation. Place.

[5] ISO/DIS 16000-6.2:2002. *Indoor Air – Part 6: Determination of Volatile Organic Compounds in Indoor and Chamber Air by Active Sampling on TENAX TA Sorbent, Thermal Desorption and Gas Chromatography using MSD/FID.* International Organization for Standardization. Geneva.

WWW pages:

Surname, Initials or Company name. Title, from http://address, date of access.

[6] Rockwell Automation. Arena, from *http://www.arenasimulation.com,* accessed on 2009-09-07.

EXTENDED ABSTRACT:

When the paper is accepted for publishing, the authors will be requested to send an **extended abstract** (approx. one A4 page or 3500 to 4000 characters). The instruction for composing the extended abstract are published on-line: http://www.sv-jme.eu/information-for-authors/ .

COPYRIGHT:

Authors submitting a manuscript do so on the understanding that the work has not been published before, is not being considered for publication elsewhere and has been read and approved by all authors. The submission of the manuscript by the authors means that the authors automatically agree to transfer copyright to SV-JME when the manuscript is accepted for publication. All accepted manuscripts must be accompanied by a Copyright Transfer Agreement, which should be sent to the editor. The work should be original work by the authors and not be published elsewhere in any language without the written consent of the publisher. The proof will be sent to the author showing the final layout of the article. Proof correction must be minimal and executed quickly. Thus it is essential that manuscripts are accurate when submitted. Authors can track the status of their accepted articles on http://en.sv-jme.eu/.

PUBLICATION FEE:

Authors will be asked to pay a publication fee for each article prior to the article appearing in the journal. However, this fee only needs to be paid after the article has been accepted for publishing. The fee is 380 EUR (for articles with maximum of 6 pages), 470 EUR (for articles with maximum of 10 pages), plus 50 EUR for each additional page. The additional cost for a color page is 90.00 EUR. These fees do not include tax.

Strojniški vestnik -Journal of Mechanical Engineering
Aškerčeva 6, 1000 Ljubljana, Slovenia,
e-mail: info@sv-jme.eu

9 770039 248001
ISSN 0039-2480

http://www.sv-jme.eu

Contents

Papers